STUDY OF NEW FUNCTIONALIZED NANOMATERIALS FOR NON-INVASIVE POINT-OF-CARE BIOSENSOR DEVICES

A Dissertation
Submitted to the Graduate Faculty
of the
North Dakota State University
of Agriculture and Applied Science

By

Michael Edward Johnson

In Partial Fulfillment of the Requirements
for the Degree of
DOCTOR OF PHILOSOPHY

Major Program:
Materials and Nanotechnology

August 2021

Fargo, North Dakota

North Dakota State University
Graduate School

Title

STUDY OF NEW FUNTIONALIZED NANOMATERIALS FOR NON-INVASIVE POINT-OF-CARE BIOSENSOR DEVICES

By

Michael Edward Johnson

The Supervisory Committee certifies that this ***disquisition*** complies with North Dakota State University's regulations and meets the accepted standards for the degree of

DOCTOR OF PHILOSOPHY

SUPERVISORY COMMITTEE:

Dr. Danling Wang
Chair

Dr. Qifeng Zhang

Dr. Erik Hobbie

Dr. Gregory Cook

Approved:

08/16/2021
Date

Dr. Erik Hobbie
Department Chair

ABSTRACT

Early disease detection and in-time health monitoring via novel sensing systems is highly demanded for modern medicine and health management. Recent development in nanotechnology and nanomaterials such as functionalized nanostructured metal-oxide semiconductors and newly discovered two-dimensional Ti_3C_2 MXenes have offered exciting areas of research as nanomaterial-based biomedical sensing devices. In this thesis, two major nanomaterials, KWO for application in diabetes and MXene for cancer management and further improvement of the KWO diabetes sensor, are intensively researched. KWO shows great potential as a breath acetone sensor, which can be utilized to monitor and diagnose diabetes. It also shows the unique ferroelectric property, which allows for a room-temperature sensing operation. Synthesis methods and characterization are done to further the understanding of KWO as an acetone sensor and further improve its capability towards becoming the cornerstone of a handheld biomedical sensor that is non-invasive, portable, and easy-to-use. Continuing, Ti_3C_2 MXenes are studied and characterized under various synthesis conditions to create both accordion-like structures with varying gap widths, and single-to-few layered nanosheets created by the intercalation of Li^+ ions. Additionally, a new sensor based on 2D nanosheets, Ti_3C_2 MXene, has been designed and used for the sensing response to 8-HOA and PGE_2 in lung cancer cells. The preliminary results indicate an important conclusion: this new Ti_3C_2-based sensor can provide a convenient and simple method for anti-cancer treatment guidance. Finally, a nanocomposite is synthesized using both KWO and Ti_3C_2 MXenes to improve the acetone sensor's sensitivity and selectivity by majorly reducing humidity cross-interference.

ACKNOWLEDGMENTS

First and foremost, I would like to acknowledge my advisors Dr. Danling Wang and Dr. Qifeng Zhang, for giving me the opportunity to join their groups. Since 2017, Dr. Wang has supported me not only by providing financial assistantship but also motivating my great interest in exploring new functional nanomaterials for applications in medical devices. Dr. Zhang has helped me conduct nanomaterial synthesis and his guidance aided me in eventually overcoming the challenges I had met. My dissertation could not be done without their excellent guidance, invaluable and constant support, and great encouragement.

I am also very thankful my committee members, Dr. Erik Hobbie, and Dr. Gregory Cook, for providing me with great advice and suggestions to improve my dissertation and defense.

The members of NEWS lab have provided me with many useful discussions and valuable suggestions to my research. Here, I would like to thank the past and present members: Razuan Hossain, Anna M. Schornack, Anna Rudie, Mahek Saqid, and Sampada Koirala. It was so nice to work with all of you. I would also like to acknowledge both the Core Research Facilities and Electron Microscopy Center at North Dakota State University for access to equipment and facilities that allowed this research work.

Finally, I want to thank my parents, my brother, and the rest of my family who supported me through this process. Without their support, I would not be here.

DEDICATION

Dedicated & in Memory to Dr. James Clement Mickus

TABLE OF CONTENTS

LIST OF TABLES

LIST OF FIGURES

LIST OF ABBREVIATIONS

MWO	A tungsten oxide semiconducting material made with an additional metal, M, such as KWO for potassium.
XRD	X-ray Diffraction
XPS	X-Ray Photoelectron Spectroscopy
FT-IR	Fourier Transform Infrared spectroscopy
SEM	Scanning Electron Microscopy
TEM	Transmission Electron Microscopy

LIST OF APPENDIX TABLES

LIST OF APPENDIX FIGURES

1. FUNCTIONALIZED NANOMATERIAL DEVELOPMENT FOR USE AS MEDICAL DEVICES FOR CHRONIC DISEASES

1.1. Introduction

Nanomaterials, a hot area of research currently, have unique properties due to having at least one dimension less than 100 nm. They can be divided into categories of one-dimensional (1D), 2-dimensional (2D), and three-dimensional materials. Examples of 1D nanomaterials include nanowires, nanorods, and nanotubes. 2D nanomaterials are typically referred to as nanosheets, as they present a flat plane-like morphology. Examples include graphene, MXenes, black phosphorus nanosheets, transition metal dichalcogenides (TMDs), and hexagonal boron nitride (h-BN). 3D nanomaterials can vary wildly in morphology but can typically be referred to as a nanoparticle or nanocluster. The methods of synthesis can include either bottom-up or top-down strategies of fabrication. Advancement in fabrication technology has enabled the manipulation of the structure and morphology of nanomaterials, which has led to extensive opportunity and possibility of research for functional devices and applications based around nanomaterials.

Many unique properties of nanomaterials make them promising candidates for new sensing technology. The various morphologies of nanomaterials have already been discussed. However, the high surface-area nature nanomaterials present is certainly worth noting as it provides many active sites for improving sensitivity. The implementation of specialized nanomaterials also makes analysis very fast, giving in-time readings which can be used to take immediate action if needed. Many fields have benefited from the invention of novel chemical sensors based on functionalized nanomaterials, with the healthcare field being the most prominent.

As a rapid, non-invasive, and efficient early disease diagnosis and management, nanomaterial-based gas sensors have become very promising candidates for application in the medical field. Traditional approaches towards disease diagnosis such as blood or urine analysis are invasive and typically require one-time-use sensing strips. Breath, however, is always readily accessible and requires no poking nor privacy to collect. The targets of breath analysis are volatile organic compounds (VOCs) in collected breath samples, which are organic compounds created via different metabolic pathways and expelled through the breath. [1] There are different techniques that have been developed to date to detect VOCs accurately such as proton transfer reaction-mass spectrometry (PTR-MS), selected ion flow tube (SIFT-MS), laser spectroscopy, and gas chromatography (GC). [2-4] While these techniques are extremely accurate while detecting these VOCs, they are expensive, large, require highly trained individuals to operate, and have testing can take a long time. Breath sensors based around nanomaterials, on the other hand, show the potential to overcome these flaws being portable, easy to use, and give fast measurements.

Herein, an overview of current breath analyses, including biomarkers which are detectable in human breath are explored along with requirements for the use of breath sensors for disease diagnosis. Continuing with these requirements, recent developments in new nanomaterial-based breath gas sensors are reviewed including sensing mechanisms and target biomarkers, as overviewed in **Figure 1.**

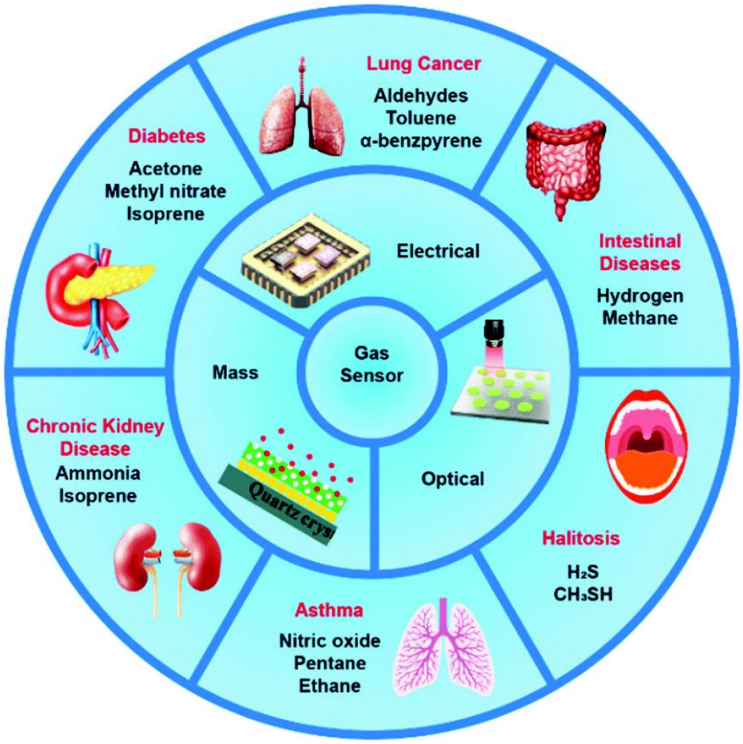

Figure 1. An overview of nanomaterial-based breath sensors' working mechanisms and some potential diseases, with biomarkers, they can be designed for. [5]

1.2. VOC Breath Biomarkers Detections and Challenges

While some human biofluids (blood, breath, sweat, saliva, urine, and feces) contain VOCs, the breath is the largest potential source. [6] And while all these biofluids are considered feasible candidates for VOC detection, the breath is one of the least invasive and most convenient to sample. The basics of breath analysis diagnose disease by detecting a change in concentration of one or more VOCs on the breath. When analyzed in this fashion, these VOCs can be referred to as biomarkers. Detecting biomarkers on the breath is a non-invasive, direct, and low-cost technique, which contributes to the development of predictive, preventative, personalized, and participatory medicine.

There are nearly 900 identified VOCs in the human breath that can work as biomarkers. [6] As these VOCs arise from metabolic processes, they can be used to gather pertinent information on metabolic disorders or dysfunction in the human body. Endogenous VOCs arise

from internal metabolic processes and are useful in clinical application as they carry important information on metabolic changes. Common VOCs on the breath include ketones, acids, aldehydes, and alcohols which are produced by different biochemical and physiological processes. So, it can be surmised that abnormal VOC concentrations are indicative to an abnormal metabolic state and can be used to distinguish certain diseases. Continuing, some common VOCs which can be used as biomarkers for various diseases will be discussed.

Acetone can be found in a higher concentration on the breath of those who have diabetes. Diabetes patients have an insufficient level of insulin, and stored sugar is quickly depleted. As the body cannot get enough glucose from the blood, gluconeogenesis is accelerated in the liver along with the oxidation of fatty acids. The oxidation of fatty acids creates a large amount of acetyl-CoA. Normally the excess acetyl-CoA would enter the citric acid cycle to be broken down, however, the accelerated gluconeogenesis depletes oxaloacetic acid, which is vital for acetyl-CoA to enter the citric acid cycle. Since acetyl-CoA cannot enter the normal citric acid cycle it is used to synthesize ketone bodies including acetone. [7] Excess acetone ends up in the bloodstream and is often released through the breath. As a biomarker for diabetes, acetone on exhaled breath is usually in the range of below 0.8 ppm (parts per million), for healthy individuals, to excesses of 1.76 ppm, for those living with diabetes. [8]

Ammonia is created during the digestion of proteins and is produced and released in the kidneys for maintaining a stable pH in the body. Typically, the liver converts ammonia in the bloodstream into urea, which is then expelled in the urine. Ammonia in mouth-exhaled breath is typically about 885 ppb (parts per billion) and has a nose-exhaled concentration of about 110 ppb. [9] Breath-ammonia can be used to diagnose kidney malfunction; it has been found that the concentration of ammonia is higher in patients (556 ppb) suffering from chronic kidney disease

(CKD) than in healthy patients (284 ppb). [10] Breath analysis techniques measuring ammonia have been shown to have great clinical value in rapid neonatal screening. Hemodialysis patients also benefit from daily tracking of breath ammonia. Measuring breath ammonia concentration and blood urea concentration in conjunction have been shown to be a vital monitoring technique for patients with end-stage CKD during dialysis. [11]

Fractional exhaled nitric oxide (FeNO) is produced by airway cells and is correlated to the number of inflamed cells. So, FeNO can be used as a biomarker of any condition that causes airway inflammation. FeNO detection has been shown to be a reliable, simple, and sensitive method for diagnosing and monitoring multiple respiratory diseases in clinical practice such as bronchial asthma, chronic coughs, and chronic obstructive pulmonary disease. [12] NO is also a biological regulatory factor produced in the body that plays an important role in many physiological and pathological processes. Levels of FeNO exhaled by children with asthma are elevated compared to healthy controls. Furthermore, FeNO levels may reflect the amount of airway inflammation, which is a pathological feature of asthma. [5]

Isoprene is created from the biosynthesis of cholesterol, and thus may be used to measure blood cholesterol level or evaluate cholesterol synthesis rate. Breath isoprene is closely related to physical activity: its concentration rapidly increases right after the start of exercise and then stabilizes at a lower level. Therefore, physical activity should be assessed with care if the breath isoprene concentration is used as an index of endogenous isoprene. Additionally, breath isoprene is a potential indicator of several diseases including diabetes, end-stage renal failure, lung cancer, and chronic liver disease with advanced fibrosis. [13-16]

Hydrogen and methane are formed entirely from carbohydrates breaking down via colonic anaerobic bacterial fermentation in the large intestine. Thus, are associated with

intestinal diseases such as small intestinal bacterial overgrowth (SIBO) and constipation-predominant irritable bowel syndrome (IBS). [17-18] hydrogen and methane breath analysis, as an alternative tool for diagnosis of SIBO, overcomes difficulties that bacterial culture of small intestine fluid as an invasive, complex, and not suitable for the outpatient clinical setting procedure. This is because SIBO can be diagnosed if the breath-concentration of hydrogen is above 12 ppm within 2 hours after oral ingestion of glucose or lactulose. [19] It is also reported that breath methane correlates to constipation-predominant IBS. [20]

Volatile sulfides, such as hydrogen sulfide gas, in the oral cavity cause endogenous halitosis. Volatile sulfides can be produced by Helicobacter pylori, which may be related to halitosis. H_2S is a well-known biomarker in breath for halitosis. Selective detection of H_2S gas more than 2 ppm in exhaled breath is required to screen patients suffering from halitosis. [21]

Aldehydes on the breath have been correlated to lung cancers. [22] Oxygen free radicals are commonly found in lung cancer patients. The excessive amount of oxygen free radicals in the body leads to potential oxidative stress injury, which is the main cause of lung cell damage. In this case, lipid peroxidation of various unsaturated fatty acids in the cell membranes has aldehyde products. Lipid peroxidation is a chain reaction; first, reactive oxygen species remove the hydrogen atoms of the propene group, producing conjugated groups, which are then oxidized by oxygen to produce aldehydes.

These are but a few selected VOCs that have been utilized as biomarkers to diagnose and monitor diseases. Much more research can be done to understand the creation of endogenous VOCs so that we may continue to exploit using engineered devices which are more affordable, less invasive, personalized methods for diagnosing and monitoring disease.

Detecting VOCs can be quite challenging, however. As mentioned, many VOCs in breath have concentrations in the ppm to ppb range. On top of that, the change in VOC concentration caused by body metabolism that can be detected is typically quite small. This means materials developed as sensor devices need to have ultrahigh sensitivity and high resolution to differentiate such small change in concentration. Beyond this, human breath is very complex with mixtures of more than 1000 organic compounds like VOCs, inorganic compounds, and high concentration of humidity. Thus, the sensor materials for VOC detection need to have extremely high selectivity for disease-related VOC compounds to allow for accurate detection and measurement with no false signals from the many other agents that can also exist in the sample. These two factors open an interesting new direction of research: the synthesis of new functionalized nanomaterials tailored to be sensing materials for realizing the purpose of disease-related VOC detection. The development of nanomaterials to achieve this high level of functionality requires an in-depth knowledge of currently known sensing mechanisms, which will be discussed next.

1.3. Nanomaterial-Based Medical Sensor Devices

Nanomaterials have spurred research into the development of numerous medical sensor devices with the interaction between the target VOC and nanomaterial being the key area of detection. Sensors can use one of three main sensing mechanisms: electrical, optical, and mass-sensitive. Herein, each type of mechanism will be overviewed with examples of current research.

1.3.1. Optical

Optical sensors work by utilizing a mechanism in which the interaction of electromagnetic waves with a target analyte alters the optical properties of the nanomaterial. This can be in the form of fluorescence, localized surface plasmon resonance (LSPR), or surface-enhanced Raman spectroscopy (SERS). Fluorescence mechanisms have a change in light

intensity when a specific analyte interacts with a specific nanomaterial. LSPR-based sensors use nanomaterials of noble-metals as they present the best LSPR properties. It has been shown that LSPR-based sensors can detect gaseous toluene, octane, xylene, and chlorobenzene using an Ag nanoparticle with an Au nanoshell, which was fully reversible. [23] **Figure 2** shows the working mechanism behind these devices, which is a visible change occurring due to surface condensation. SERS-based sensors are like LSPR-based sensors but will also include a chemical enhancement which allows for extremely high sensitivity and selectivity.

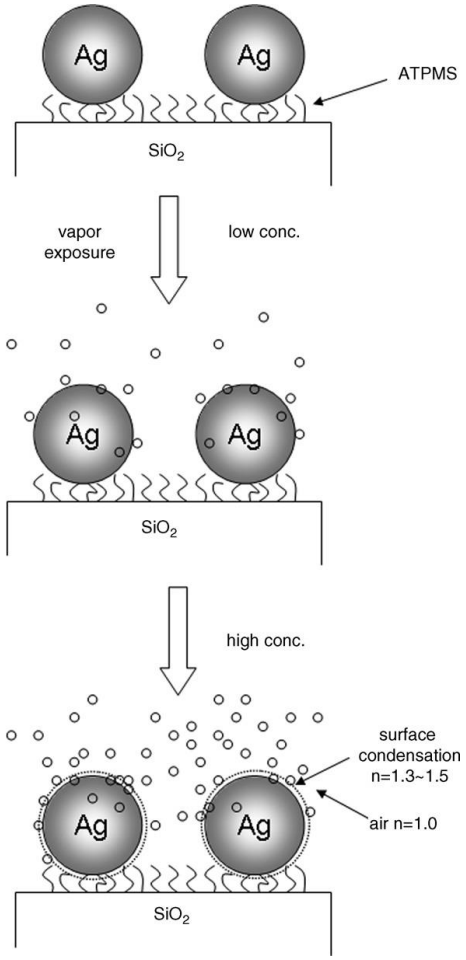

Figure 2. Illustrations for LSPR–VOC sensor response mechanism. [23]

1.3.2. Mass-Sensitive

Mass-sensitive nanomaterial-based sensors utilize the same mechanism a quartz crystal microbalance (QCM) utilizes. By capturing a target analyte, a change in any of the oscillatory parameters, frequency, amplitude, and wave velocity, of the piezoelectric crystal can be measured. For example, a QCM sensor coated with a thick Au layer and cobalt (II) phthalocyanine–silica nanocomposite to detect NO has been developed as a tool to diagnose asthma. The sensing mechanism involves coordinated adsorption of NO onto the cobalt (II) phthalocyanine, which leads to a shift in the resonance frequency of the modified QCM sensor, **Figure 3**. [24] It can be seen that the frequency of the QCM decreases with the capture of analyte gases of acetone and NO.

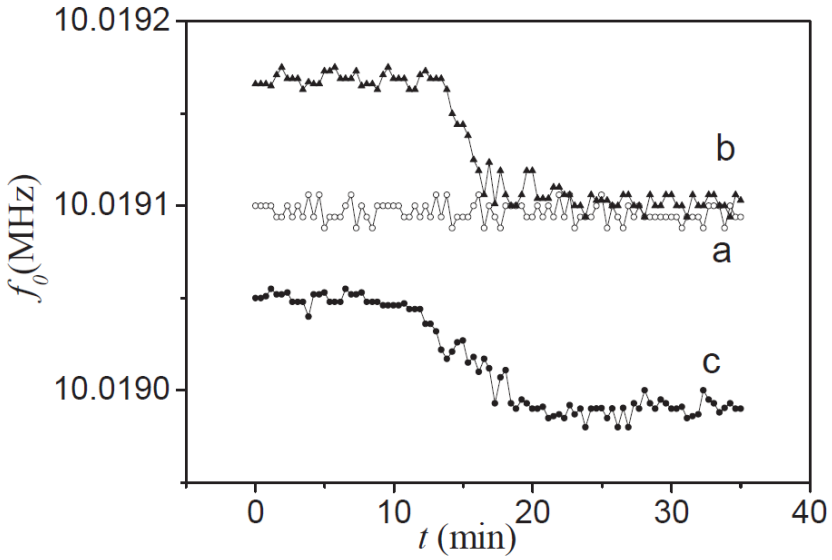

Figure 3. Typical response curves of 17.3 ppm acetone 5.75 ppb NO mixture gas on (a) bare (b) TiO_2-MWCNT (c) cobalt phthalocyanine silica modified QCM sensor on MQCM device. [24]

1.3.3. Electrical

The most basic electrical parameters are resistance, voltage, and current. Thus, the most basic working mechanism for nanomaterial-based medical sensors will operate by having anyone of the three of these parameters change when exposed to the targeted VOC, with greater

concentrations causing greater electrical change. As all these properties are correlated due to Ohm's law, the typical measurement taken is change of resistance.

Electrical sensors are the most widely used and well established for use as medical device sensors. Common chemical sensing nanomaterials include metal oxide semiconductors (MOS), carbon-based nanomaterials like graphene and carbon nanotubes (CNTs), and conductive metal organic frameworks (MOF). [25-26] The sensing principles of nanomaterial MOS-based sensors including WO_3, ZnO, SnO_2, and Cu_2O is the most widely investigated. This is due to the variety of synthesis techniques that can be used to make these materials. This variety allows for numerous morphologies which can cause changes in the crystal structure, exposed crystal faces, and functional groups which dot the surface of the material. These properties can all have a direct impact on the sensing performance of final sensor devices.

Another new material which has become of particular interest is the 2D nanosheet, Ti_3C_2 MXenes. These new materials have been proven to be effective gas- and electrochemical sensors due to their unique morphology, electrical properties, and surface functional groups. [27]

For the application of medical devices, VOC biomarkers will interact with the surface of the nanomaterial and cause a change in resistance due to a charge transfer mechanism. This is referred to as the chemiresistive property, and an electrical sensor which works using this mechanism is called a chemiresistive sensor. Due to their simple working principle and ease of fabrication and miniaturization, they are very popular in current research for the development of nanomaterial-based medical sensors. [5, 23-27] Although these advantages of chemiresistive based gas sensors, it has some disadvantages. First is the sensitivity and selectivity, which require a high degree of tuning material properties such as specific crystal facets, tuning crystal phases, and control over any surface functionalization. Second is the high operating temperature,

current materials utilize a redox reaction that requires temperatures of 160 ^{o}C and even higher. This is especially poor for device design as it adds another layer of complexity and power draw. Third is achieving high stability, the material needs to be able to stand up to multiple uses and maintain its sensing feature. Lastly, the humidity cross-interference is near ubiquitous to all electrical based sensors. This is the effect that causes signal to deteriorate in the presence of high moisture environments. Considering these factors, this work mainly focuses on chemiresistive gas sensor devices and the synthesis of novel nanostructured materials to optimize the device sensing performance.

In this thesis, considering the actual applications for specific disease early detection and management, exploring new nanomaterials as the sensing materials in the sensors is the main goal for my PhD study. Herein, we emphasize two novel nanomaterials, one is 1-dimensional nanostructured semiconducting material: $K_2W_7O_{22}$ nanorod; the other is 2-dimentional Ti_3C_2 MXene nanosheet materials is done to further scientific understanding pertaining to utilization as biomedical sensor devices. Specifically, novel $K_2W_7O_{22}$ nanorods show great potential as an acetone sensor to diagnose and monitor diabetes. Ti_3C_2 MXenes are studied for their basic properties utilizing new synthesis techniques and are studied for their feasibility as a biomedical sensor for monitoring the progress of new novel cancer treatments. Both nanomaterials were also combined as a composite to further improve the properties of the acetone sensor.

2. METAL TUNGSTEN OXIDES AS CHEMIRESISTIVE BREATH-ACETONE SENSORS[1]

2.1. Introduction

2.1.1. Diabetes

Diabetes is one of the leading causes of health complications and death currently in the United States. Diagnosing and monitoring methods are invasive, risk infection, and can become costly due to regularly replacing either lancets, needles, or sensing strips. The design of a breathalyzer device for diabetes monitoring and diagnosis would eliminate these negative side-effects while already living with a debilitating disease. It could also improve point-of-care by yielding fast results while collecting patient data for a personalized history to better manage and track daily life living with diabetes.

Human exhaled breath contains mostly nitrogen (78.04%), oxygen (16%), carbon dioxide (4-5%) [28], other inert gases (0.9%) [29] and water vapor (5%). Beyond that, there are thousands of Volatile-Organic-Compounds (VOCs) on the breath that range in concentration from parts-per-million (ppm), parts-per-billion (ppb), to as low as parts-per-trillion (ppt). [30] examples of such VOCs include; ethane (0-10 ppb), methane (2-10 ppm), pentane (0-10 ppb), nitric oxide (10-50 ppb), and nitrous oxide (1-20 ppb) [31], ammonia (0.5-2 ppm) [32], carbon monoxide (0-6 ppm) [29], hydrogen sulfide (0-1.3 ppm) [33], acetone (0.3-2 ppm) [34], ethanol, and isoprene (105 ppb) [15]. VOCs are not typically made by endogenous effects, but rather are influenced by exogenous factors such as food consumption, drug metabolization, or exposure to pollution. [35] To be able to detect a disease via the breath a VOC needs to be identified which

[1] The material in this chapter was co-authored by Michael Johnson and Danling Wang. Michael had primary responsibility for material synthesis, and data collection and analysis of XRD, XPS, TEM, SEM, Raman, and FT-IR. Michael was the primary developer of the conclusions that are advanced here. Michael also drafted and revised all versions of this chapter. Danling served as proofreader and checked the data and conclusions conducted by Michael.

functions as a biomarker for type-1 diabetes. It has already been found that acetone on the breath can be used as a biomarker for diabetes and sensing this acetone on the breath is a rapid and non-invasive method for screening and diagnosing diabetes and would be an effective method towards management of the disease as well. [1, 36]

The concentration of acetone in a healthy individual's breath is typically around 0.76 parts per million (ppm), while those with diabetes can have a breath-acetone concentration of 1.71 ppm or even higher, and so techniques need to be developed with enough sensitivity to work within this range. [34, 36] Using patient breath samples for non-invasive VOC detection has already been achieved using equipment such as paired gas-chromatography/mass-spectrometry (GC/MS) and solid-phase microextraction (SPM). While these techniques are highly accurate and have been shown to have low detection limits for acetone at 0.049 parts per billion (ppb), they do require high levels of experience to operate, are expensive to buy and maintain, and are more-or-less immovable. [8] All of these pitfalls limit them to becoming well-suited for point-of-care (POC) technology for disease monitoring and control.

Herein, a novel group of chemiresistive nanomaterials, metal doped tungsten oxide (MWO) nanorods, are extensively studied for their ability to work as a sensor for breath-acetone. A chemiresistive sensor has a simple design, which is described further on, that allows it to work as an easy-to-use POC device that is non-invasive and reusable. The goal of this research is to improve and better understand how tungsten oxide nanomaterials work as a transducer material for said device.

2.1.2. Chemiresistive Sensors

Chemiresistive gas sensors based on Metal-Oxide-Semiconductor (MOS), such as KWO, are becoming a more widely studied and available for biomedical applications. In contrast to the

methods previously mentioned, GC/MS and SPM, are simple devices which allow for a high miniaturization potential and have a low-cost output. All of this means they have the potential to become robust devices used in everyday clinical and personal settings. The chemiresistive mechanism for gas sensors, in short, is an observable change in electrical resistance when exposed to an analyte gas. The intensity and direction (increase or decrease) of resistance change is determined by the electrical and physical properties of MOSs. In addition, nanomaterial-based MOSs for biomedical sensors have been a widely studied area as of late due to nanomaterials possessing unique properties which aid in the sensing mechanisms. This is due to their high surface area to volume ratio, low cost, and tunable surfaces which allow for a wide range of study and application. [37]

Due to the wide variability nanomaterial MOSs present, changes in the electrical properties can be tuned to influence the final sensor's sensitivity, selectivity, productivity, and long-term stability. These are the main properties measured when testing a sensor's efficacy. Sensitivity is the sensor's ability to detect small changes in analyte concentration; selectivity is the ability to distinguish a single analyte from a complex chemical mixture; productivity is the reaction speed of the sensor, which can be broken down into response and recovery times; finally, long-term stability is the lifetime of the sensor, usually dictated by the transducing material. [38] Nanomaterial MOSs are highly attractive since all these properties can be easily manipulated through synthesis procedures that effect crystal size, structure, and surface functional groups.

To develop and improve the sensing-material's properties, three major functions, which drive the chemiresistive mechanism, must be considered: These functions are the receptor function, transducer function, and utility factor. [39-41] **Figure 4** illustrates these properties and

can give deeper understanding to how they affect overall sensitivity. The receptor function is most related to the sensitivity and selectivity of the produced material and dictates how said material will respond to the target gas. For MOS nanomaterials, oxygen vacancies are created at the surface of crystal structures during synthesis. The concentration of these oxygen vacancies directly impacts the sensing performance of MOS based gas sensors as these are the sites which the target gas will interact with. Beyond this, the ferroelectric property, present in $K_2W_7O_{22}$ (KWO) nanorods, creates a unique surface that allows for the receptor function to operate at room-temperature where non-ferroelectric MOS materials operate at temperatures well above 150 ^oC. [42]

The transducer function reveals how the response of each individual crystal translates to the overall response of the sensing film and continues to describe how free charge-carriers transfer within a crystal and across grain-boundaries. Theoretically, this function is caused by the formation of the depletion region between junctions or grains. MOS nanomaterials adsorb oxygen from the surrounding atmosphere, due to the receptor function, which attracts electrons forming O^-, O^{2-}, and O_2^- species. In an *n*-type MOS nanomaterial this causes an electron depleted layer, however as the topic of this dissertation is on a *p*-type MOS nanomaterial this function will be described assuming *p*-type response, which is the creation of a hole accumulation layer. The generated hole accumulation layer allows for easier flow of charge from one grain to the next as holes are the major charge carrier. Reducing gases, such as acetone, reacting with the surface of the material causes the hole density to decrease as the reduction reaction adds negative charge to the system. This causes a drop in charge mobility, which increases the resistance of the entire film. Reversely, oxidizing gases will increase hole concentration causing the resistance to

decrease. For a full picture, **Table 1** describes the interaction between *p*- and *n*-type MOS materials with reducing and oxidizing gases.

Table 1. Response behavior of p- and n-type MOS sensors to reducing and oxidizing gases.

Sensing Response Behavior	p-type Sensor	n-type Sensor	Example Gases
Reducing	Resistance increases	Resistance decreases	H_2, H_2S, CO, NH_4, Ethanol, Acetone, CH_4
Oxidizing	Resistance decreases	Resistance increases	O_2, O_3, NO_x, CO_2, SO_2

Lastly, the utility factor relates to the sensing material's morphology and porosity, which defines the diffusion and reaction of gases through the sensing medium. This directly impacts response and recovery times, so achieving high porosity will vastly improve the sensing films capability as a fast hand-held sensor. Here the morphology of the nanomaterial comes into play, as it dictates the porosity of the resulting film as well as the exposed reaction surfaces.

Chemiresistive gas sensor devices work using a mechanism mainly involving surface adsorption of an analyte and electrical signal transduction. Simply, this means the material's electrical resistance changes based on analyte concentration fluctuations. These devices are simple including a substrate, electrodes, and an active transducer layer. **Figure 5** shows a schematic of a typical chemiresistive sensor and the signal it presents when interacting with an analyte gas. The sensor response shown can then be quantified using an equation for sensitivity. The standard equation for sensitivity is presented here in equation (2.1):

$$S\ (\%) = \left(\frac{R_g - R_a}{R_a}\right) \times 100 \qquad (2.1)$$

Where R_g is the resistance when exposed to analyte gas, R_a is the resistance in air, and S is the calculated sensitivity expressed as a percent change from the controlled starting condition. The sensitivity is best improved by enhancing the transducer and/or the receptor function. Improving

the transducer function causes the difference in resistance between air and analyte gas environments to increase. This directly relates to the top-half of the equation creating a higher R_g - R_a value. On the other hand, the receptor function directly correlates to the value of R_a, which, when lowered, increases overall sensitivity. This will be the equation used when calculating sensitivity for all materials presented here-on.

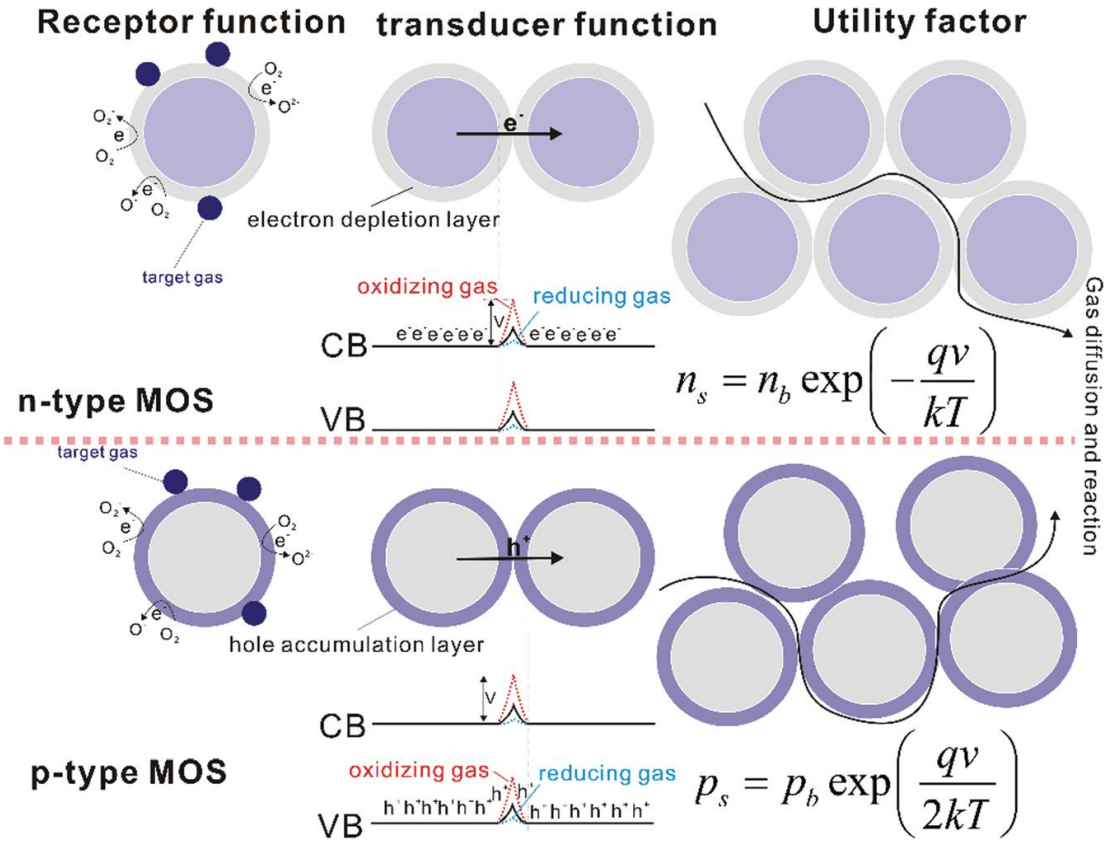

Figure 4. Three main factors controlling semiconductor gas sensor sensitivity Receptor Function, Transducer Function, and Utility Factor. [40]

Overall, all of these concepts are important towards the application of design and study of $K_2W_7O_{22}$ (KWO) nanorods for the application as a breath-acetone sensor. Herein, we will apply these concepts towards the experimentation and development of KWO for said sensing usage, and how factors such as growth temperature, potassium content, and the addition of surfactants affected the final measured sensing performance.

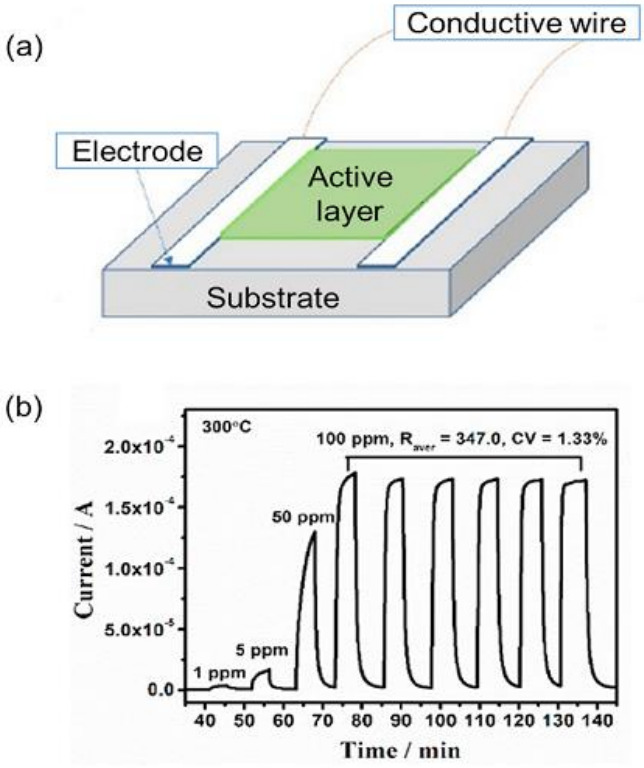

Figure 5. (a) Illustration of chemiresistive gas sensor. (b) Typical response and recovery curves measuring current when interacting with analyte gas at different concentrations. [39]

2.2. $K_2W_7O_{22}$ (KWO) Nanorods

KWO nanorods were the first tungsten oxide materials studied and comprise much of this work. This is due to the ferroelectric property they possess, which as discussed earlier, allow for this material to work at room-temperature. [42-44] This is notable as other MOS based sensors, including other tungsten-oxide based sensors, work at temperatures exceeding that of 150 ^{o}C. [45-52] Herein the effects of differing synthesis conditions are explored towards better understanding the crystal-structure, morphology, and ferroelectric property of KWO and how it pertains to the final sensing properties.

Initial literature research on tungsten oxides revealed that the ferroelectric phase stems from a specific crystal phase, called ε-WO_3. The ferroelectric property in ε-WO_3 creates a dipole within a crystal lattice structure by off-setting one or more atoms from their charge neutral

position. Due to this, high dipole moment compounds such as acetone will readily interact with the surface of the material. [51] The focus of this experimentation was to see if 1) ε-WO_3 was the cause of KWO's ferroelectric property, and 2) find if said phase could manipulated via synthesis conditions.

KWO is grown using the hydrothermal method. [53, 54] A precursor solution containing $Na_2WO_4 \cdot 2H_2O$ (95%, Alfa Aesar), oxalic acid dihydrate (>99%, VWR), K_2SO_4 (>99%, VWR), and HCl (36-38%, Aqua Solutions Inc.) was made. This solution was then put into a 30 mL autoclave for synthesis. KWO samples were grown at various temperatures for 24 hours. The collected material is then washed with D.I. water and ethanol then collected via centrifuge. Samples used for acetone sensing tests were applied to a sensor slide, which consists of a glass substrate and gold-patterned electrodes, by blade coating and then annealed at 350 ^oC for better contact with the substrate as well as improving crystallinity.

2.2.1. Growth Temperature Effects

As this material is new, it must be determined what the best synthesis conditions are. To do this a round of experimentation was done growing four samples of KWO at temperatures of 160, 180, 210, and 225 ^oC using the hydrothermal method described earlier. These samples were then examined using X-ray diffraction (XRD), transmission electron microscopy (TEM), Raman spectroscopy, Fourier-transform infrared (FT-IR) spectroscopy and were all tested for sensing performance. [51]

2.2.1.1. X-Ray Diffraction (XRD) and X-Ray Photoelectron Spectroscopy (XPS)

X-ray diffraction was obtained using a Bruker AXS D8 Discover to study as-synthesized KWO crystalline structure. Samples were made by coating a paste made from KWO and ethanol on glass substrates. A diffraction pattern was gathered from a 2-Theta of 5^o to 90^o.

Figure 6 shows the XRD spectra of KWO grown at 160, 180, 210 and 225 ^{o}C. The individual peak's 2-θ values found were: 14.013^{o}, 23.265^{o}, 24.339^{o}, 27.269^{o}, 28.175^{o}, 33.896^{o}, and 36.843^{o} corresponding to the crystal indices of *(100)*, *(002)*, *(110)*, *(101)*, *(200)*, *(111)*, and *(201)*, respectively. It was found that the crystal structure of KWO was similar to results found for other hexagonal tungsten oxides used for gas sensing. [50, 55, 56] The peak positions remain constant with respect to growth temperature indicating that the growth temperature did not alter the crystal structure. The main differences that can be observed in these samples from XRD are 1) stronger peaks are observed for samples grown at higher temperatures, and 2) the relative peak intensities of *(200)* and *(201)* facets become much more intense with respect to other peaks as the growth temperature was increased. In summary, nanorods grown at higher temperature presented higher crystallinity with the *(200)* facet becoming much more prevalent than other peaks with respect to increasing growth temperature.

X-Ray Photoelectron Spectroscopy (XPS) was done using a Thermo Scientific K-Alpha XPS to study the molar value of each type of atom in KWO. Samples were collected and annealed as a powder for analysis. The results can be seen in **Figure 7** which the analysis can be found in **Table 2**. The values found show that the molar ratio of the material obtained is very close to the 2:7:22 of K:W:O as expected.

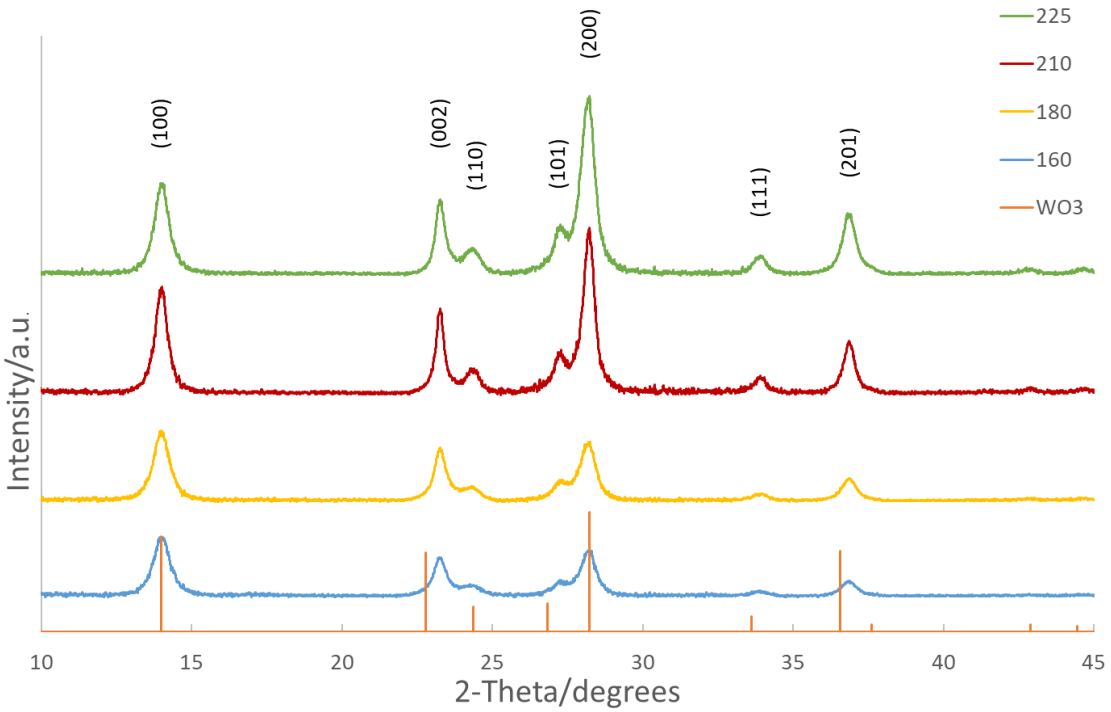

Figure 6. XRD spectra of KWO growing at 160, 180, 210, 225 ^{o}C and standard WO_3.

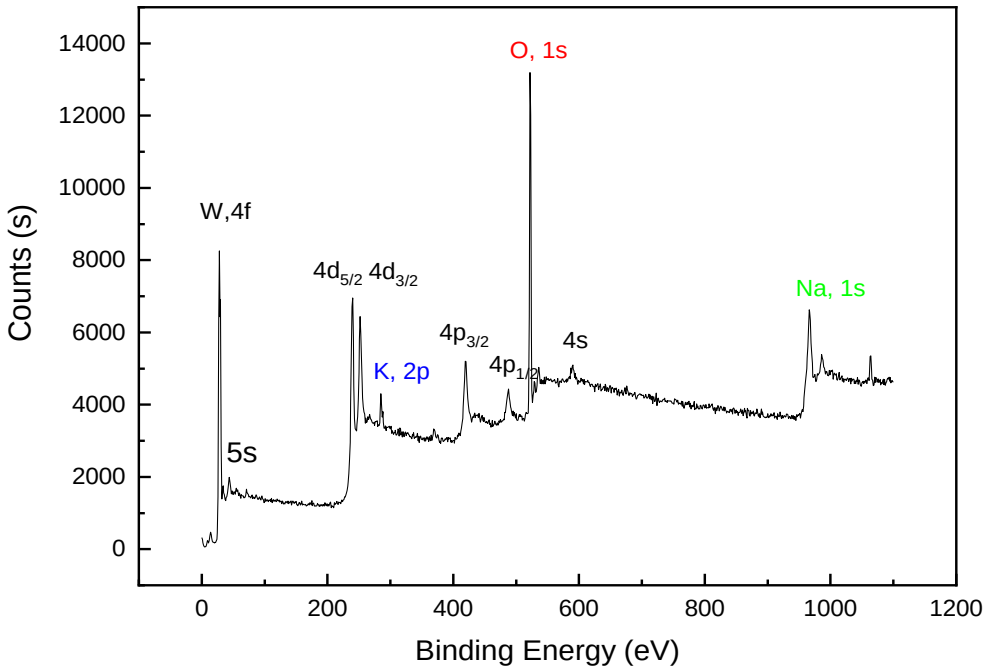

Figure 7. XPS Spectrum of $K_2W_7O_{22}$ nanorods.

Table 2. XPS data of as-synthesized KWO.

	Peak (BE)	Height (CPS)	FWHM (eV)	Area (CPS.eV)	Atomic Content (%)
W_{4f}	36.36	421721.42	4.08	1798872.21	23.41
O_{1s}	530.34	334091.36	2.59	995253.52	68.46
K_{2p}	239.29	38855.81	2.70	168932.44	6.05

2.2.1.2. Transmission Electron Microscopy (TEM)

TEM imaging was obtained using a JEOL JEM-2100 high-resolution analytical TEM. Samples were prepared on carbon grids by sonication. **Figure 8** shows the TEM images of the nanorods to see the typical length at all four growth temperatures. It can be seen that the higher the temperature the longer the nanorods were. It can also be noted that the average dimeter of the nanorods across all samples is about 10 nm indicating that growth temperature does not affect the thickness of the synthesized product. Also of note, the sample grown at 225 ^{o}C have become much longer on average compared to the other samples indicating a faster growth rate.

Figure 9 presents TEM imaging which the crystal lattice has become apparent for the four samples grown at varying temperatures. The lattice-fringe spacing found from these images are presented in **Table 3**. Looking at this data, it can be seen that this spacing does not vary much indicating little change to crystal morphology with respect to growth temperature. This correlates well with the XRD data presented earlier in **Figure 5**.

Table 3. Lattice fringe spacing for KWO samples grown at 160, 180, 210, and 225 ^{o}C.

Growth Temperature (^{o}C)	*a-spacing (Å)*	*c-spacing (Å)*
160	6.038	3.598
180	6.320	3.636
210	6.356	3.634
225	6.388	3.542

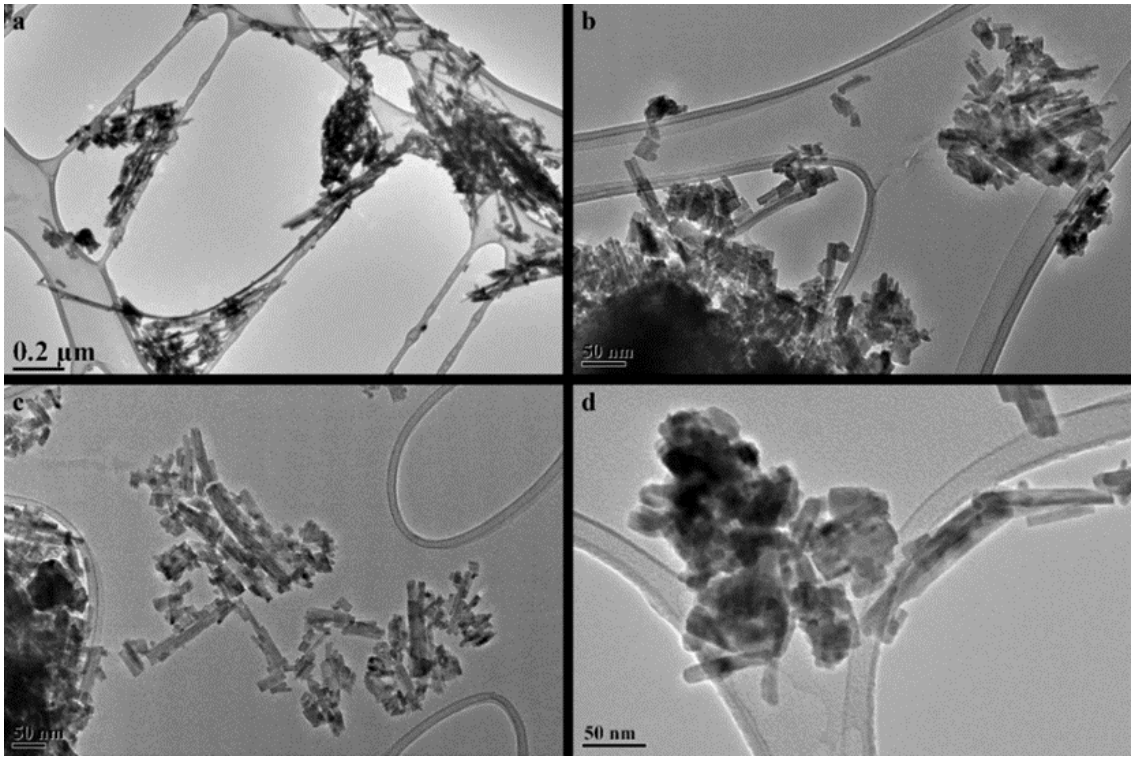

Figure 8. HRTEM image of KWO samples grown at (a) 225 (b) 210, (c) 180, and (d) 160 ^{o}C.

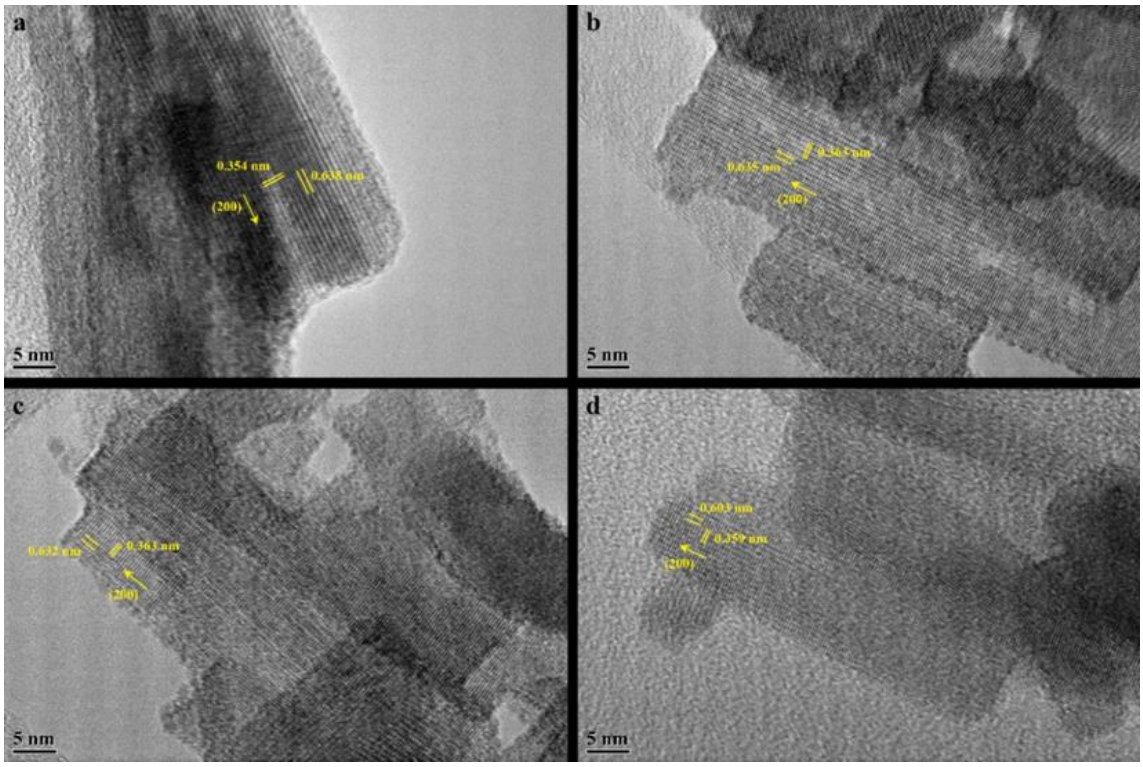

Figure 9. HRTEM image of KWO lattice, samples grown at (a) 225 (b) 210, (c) 180, and (d) 160 ^{o}C.

2.2.1.3. Raman Spectroscopy

Previously, our group has shown that KWO presents the ferroelectric property using a piezoresponse force microscope. [42] Raman spectroscopy was used to further study the ferroelectric property of KWO in this study. Previous reports have found that WO_3 exhibits this property in a bulk phase called ε-WO_3 which is only stable below -40 ^oC, and normally exists in the γ-phase of WO_3 at room-temperature. [52] However, it has also been found that ε-WO_3 can exist at room temperature as microcrystals in a bulk sample. [57] Raman has been utilized in other studies to better understand the effect that doping has on the crystal phase WO_3 expresses and study the material's ferroelectric property. [49] Here, we used Raman spectroscopy to find peaks at room temperature, which can provide evidence of the existence of ε-WO_3 within the KWO crystal phase at room temperature.

Raman spectra were obtained using an Aramis Confocal Raman Imaging System with Horiba Jobin Yvon's Raman Spectrometer. **Figure 10** shows the spectra obtained of KWO grown at 160 and 225 ^oC. Both samples show peaks at ν= 642, and 688 cm^{-1} which belong to the ε-phase of WO_3. [58] These results confirm that the ε-WO_3 phase is present within the samples made. Factoring this in, the KWO grown at 225 ^oC shows further extended shoulder comparing to the sample grown at 160 ^oC indicating that KWO grown at higher temperature presents more ε-WO_3 and thus a stronger ferroelectric property.

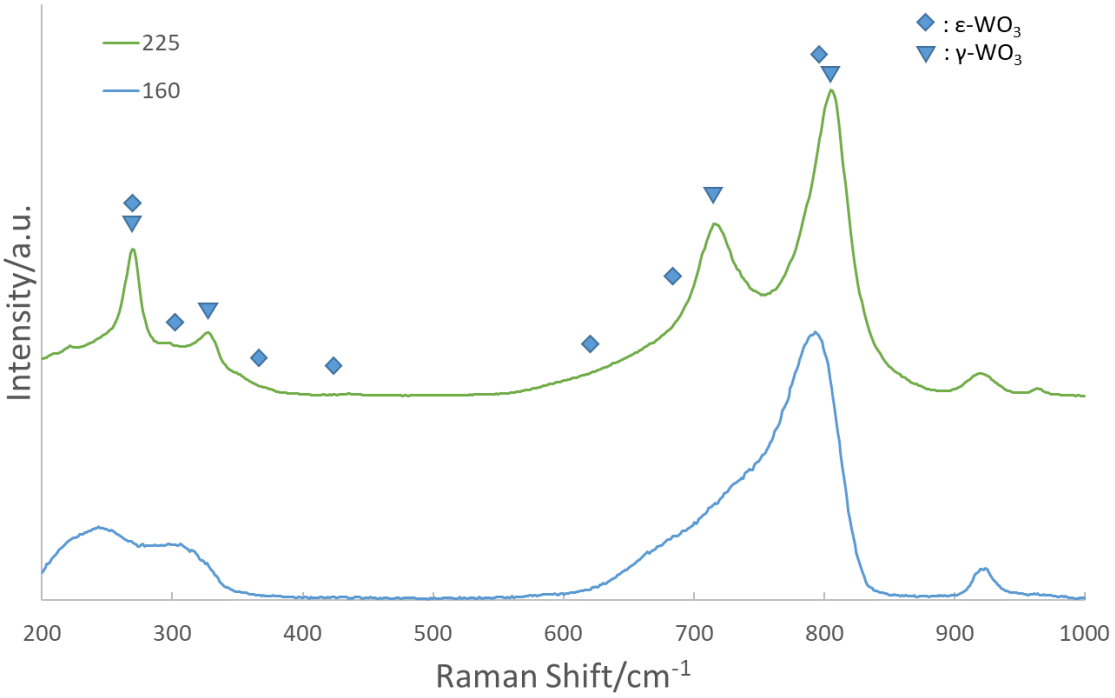

Figure 10. Raman Spectra of KWO grown at 160 °C and 225 °C.

2.2.1.4. Fourier-Transform Infrared (FT-IR) Spectroscopy

Further structural and functional groups of KWO grown at 160 °C and 225 °C were studied using FT-IR, see **Figure 11**. It has been reported the WO_3 nanostructures can contain water within the crystal structure. [54, 59] This is confirmed in our results showing a wide band at ν= 3,410 cm^{-1} and weak peak at ν= 1,590 cm^{-1}. These peaks can be attributed to -OH and H_2O stretching vibration. A strong band at ν= 806 cm^{-1} with shouldering at ν= 716 cm^{-1} corresponds to O-W-O stretching vibration. This peak is stronger in the sample grown at 225 °C, and this is likely due to the higher crystallinity which was presented earlier. Also, weak shouldering at ν= 1,030 cm^{-1} can be attributed to the W=O vibrational mode. A weak peak at ν= 1,380 cm^{-1} is attributed to W-OH. Interestingly, this peak only shows up for KWO synthesized at 225 °C indicating isolated hydroxyl groups only in this sample. From this data, we can see that KWO grown at higher temperatures presents **-OH terminations** while samples grown at lower

temperatures do not. It has been shown that the –OH terminations can cause electrostatic interactions between the material and high dipole analytes such as acetone. [60] The increased electrostatic interaction with acetone likely causes an improvement in sensing performance.

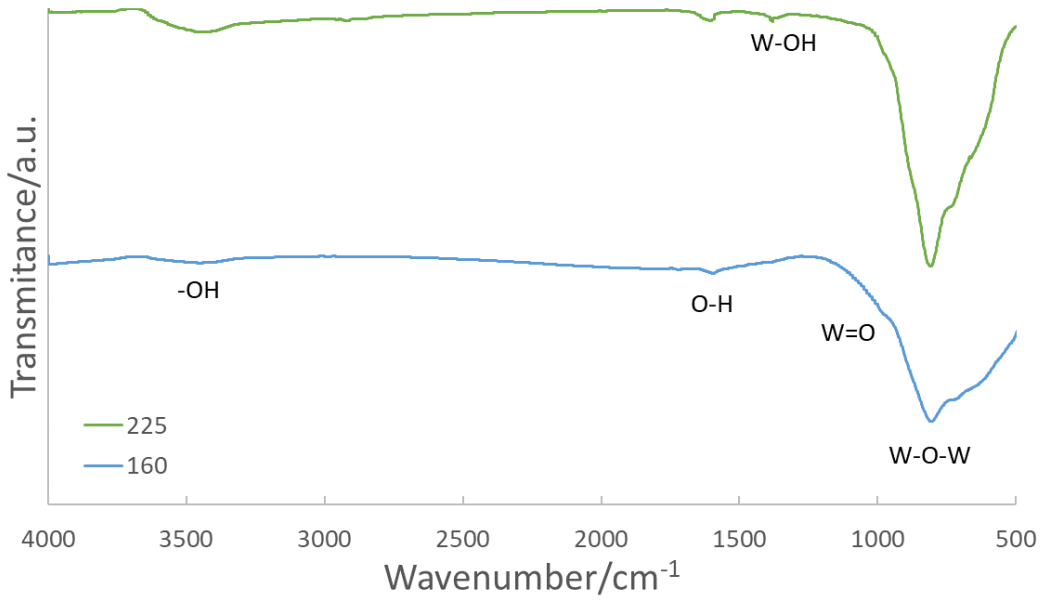

Figure 11. FT-IR spectra of KWO grown at 160 and 225°C.

2.2.1.5. Acetone Sensing and Discussion

The acetone sensing performance has been done through a programmable chemiresistive gas sensor measurement system. [42, 43] Briefly, the acetone vapor is generated from OVG-4 (Owlstone, InC.) based on the theory of permeation tube. The concentration of acetone can be precisely controlled from 0 to 5 ppm. Higher concentration, 50 ppm, acetone is generated from acetone tank in dry nitrogen calibrated and made by Airgas, Inc. Once the acetone is exposure onto KWO film, a resistance change can be detected and recorded through an advanced circuit system designed for signal collecting.

The sensing tests based on the as-synthesized KWO at different fabricating temperature to 50 ppm of acetone have been done. Sensitivity to acetone was determined based on the typical

equation for a chemiresistive sensor, as described earlier in the introduction of the chapter, to evaluate KWO sensing performance. Based on this equation, the sensitivity for KWO grown at 160, 180, 210, and 225 ^{o}C was calculated and shown in **Figure 12**. As we can see, the sensitivity increases as growth temperature increases as far as the temperature is not too high to cause any phase transition. While the data shows the highest growth temperature, 225 ^{o}C, is in fact the most sensitive to acetone, the samples could become even more sensitive at even higher growth temperatures. However, this was unable to be tested as the equipment available was only capable of temperatures at the maximum shown here.

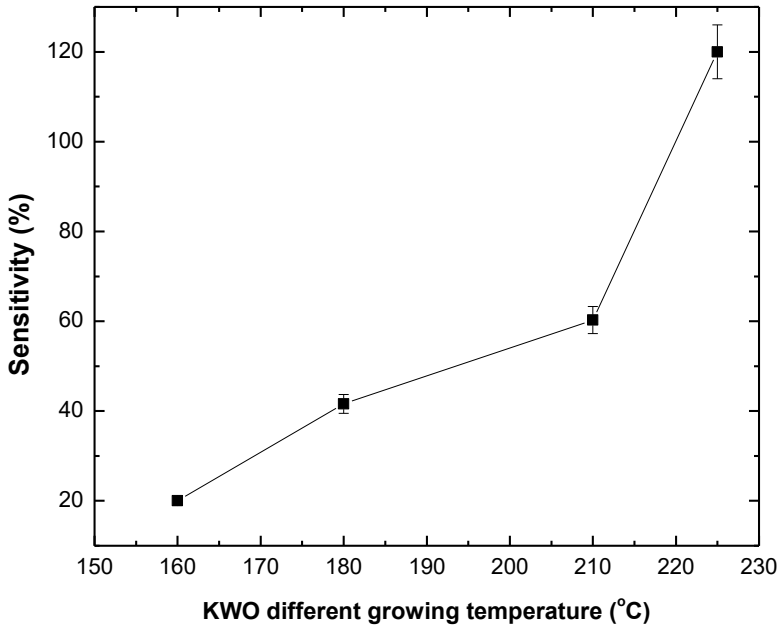

Figure 12. Sensitivity to acetone (50ppm) using KWO grown at 160, 180, 210, and 225 ^{o}C.

Considering the results of XRD and HRTEM, in **Figures 1** and **4** respectively, the results have shown that 225 ^{o}C KWO has higher crystallinity and longer nanorods. The sensing test results reveal that higher crystallinity and larger surface area can be one reason to result in better response of KWO to acetone. Also, an increased ferroelectric property, measured using Raman spectroscopy shown in **Figure 10**, can be another important factor that results in the higher

response of KWO to acetone. Due to the ferroelectric property being so important to the charge transfer between acetone and KWO, this indicates that improving this property is important to further improve KWO sensing performance to detect acetone. [49]

The selectivity of the material is also another important factor the future use of this material for an application in a diabetes monitoring device. We have previously reported the selectivity of this material to being most sensitive to acetone over ethanol and water vapor. [42] We have also reported on the humidity cross-interference effect showing that this material works even in environments with high humidity (relative humidity up to 80%). [61] It has been highly reported that environments with high humidity are problematic to semiconductor sensors, and since KWO operates at room-temperature and can operate at high humidity shows the quality of this material for use in an acetone sensor for human breath. Due to this fact, continual experimentation will be done to find ways to mitigate the humidity cross-interference effect to achieve suitable operation in environments of a relative humidity greater than 90%, and to increase the selectivity for acetone further in future work.

Overall, the goal is to create a working medical device based around this material that can detect acetone on human breathe and correlate that to blood-glucose levels. The obvious next step to achieve this is to begin tests using human breath samples of those with diabetes. This would show the viability of this material in more real-life circumstances. Also, our group is working on designing the circuits and fabrication of a portable device for easy convenient use. Accomplishing these two objectives would allow for KWO to become a staple for diabetes health detection and monitoring.

$K_2W_7O_{22}$ nanorods synthesized at temperatures from 160 to 225 ^oC were characterized and studied for beneficial properties applicable to acetone sensing. It was found that when KWO

was grown at higher temperatures it exhibited higher crystallinity, longer nanorods, more –OH termination, and a more prominent ferroelectric property. The more prominent ferroelectric property was shown to be the main reason why KWO synthesized at higher temperatures became more sensitive to acetone. It has been shown here for the first time that the optimization of growth temperature directly affects the ferroelectric property, and thus the sensitivity of the resulting material. Other important factors such as more –OH termination, higher surface area due to longer nanorods, and higher crystallinity also show impact on the overall sensitivity of the material to acetone. Overall, the KWO grown at higher temperatures has been shown to be an improvement for the material's sensing properties for diagnosing and monitoring diabetes.

2.2.2. Potassium Content and Surfactant Effect on KWO's Ferroelectric Property and Crystal Structure

It has been shown that manipulating the surface facets of WO_3 nanomaterials can greatly impact their sensing properties. [50] The addition of surfactants during growth can influence the morphology and surface facets. [62] So, we have tried manipulating the specific surface facets of KWO via growth using surfactants and studied the role of potassium (K) in KWO. The results show that both K and surfactants influence KWO sensing performance. Like several other nanomaterials, gas sensing capability is dependent on the exposed planes of the crystal structure, and exposed crystal facets. [49, 50, 62-66] From there, it will help us to better understand the relationship of KWO material structure and properties. As mentioned earlier, KWO has a strong room-temperature ferroelectric property that drives the mechanism of acetone sensing, and the ferroelectric property has been shown to be correlated to the ε-WO_3 phase of WO_3. [58] By manipulating the surface facets and the potassium concentration a better understanding of the KWO acetone sensing mechanism is presented, and further improvement of the material for its

use in an acetone breath sensor as a diabetes diagnosis and monitoring device is accomplished. [67]

KWO is grown using the hydrothermal method described earlier. For surfactant growth poly(ethylene glycol)-*block*-poly(propylene glycol)-*block*-poly(ethylene glycol) (designated PEG-PPG-PEG; Pluronic L-121, Sigma-Aldrich) was added to the precursor solution last and let stir for 10 minutes before beginning hydrothermal growth. Additionally, precursor solutions of varying K_2SO_4 concentrations to obtain the products $K_xW_7O_{22}$ with x = 1.2, 1.5, 1.8, 2.0, and 2.2 were made for testing how potassium content affects sensitivity of the final sensing material.

2.2.2.1. X-Ray Diffraction (XRD)

XRD patterns were collected on a Bruker AXS D8 Discover to study as-synthesized KWO crystalline structure. Samples were made by blade coating a paste made from KWO powder and ethanol on glass substrates. A diffraction pattern was gathered from a 2-Theta of 10^o to 45^o.

Previous work has shown that the crystal structure of KWO is similar to that of hexagonal tungsten trioxide (*h*-WO_3), and that it can be tuned for higher acetone sensitivity by adjusting the growth temperature. [42] It has been reported that the controlled exposure of the crystal facets of WO_3 have a high impact on acetone sensitivity and selectivity. [50] According to this information, we have modified KWO in a similar fashion to gain more control over the crystal surfaces exposed as shown in **Figure 13**. The introduction of the Pluronic L-121 surfactant has effectively changed the ratios of surface facets while still maintaining the same peak positions indicating the sample maintained a hexagonal lattice structure. So, to compare the samples the ratio of the *(002)* and *(200)* peaks were obtained. KWO grown without surfactant shows a ratio of 0.426, and the addition of L-121 increases this ratio to 0.814. By utilizing a

surfactant growth method, the facets have been altered enough to see if there will be a change in the materials sensing property which will be discussed further on. **Figure 14** shows the XRD for the samples with varying stoichiometric ratios of potassium. The general chemical formula of $K_xW_7O_{22}$ where x was equal to 1.2, 1.5, 1.8, 2.0, and 2.2 for varying samples was used. The first thing that should be noted is similarly to growing with a surfactant, the potassium level directly controls the ratio of crystal facets. It can be seen that the *(200)* peak sharply increases at a K value of 1.5 and lower, while the *(002)* peak gets significantly larger at a K value of 1.8 and above. Overall, we can see that with a lower concentration of K the *(002)* peak decreases and the *(200)* peak increases, and vice versa for increasing potassium concentration.

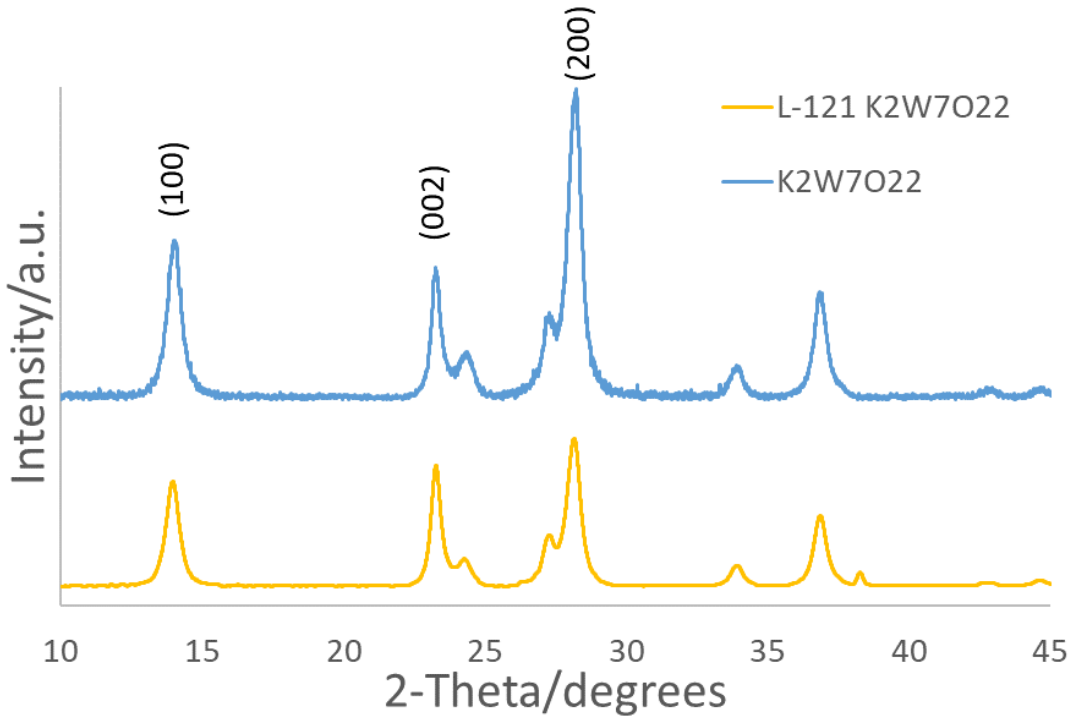

Figure 13. XRD of KWO grown with and without L-121 surfactant.

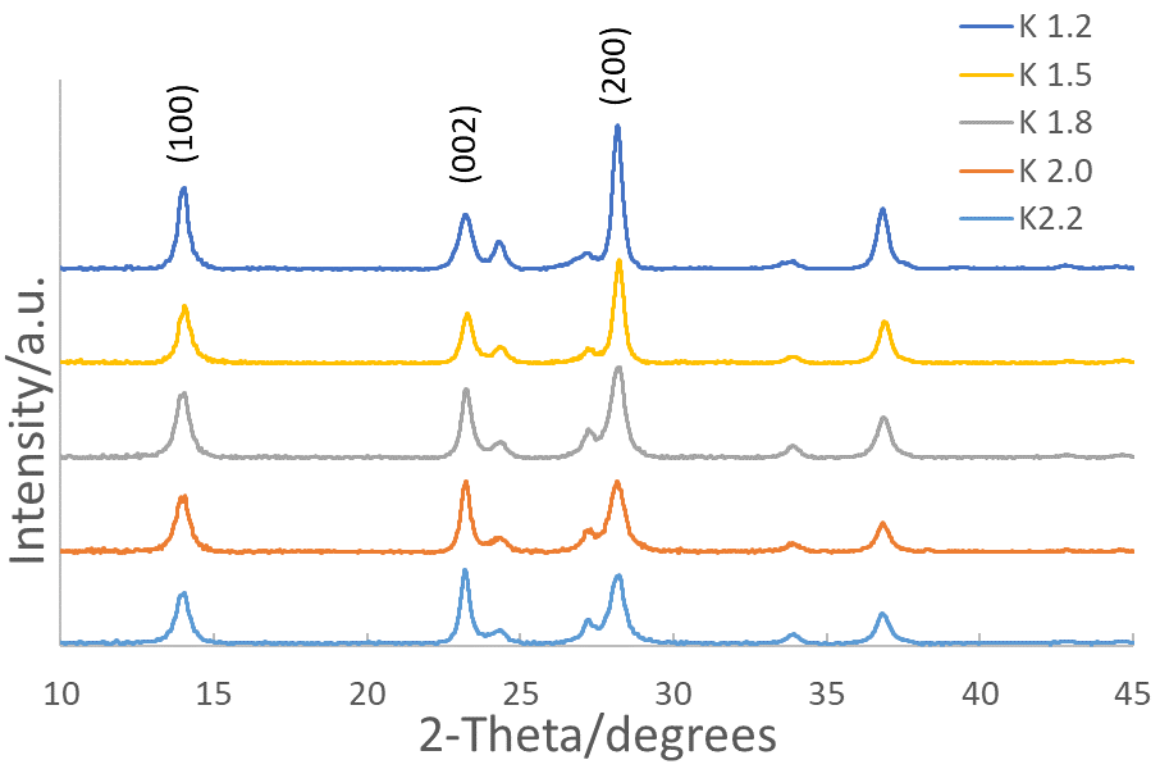

Figure 14. XRD of KWO grown varying stoichiometric potassium compositions of 1.2, 1.5, 1.8, 2.0, and 2.2.

The data gathered by XRD indicated that control of the crystal facets of KWO material can be achieved via two pathways: addition of chemical additives during growth such as surfactants, and the adjustment of the concentration of potassium in KWO.

2.2.2.2. Raman Spectroscopy

Figure 15 shows the Raman obtained of KWO samples grown with and without L-121, and **Figure 16** shows samples with a change in potassium content. Comparing K_x values of 1.8, and 2.0 when grown with L-121, we see little difference other than a more prominent ferroelectric phase observed by farther shouldering which was previously reported by our group. [51] In detail, in Figure 2, there are two primary peaks at 715 cm^{-1} and 805 cm^{-1} in Raman spectra which indicate the presence of γ-phase. With addition of L-121 a decrease of peaks

related to γ-phase was seen in $K_{1.8}$WO-L121 and $K_{2.0}$WO-L121. Instead, one primary peak just below 800 cm^{-1} was showing up which is indicated a further shift to the ε-phase. [49, 51] This result combining the XRD data indicate KWO grown with L-121 has a stronger ferroelectric phase as well as higher ratio of *(002)* facet.

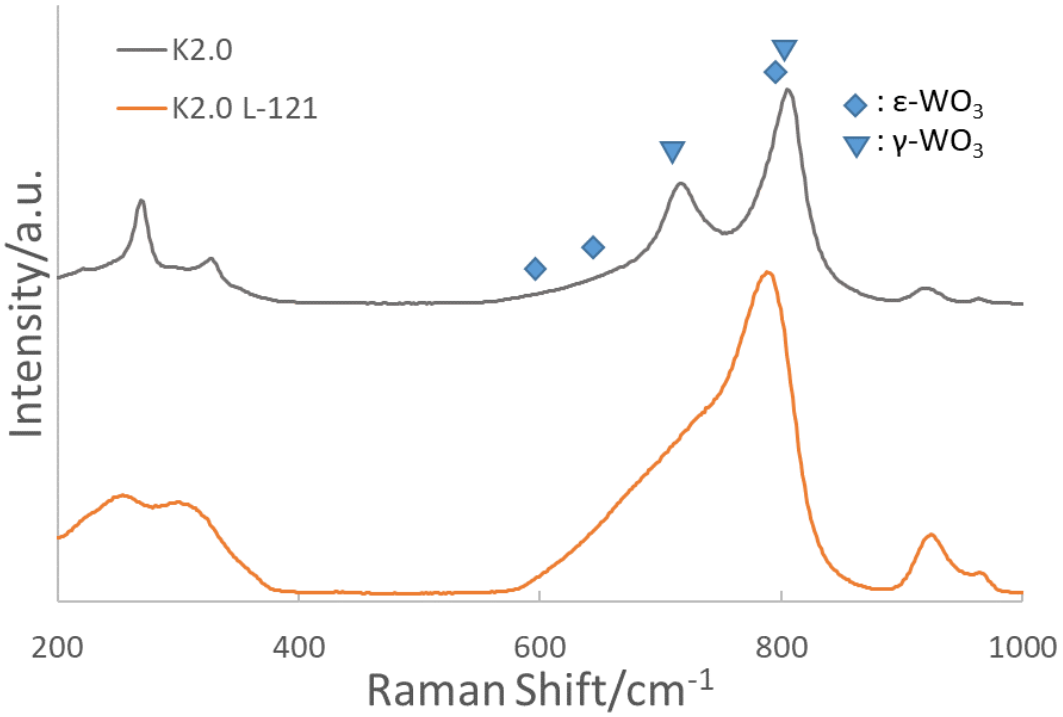

Figure 15. Raman of $K_2W_7O_{22}$ grown with and without L-121 surfactant.

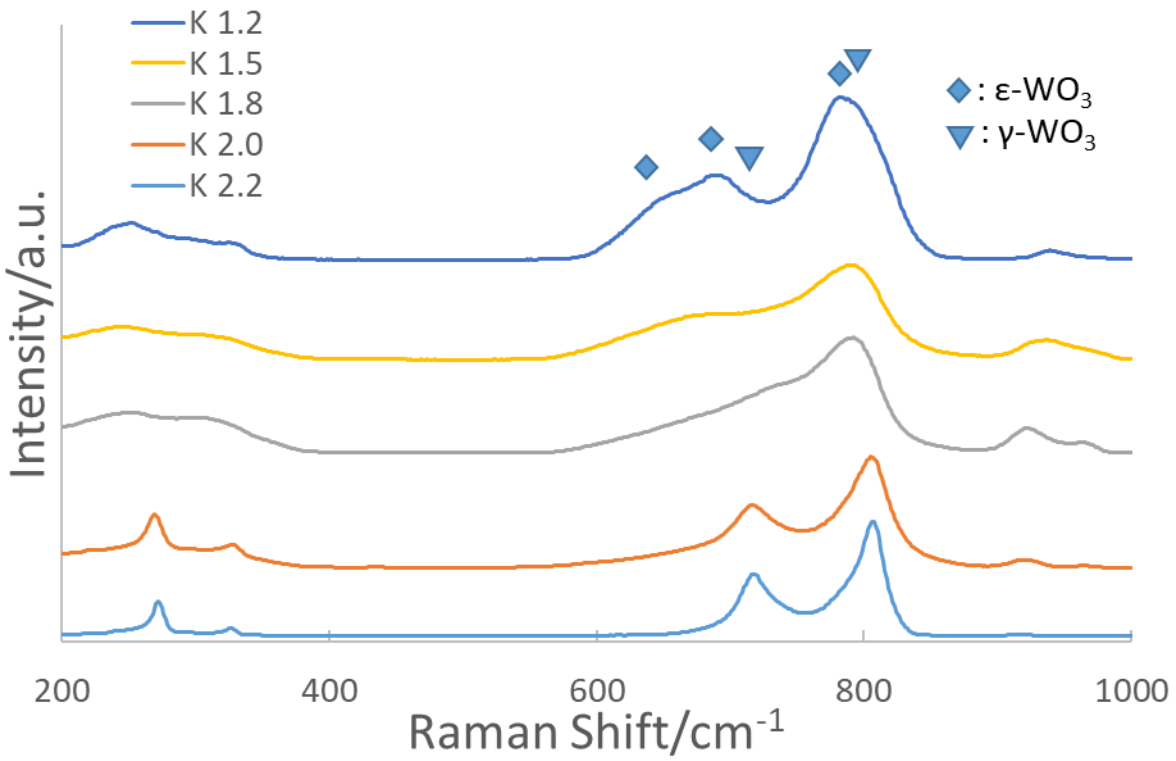

Figure 16. Raman of KWO with potassium stoichiometric ratios of 1.2, 1.5, 1.8, 2.0, and 2.2.

We can also see in **Figure 16** a clear shift from the *gamma* phase to the *epsilon* phase of WO_3 when potassium levels are decreased. This is similar to the results found when doping with chromium where a decrease in doping yielded more ε-WO_3. [49] That is, it is critically important to find the right component ratio of K in KWO in order to optimize KWO sensing performance. This is because both ferroelectric phase and *(002)* surface play an important role in KWO as an acetone sensing material. To elaborate, if the potassium content of KWO is too high, we see a strong drop in the ferroelectric phase. While, if the potassium content is too low, we see less expression of the *(002)* facet. This lets us conclude that there must be a balance where the potassium levels express enough of each property to maximize the material's sensitivity.

2.2.2.3. Fourier-Transform Infrared (FT-IR) Spectroscopy

Figure 17 shows the FT-IR of the obtained samples grown with and without L-121. The peak at ν= 3,410 cm-1 and weak peak at ν= 1,590 cm-1 can be attributed to -OH and H2O

stretching vibration. A strong band at ν= 806 cm-1 with shouldering at ν= 716 cm-1 corresponds to O-W-O stretching vibration. Also, weak shouldering at ν= 1,030 cm-1 can be attributed to the W=O vibrational mode. A weak peak at ν= 1,380 cm-1 is attributed to W-OH. Overall, we can conclude from this data that there is no significant change with the surface functionalization of the material. So, any sensing changes that do occur are solely from the changing of the crystal facets and structure expressed.

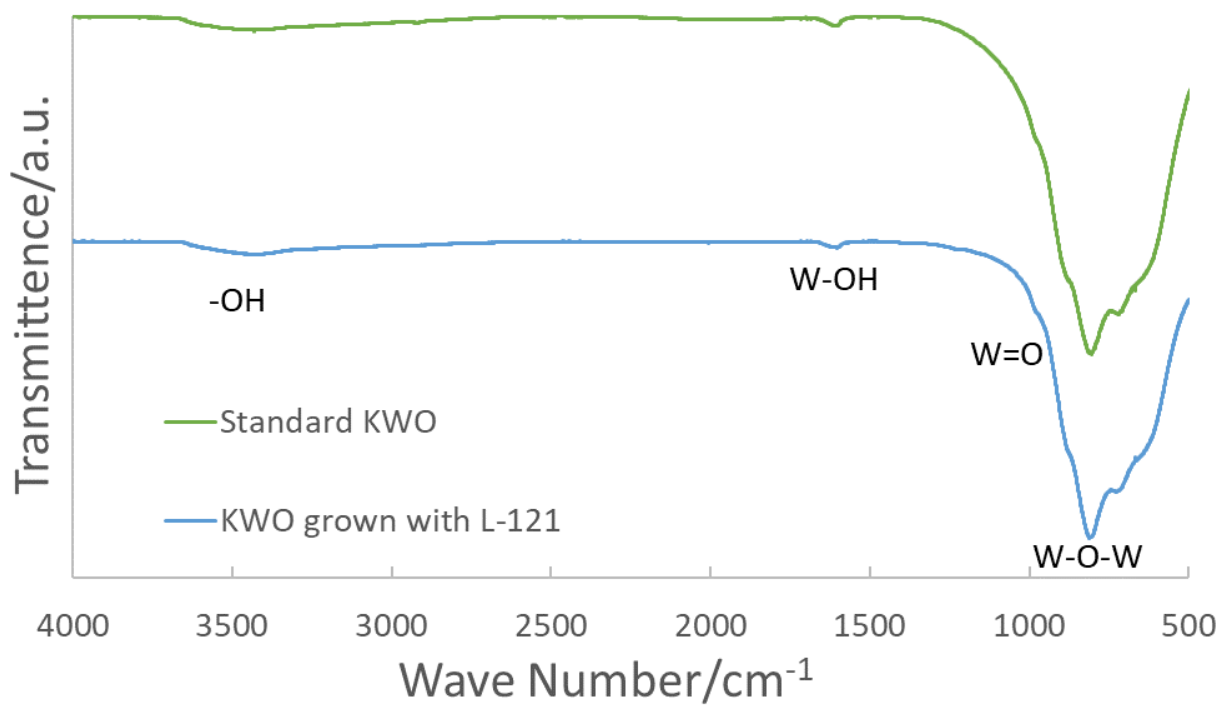

Figure 17. FT-IR of KWO grown with and without L-121.

2.2.2.4. Acetone Sensing, Selectivity, and Discussion

To exam the importance of potassium and L-121 in KWO, the sensing test by using different potassium concentration has been conducted. The results are shown in **Figure 18**. This figure presents the sensitivity of 25 ppm acetone detection using KWO samples made with different K concentration and surface modification using L-121.

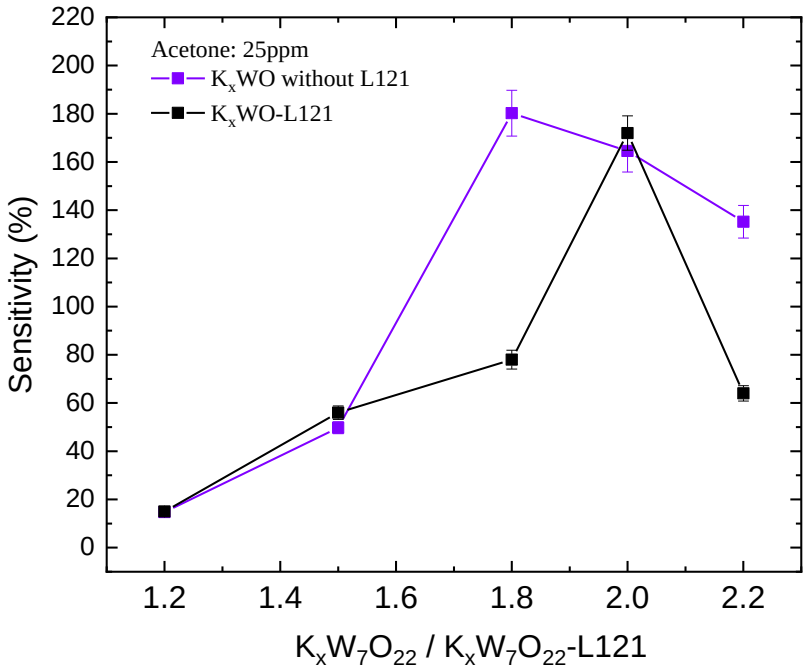

Figure 18. Sensing response to 25 ppm acetone using K_xWO grown with and without L-121.

The sensitivity was calculated using the standard equation used to study gas-sensor sensitivity. As we can see, the best sensing performance needs to balance the concentration of potassium in K_xWO and surfactant L-121 treatment. Looking at **Figures 14** and **16** we see that this would make the most sense. This is because the *(002)* peak is relatively stronger compared to other peaks, as well as the ferroelectric phase, ε-WO_3, is more present in the sample of $K_{2.0}WO$-L121. This result confirms that both surface facet *(002)* and ferroelectric phase play an important role in KWO sensing to acetone.

Another important factor of a sensor's performance is the selectivity. **Figure 19** is the selectivity testing on 2.85 ppm of different chemicals such as acetone, ethanol, methanol, and water vapor for $K_{2.0}WO$-L121. This indicated that KWO with a potassium level of 2.0 treated with L-121 shows the interaction with acetone has the highest sensitivity and selectivity. That is, by manipulating the crystal facets of the KWO material, we found that the *(002)* peak does in

fact have an important role for sensing acetone. Although the detailed explanation is still under investigation at current stage, we can briefly theorize that a higher number of coordinated unsaturated O atoms on the surface of the *(002)* facet than the *(100)* or *(200)* facet could be one factor. These O atoms allow for easier interaction leading to larger charge transfer from gas to material surface. Also, it has been reported that the O atoms on the *(002)* surface facet are asymmetrically arranged which leads to a non-uniform distribution of the electron cloud-surface causing ferroelectricity. [50] This asymmetrical electron cloud makes the *(002)* facet form a local electric polarization allowing for dipole-dipole interaction between acetone and other molecules. Considering that acetone is a chemical with higher dipole moment than ethanol, methanol, and water; these results are an example of the good selectivity of KWO-L121 as an acetone sensing material.

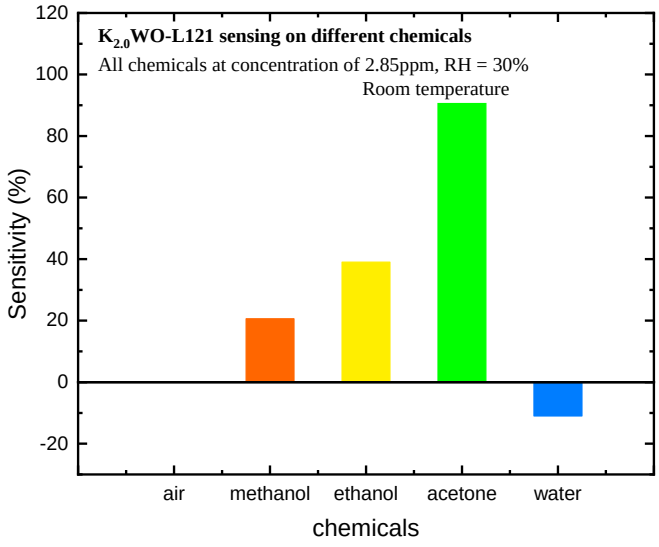

Figure 19. Selectivity testing of K2.0WO-L121 to 2.85ppm of acetone, ethanol, methanol, and water vapor (the concentration of air is arbitrary).

The ferroelectric property of KWO is not the only property that is important for acetone sensing. This study has shown that the surface facet *(002)* expressed also has an important role in the material's sensing properties. In summary, firstly, it was shown that utilizing a surfactant (L-

121) during growth could influence the surface facets expressed of the final material, and it was proven to not be an effect from having different functional groups via FT-IR. Secondly, we have shown that the concentration of potassium, K in KWO, can directly affect expressed facets, as well as the ferroelectric phase of the final product. On the other hand, our results revealed that a balance is needed between exposed surface facets and the ferroelectric property to optimize KWO sensing response to acetone. We have observed this balance to be a stoichiometric ratio of 2:7:22 of K, W, and O respectively. Also, the introduction of L-121 during hydrothermal growth can create a more selective material toward acetone. This would allow for much more reliable readings when it is applied to a device for diabetes diagnosis and monitoring. Work in the future should include finding other methods to maximize the ferroelectric property while keeping acceptable exposed surface facets for acetone detection. In a word, the manipulation of stoichiometric potassium levels as well as the introduction of L-121 during hydrothermal growth can improve KWO sensing properties to detect acetone for great potential application in non-invasive diabetes diagnosis and monitoring.

2.3. Exploration Beyond Potassium-Tungsten Oxide

Other metals beyond potassium have also been tested for their efficacy as possible Metal-Tungsten Oxide (MWO) breath acetone sensors. Synthesis of these samples was done using the standard synthesis procedure for KWO except K_2SO_4 is replaced by another metal-sulfate using an equivalent molar amount to K, *i.e.* Li_2SO_4 would use the same molar amount as K_2SO_4 would, and $CuSO_4$ would use twice the molar value of K_2SO_4 to account for the molar difference in the chemical formula to achieve full molar equivalence. **Table 4** further elaborates this by showing the ratio of moles of each metal sulfate used in this study compared to every mole of K_2SO_4 used. This was done as to directly compare to KWO as the standard.

Table 4. A comparison of moles metal-sulfate used to match the full-, half-, quarter-, and eighth-molar equivalence of a 1 mole standard of K_2SO_4.

Sulfate	Full	Half	Quarter	Eighth
K_2SO_4	1	0.5	0.25	0.125
Na_2SO_4	1	0.5	0.25	0.125
Li_2SO_4	1	0.5	0.25	0.125
$Cr_2[SO_4]_3$	1	0.5	0.25	0.125
$CuSO_4$	2	1	0.5	0.25
$La_2[SO_4]_3$	1	0.5	0.25	0.125
$SnSO_4$	2	1	0.5	0.25

2.3.1. Alkali Metals

Both Li_2SO_4 and Na_2SO_4 were tested in replacement of K_2SO_4 in the standard synthesis procedure creating a lithium-tungsten oxide (LiWO) and a sodium-tungsten oxide (NaWO). The resulting materials were tested for their efficacy as acetone sensors and studied using XRD, SEM, and Raman spectroscopy. Additionally, composite metal systems were synthesized using a lithium and a potassium source in samples at varying ratios.

2.3.1.1. X-Ray Diffraction (XRD)

XRD patterns were collected on a Bruker AXS D8 Discover to study as-synthesized alkali-metal tungsten oxide crystalline structure. Samples were made by blade coating a paste made from powder and ethanol on glass substrates. A diffraction pattern of each sample was gathered from a 2-θ of 10^o to 70^o and can be seen in **Figure 20.**

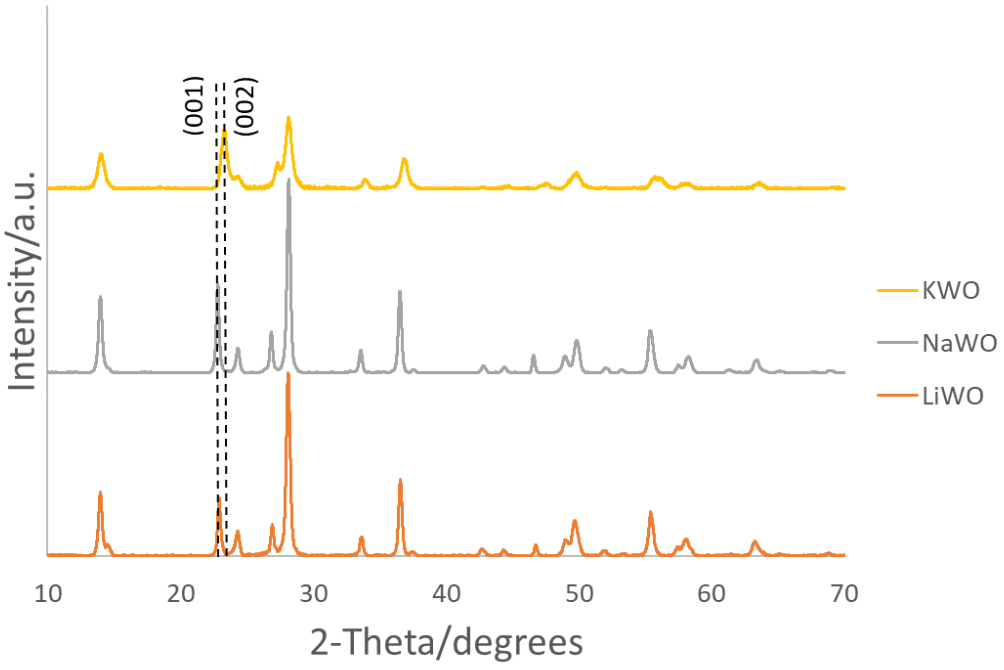

Figure 20. XRD of tungsten oxide nanorods with the alkali metal additives of K, Na, and Li.

At first glance, all samples shows peaks which correspond to the hexagonal tungsten trioxide phase (*h*-WO_3) at 2-θ values of 13.9º, 22.8º, 24.3º, 26.8º, 28.2º, 33.6º, 36.5º, 49.9º, and 55.5º. Additional peaks in the diffraction pattern can occur due to a change in metal ion, which act as a capping agent directing growth, causing slight impurities. [50] Upon closer inspection, both the Li and Na samples present a similar hexagonal phase to KWO. However, they present the *(001)* facet instead of the *(002)*. This is important as it has been found that the *(002)* facet is in fact important for tungsten oxide acetone sensors as discussed earlier. [50, 67] Beyond this, it can also be noted that the *(200)* peak is relatively less expressed indicating less expression of this crystal facet when grown with K_2SO_4.

Samples were also grown with respective ratios of 1:1, and 3:1 of K_2SO_4:Li_2SO_4 and compared to the pure LiWO and KWO counterparts. The XRD pattern of these samples can be found in **Figure 21.**

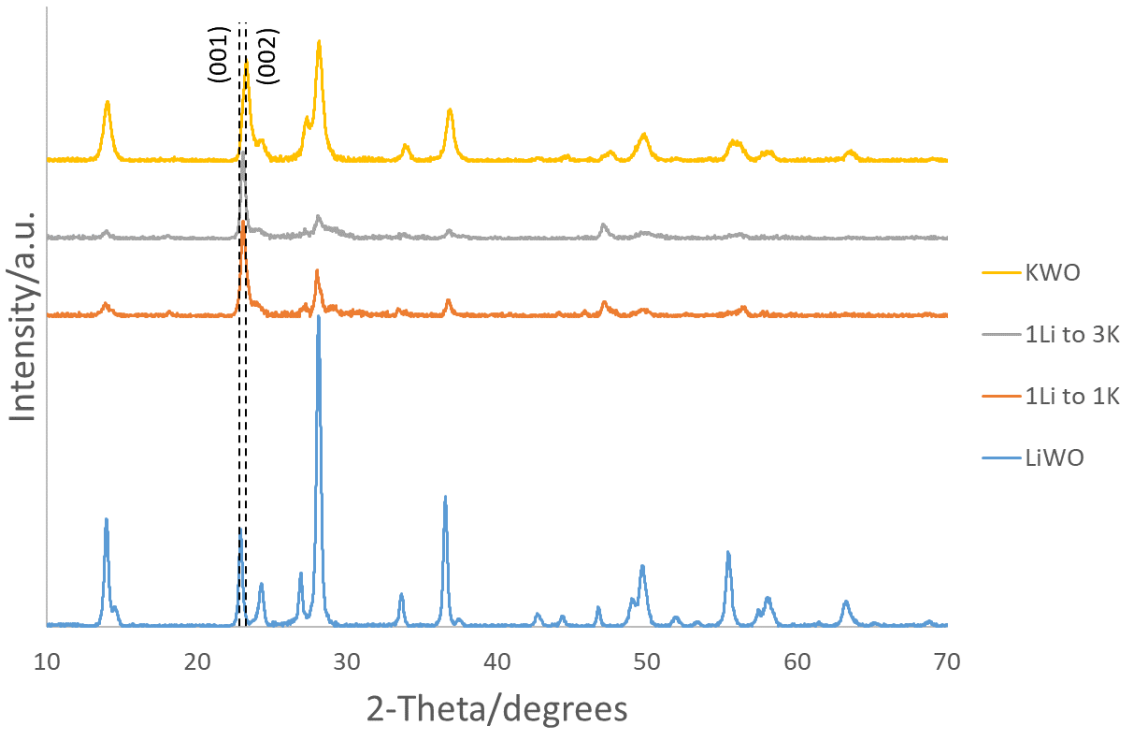

Figure 21. XRD comparison of LiWO, KWO, and hybrid samples of 3:1 and 1:1 K:Li respectively.

As discussed earlier, the primary differences between KWO and LiWO include the shift of a peak from *(001)* to a *(002)* facet, and the lower expressed *(200)* peak in KWO. When grown as a hybrid it can be seen the samples come out much less crystalline, and the strongest peak ends up in between where the *(001)* and *(002)* peaks are, see **Figure A1** for a zoom in on these peaks. This means the samples likely grew crystal facets of both. It can be concluded that the growth this way inhibits crystal growth given the weak crystallinity seen in both samples.

2.3.1.2. Scanning Electron Microscopy (SEM)

Electron microscopy was done using a JEOL JSM-7600F field-emission SEM. Samples were prepared as a powder on carbon tape. SEM imaging of KWO, NaWO, and LiWO can be seen in **Figure 22**, which shows all samples present nanorod morphology. As we look at the samples, it can be seen that they present pure nanorod structure in good agreement with the XRD

data, and little-to-no difference can be seen between LiWO, and NaWO samples in a morphological sense. However, KWO has a much thinner morphology which has been shown to relate to the *(002)* facet. This is due to most cases with inorganic salts as capping agents hydrothermally synthesized WO_3 nanorods and their variations shown here are grown along the intrinsic *c*-axis because the surface energy of the *(001)* crystal facets are higher than the *(110)* facets. [50] However, using larger ions, such a K^+, as capping agents can cause the expression of the *(002)* facet by forcing growth along the *(110)* axis.

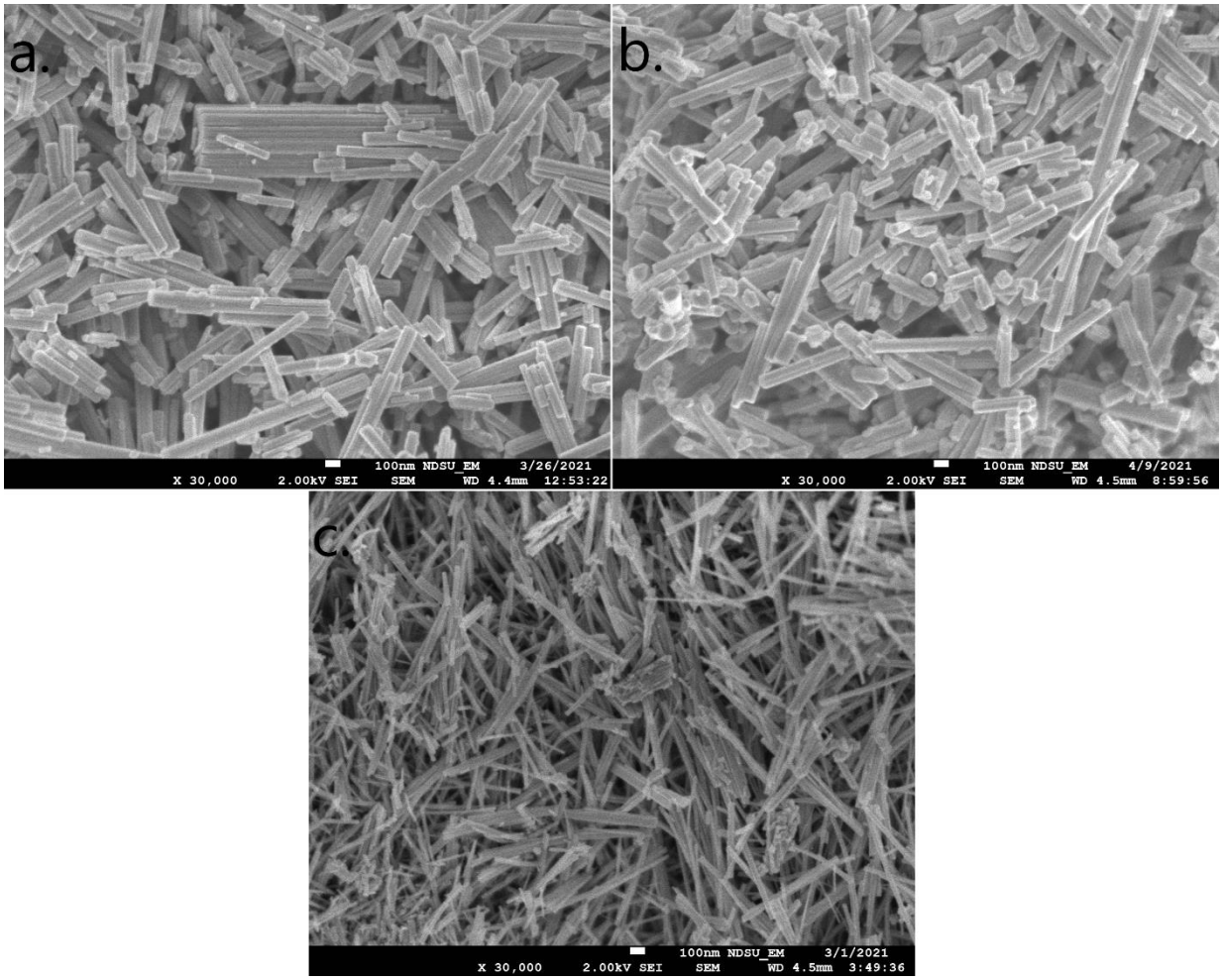

Figure 22. SEM of (a.) LiWO, (b.) NaWO, and (c.) KWO nanorods.

Continuing, samples grown with K:Li mixtures were studied using SEM in the same manner, the results can be seen in **Figure 23**. Like previously mentioned, KWO has a thinner

morphology than LiWO. Knowing this, the hybrid samples shows an expected progression of becoming thinner in morphology as K content is increased and Li content is decreased. It is likely, given the data from XRD, that the nanorods in the hybrid samples are a mixture of KWO and LiWO and not a homogenous mixture of K and Li. This means K and Li have likely grown congruently but are still discreet materials. This idea works well with the XRD data as well, as previously discussed, the K and Li samples grow on different axis due to being different capping agents. While both are present during synthesis, it would likely hinder growth in both the preferred axis leading to the low crystallinity observed.

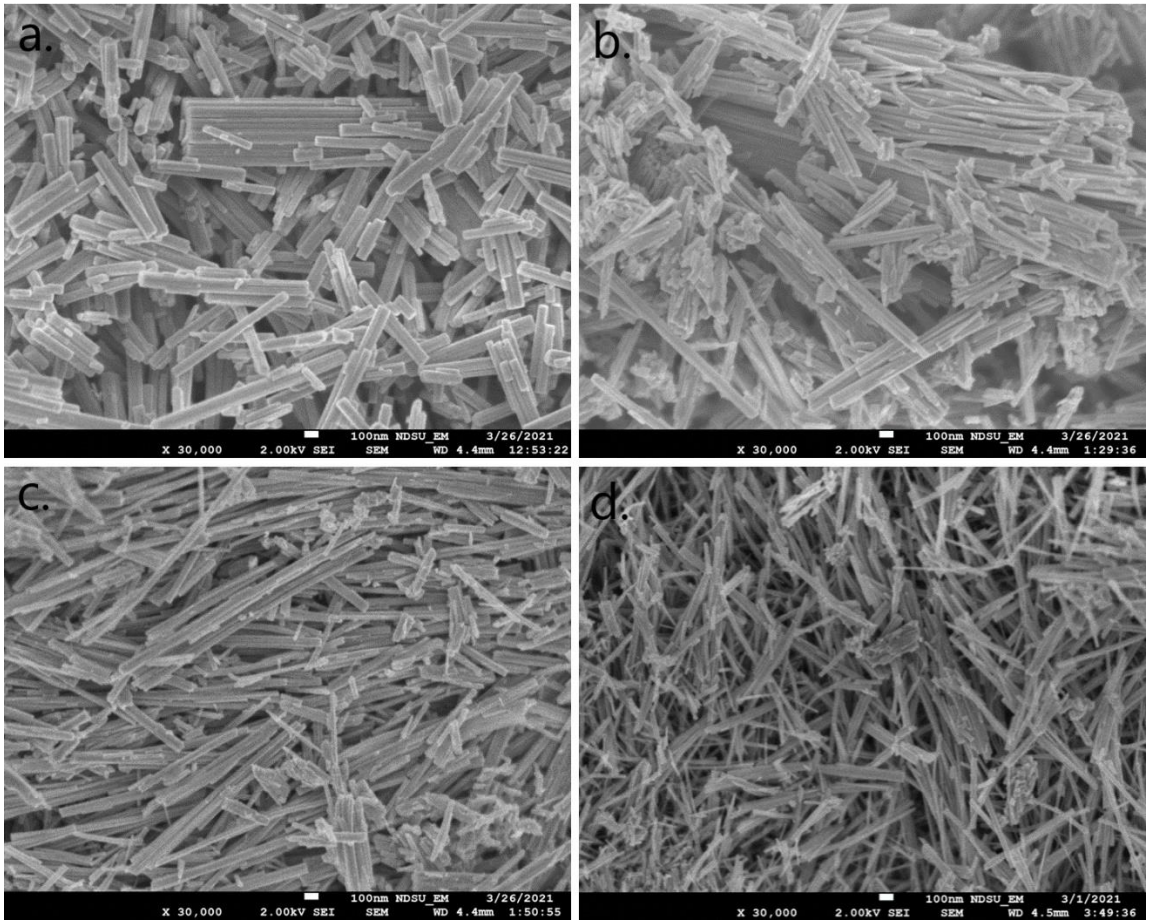

Figure 23. SEM of (a.) LiWO, (b.) 1:1 (K:Li)WO, (c.) 3:1 (K:Li)WO, and (d.) KWO.

2.3.1.3. Raman Spectroscopy

Raman spectra were obtained using an Aramis Confocal Raman Imaging System with Horiba Jobin Yvon's Raman Spectrometer from 200-1000 cm^{-1}. Results can be found in **Figure 24**. As discussed earlier, samples show peaks at ν= 642, and 688 cm^{-1} which belong to the ε-phase of WO_3 as shouldering. This shouldering can be seen only in the KWO sample indicating that neither NaWO nor LiWO present any ferroelectric ε-phase. Raman peaks located to 757 and 810 cm^{-1}, respectively, are assigned to O–W–O stretching vibration modes of hexagonal γ-WO_3 phase. It can be seen that these peaks shift to 730 and 792 cm^{-1} which is connected with the shortening of stretching vibration modes O–W–O, and corresponds to small cell parameters of KWO in good agreement with the XRD data. [68] Peaks at 911 and 962 cm^{-1}, seen on the KWO spectrum, correspond to surface oxygen. This indicates that the KWO sample has a high receptor function at room-temperature allowing for oxygen to accumulate on the surface of the material.

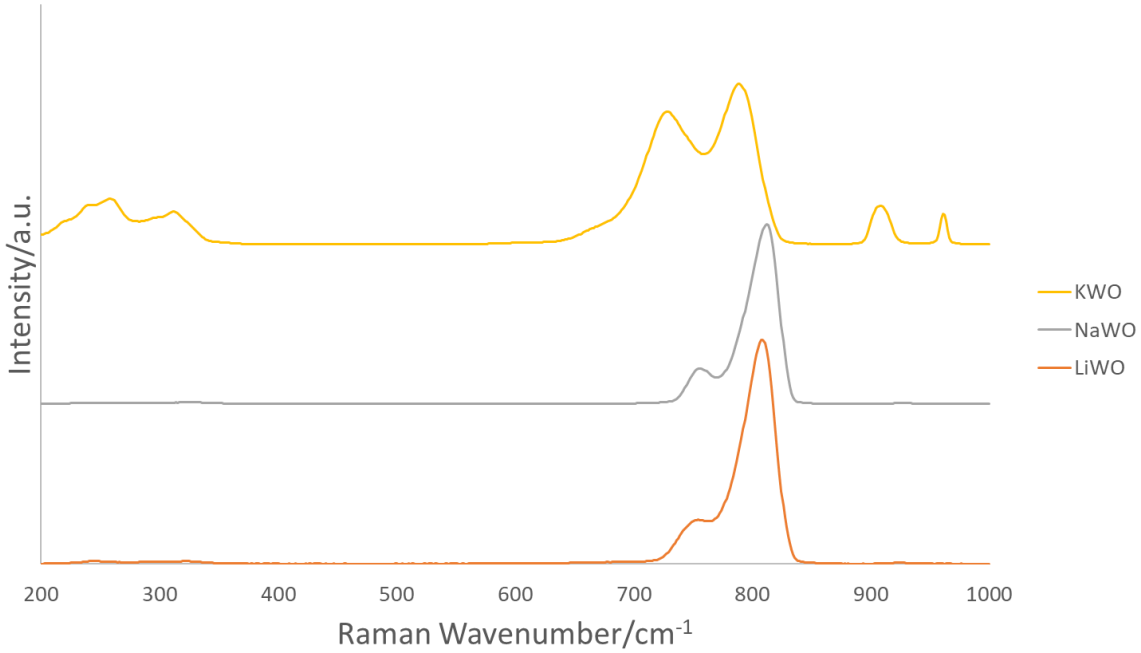

Figure 24. Raman spectra of KWO, NaWO, LiWO, and pure WO_3.

Raman spectra were also collected of hybrid (K:Li)WO samples and compared to pure LiWO and KWO with results shown in **Figure 25**. As described earlier, a shift in the O-W-O peaks indicate smaller cell parameters, and we see KWO shifts to 792 cm^{-1} from LiWO being at 810 cm^{-1}. Bothe the hybrid samples shift ever further down to 779 cm^{-1} which is in good agreement with the XRD data which present low crystallinity. Beyond this a clear pattern can be followed in the shouldering where the ε-WO_3 peaks are. As the K content increases, a larger shouldering can be observed indicating higher ferroelectric phase content.

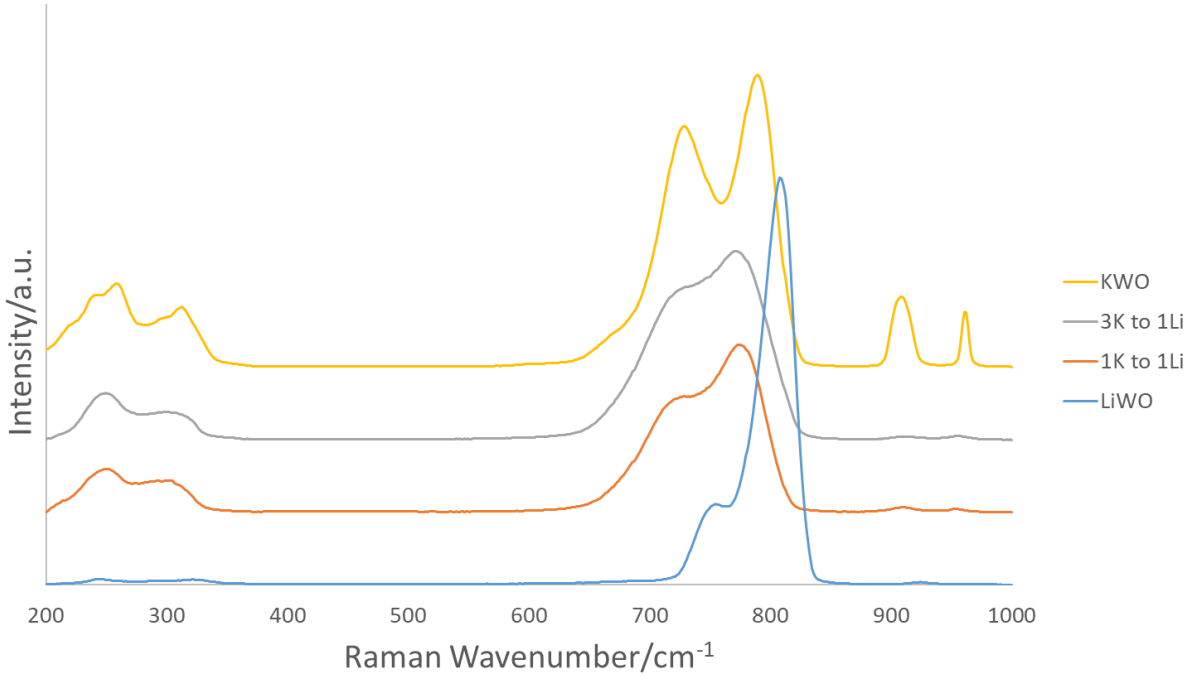

Figure 25. Raman Spectra of pure KWO and LiWO, and hybrid (K:Li)WO samples.

2.3.1.4. Acetone Sensing and Discussion

Initial sensitivity data can be seen in **Figure 26**. KWO grown hydrothermally has shown the best sensitivity to acetone. This is likely due to the good ferroelectric property which was seen in the Raman data. From there LiWO becomes less sensitive and NaWO even less so. KWO presenting good sensitivity is due to the strong ferroelectric phase it presents in combination with

the more expressed *(002)* facet seen from the XRD data. Here it is reinforced again that a combination of the *(002)* facet and the ferroelectric phase are paramount towards the detection of acetone using KWO at room-temperature. More study towards the selectivity of these materials could give us good insight of the working mechanism as well.

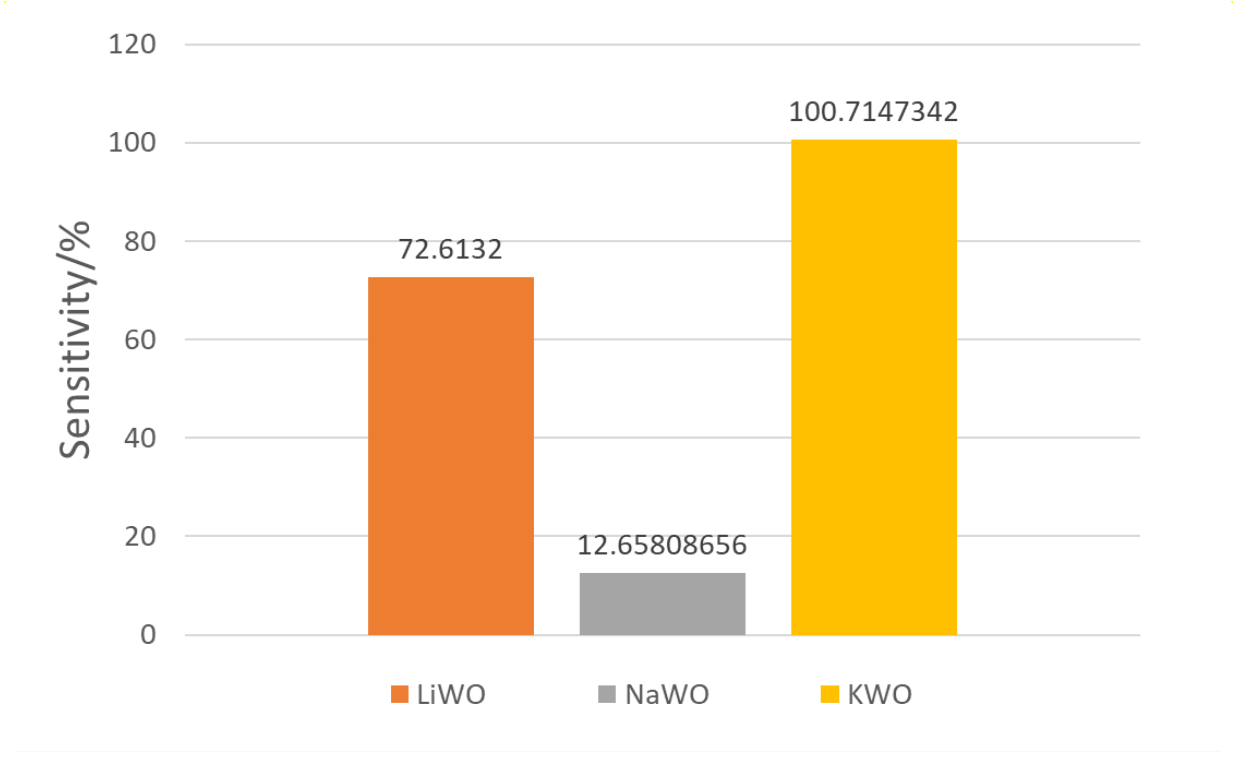

Figure 26. Sensitivity of LiWO, NaWO, and KWO.

Sensitivity data of hybrid (K:Li)WO samples can be found in **Figure 27**. It is found that both of the hybrid samples have a sensitivity higher than that of pure KWO or LiWO. This warrants further study as the Raman spectra show good ferroelectric phase, and the XRD has shown a peak that is likely a combination of the *(001)* and *(002)* facet as discussed earlier which means these results could be true. Further sensing testing should also be done to verify this.

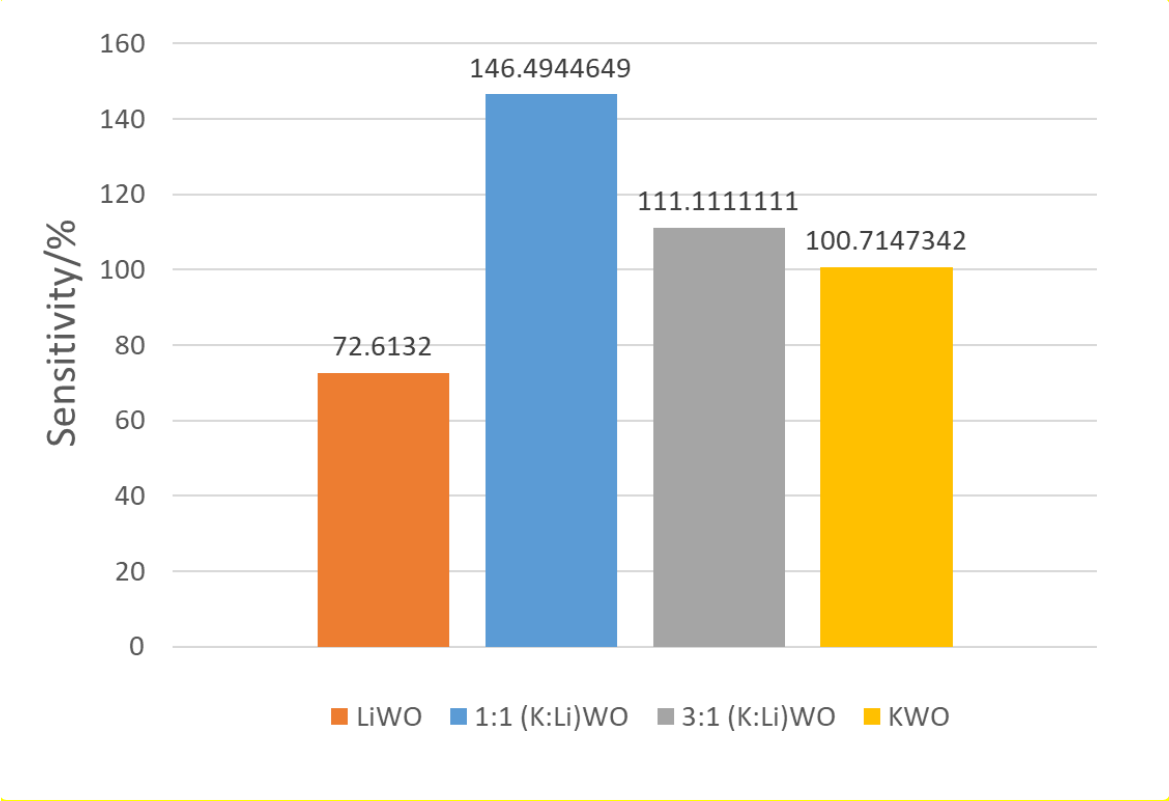

Figure 27. Sensitivity of pure KWO, LiWO, and hybrid mixtures of 1:1 and 3:1 (K:Li)WO.

2.3.2. Other Metals

Other metals have also been tested to find if non-alkali metals could be used to the same effect. Herein, it is tested to see if tungsten oxide materials can be made using our standard hydrothermal method. Samples with Cr, Cu, La, and Sn are made using sulfates of each metal being $Cr_2[SO_4]_3$, $CuSO_4$, $La_2[SO_4]_3$, and $SnSO_4$. Samples will be denoted as their respective metal followed by "WO", *e.g.,* SnWO for a sample made with Sn. All samples were synthesized using the standard hydrothermal synthesis method described earlier. After washing and collecting, samples were tested using XRD, and SEM. Samples made with La and Sn were synthesized using a similar molar equivalence and quarter the molar equivalence of standard K_2SO_4. Due to poor acetone response and no recognizable hexagonal crystal structure in the XRD data (**Figure A2** for SnWO, and **Figure A3** for LaWO), they were not studied as

thoroughly as the Cu and Cr samples. Acetone sensing was found to be best at eighth-molar equivalence for the CuWO and CrWO samples. Much more testing is needed to definitively know sensing properties, but the initial sensitivity data can be found in **Table A1**.

2.3.2.1. Copper

CuWO samples were grown with full-, half-, quarter-, and eighth-molar equivalences. The Cu source used was $CuSO_4$ and was grown using standard conditions at full-, half-, quarter-, and eighth-molar equivalence. It was then studied using XRD, SEM, Raman spectroscopy, and acetone sensitivity.

X-ray diffraction was obtained using a Bruker AXS D8 Discover and the results can be seen in **Figure 28**. It can be seen that synthesis using half-, quarter-, and eighth-molar equivalences yield a hexagonal crystal structure with some impurities. They seem to differ from KWO in the sense that it expresses the *(001)* facet over the *(002)* facet, however, which could lead to poorer sensitivity to acetone. The other samples, full-, quarter-, and eighth-molar equivalence, show proper peaks for hexagonal crystal structure, but also show a number of impurities.

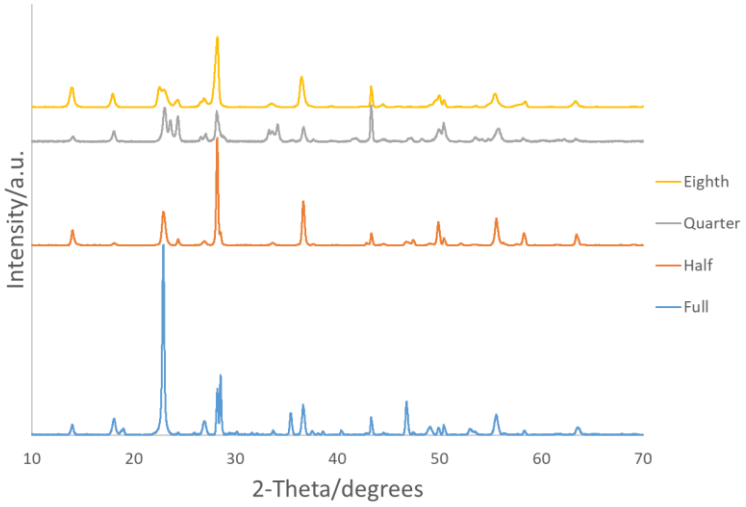

Figure 28. XRD of CuWO samples grown at full-, half-, quarter-, and eighth-molar equivalences.

SEM was done using a JEOL JSM-7600F field-emission SEM, the results can be seen in **Figure 29**. Samples grown with full- and half-molar equivalences show no nanorod structure and present more platelet structures, which are likely impurities. Quarter- and eighth-molar equivalences present more nanorod structure, indicating that the reaction has created tungsten oxide nanorods as intended.

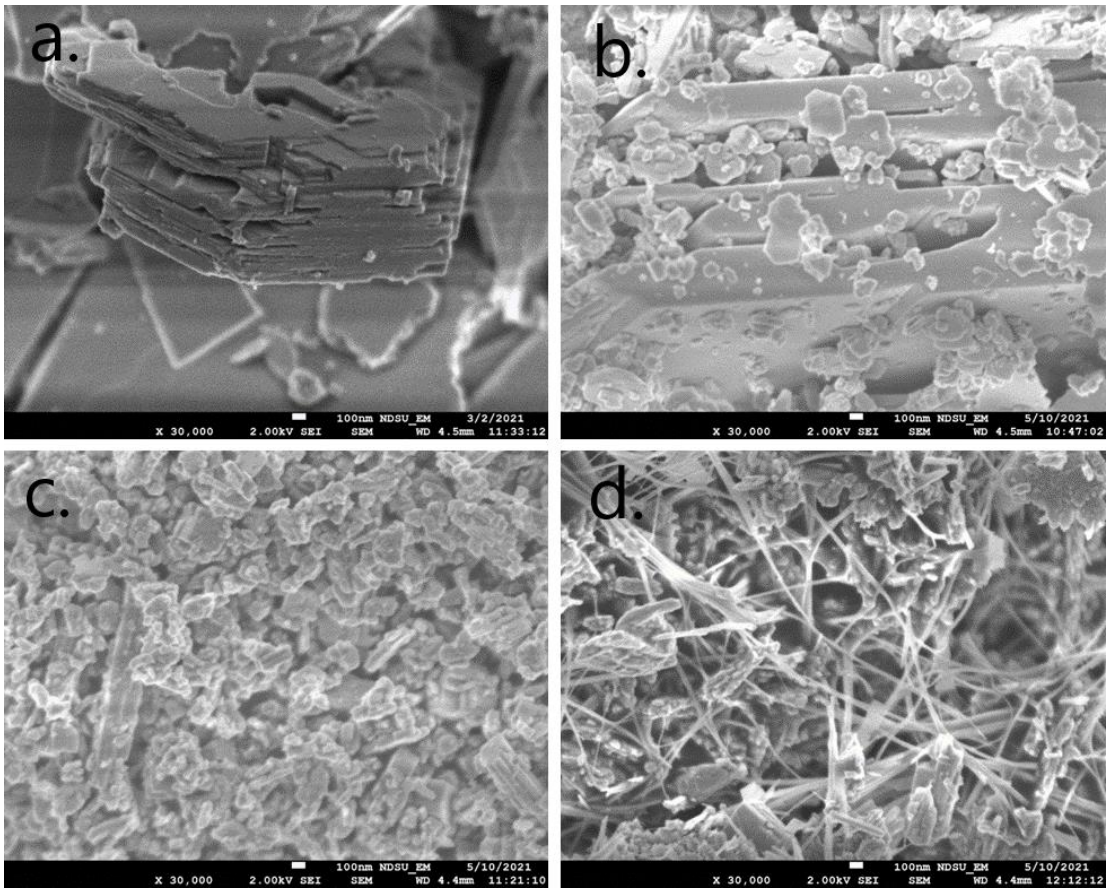

Figure 29. SEM of CuWO samples grown at (a.) full-, (b.) half-, (c.) quarter-, and (d.) eighth-molar equivalences.

2.3.2.2. Chromium

CrWO samples were grown with full-, half-, quarter-, and eighth-molar equivalences. The Cr source used was $Cr_2[SO_4]_3$ and was grown using standard conditions at full-, half-, quarter-, and eighth-molar equivalence. It was then studied using XRD, SEM, Raman spectroscopy, and acetone sensitivity.

X-ray diffraction was obtained using a Bruker AXS D8 Discover and the results can be seen in **Figure 30**. Little crystallinity can be seen in samples grown with full- and eighth-molar equivalences indicating incomplete growth of samples. This is likely due to growth of tungsten oxides with chromium require a narrow range of chromium content. [49] The sample at half-molar equivalence shows some hexagonal-WO crystal structure appearing with some impurity. The sample grown at quarter-molar equivalence shows good hexagonal crystal structure which is promising for any acetone sensitivity testing.

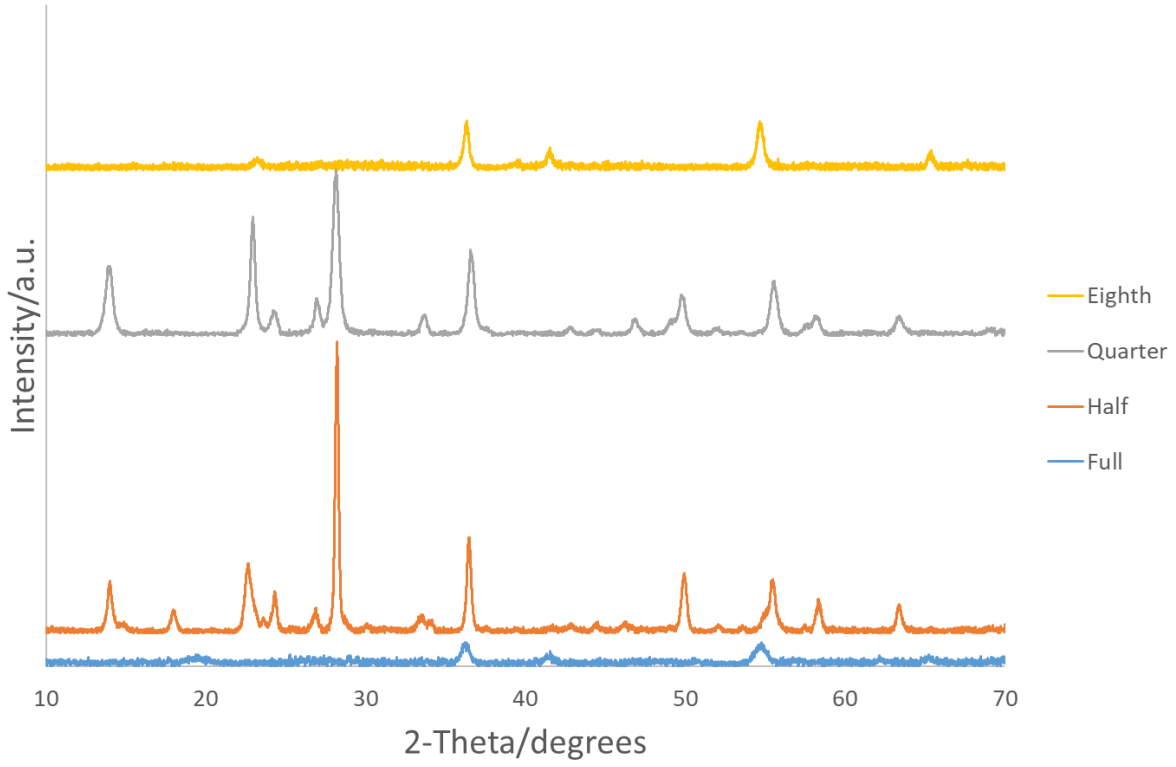

Figure 30. XRD of CrWO samples grown at full-, half-, quarter-, and eighth-molar equivalences.

SEM was done using a JEOL JSM-7600F field-emission SEM, the results can be seen in **Figure 31**. Little can be seen, besides amorphous globules, in the samples grown with quarter- and eighth-molar equivalence. This is likely due to the washing process needing to be more vigorous for this particular material as the starting Cr source contains much more sulfate than

other samples. That being said XRD data shows good hexagonal crystal structure in the quarter-molar equivalence sample indicating that there is likely still nanorod structure unseen. A few nanorod structures can be seen in samples grown at full- and half-molar equivalences, which agrees with the XRD data as well. Very few nanorods can be seen in the full-molar equivalence sample, but they become much more prominent in the half-molar equivalence sample. Overall, more SEM study should be done to get a better understanding of the morphology of all samples, in particular the half molar equivalence sample.

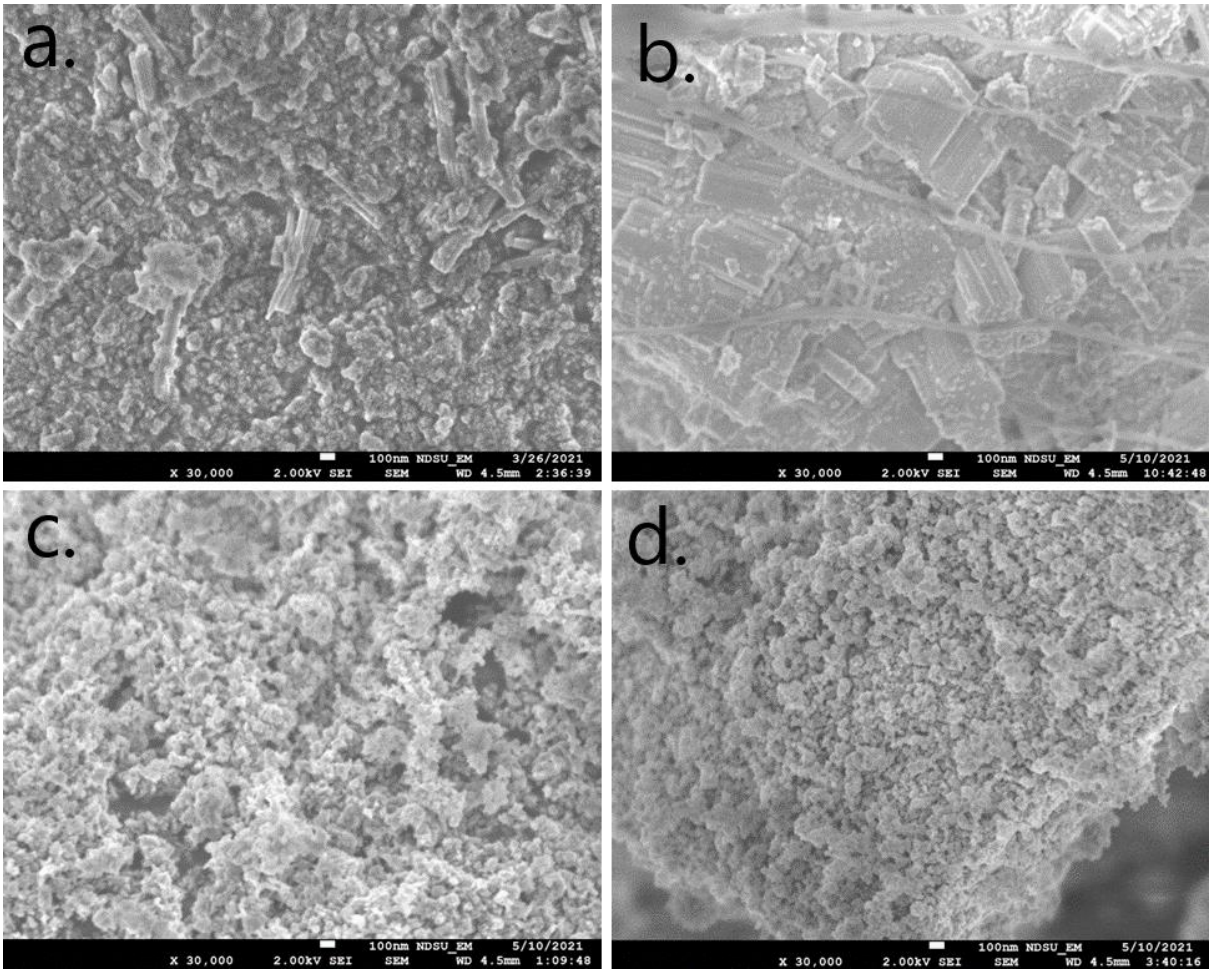

Figure 31. SEM of CrWO samples grown at (a.) full-, (b.) half-, (c.) quarter-, and (d.) eighth-molar equivalences.

2.4. Concluding Remarks and Future Work

The viability of tungsten oxide nanorods grown via the hydrothermal method for application as a breath acetone sensor was studied here. The basics of the chemiresistive method were explained and applied to the development of multiple samples. First, KWO was studied for proper growth temperature, which was found to be 225 ^{o}C, to better express its crystallinity and ferroelectric phase. Then varying levels of potassium content along with synthesis using surfactant additives was studied to tune the materials crystal facets and increase the ferroelectric property. Continuing, metals beyond K were studied using the same hydrothermal growing method. Initially, other alkali metals Li and Na were studied and compared to the original KWO. It was found that KWO had the best sensitivity to acetone, and this was likely due to it possessing the ferroelectric ε-phase. On the other hand both LiWO and NaWO samples showed poorer performance than that of KWO. More study into the selectivity and longevity of these materials should also be done to better characterize their sensing properties. Hybrid metals of (K:Li)WO were also synthesized at 1:1 and 3:1 ratios. Both samples presented ε-WO_3 correlating to good ferroelectricity and had very expressed *(002)* peaks in the XRD. They ended up having higher sensitivity than KWO and it is believed this is due to discreet KWO in the mixed samples.

Other Metals including La, Sn, Cu, and Cr were also tested in place of K. Cu and Cr samples show good morphology and a crystal structure which resembles KWO's. They merit more study for their acetone sensitivity. Initial sensing trail data for CuWO and CrWO can be found in **Table A1**.

3. Ti_3C_2 MXENE NANOSHEETS[2]

3.1. Introduction

Research of Two-Dimensional (2D) materials has been a popular topic for over a decade now. Starting from the discovery of graphene, 2D nanomaterials are of great importance in the scientific community due to their extraordinary physical and chemical properties. Incorporating 2D nanomaterials into conventional devices has tremendously improved their performance, *e.g.*, rechargeable lithium-ion batteries [69, 70], fuel production [69-73], photodetectors [74], biosensors [75], photothermal therapies [76-78], and more [74, 78]. These are all examples of areas that have greatly benefited from the incorporation of 2D nanomaterials. Among 2D layered nanomaterials, MoS_2, phosphorene, graphene, and their derivatives are the most widely studied and have been successfully applied to numerous engineering applications. [78-81] Out of these materials studied, graphene is by far the oldest and most studied. However, these materials can be tricky to work with; graphene's low surface energy is a bottleneck on cost-effective solution processing. [82] The novel new 2D MXene nanosheet on the other hand, is formed with surface functionalization that allows for dispersion into colloidal solutions readily with water. [83] Beyond this, MXenes have a variety of morphologies and elemental makeups allowing for a highly tunable material which merits research into the over 30 versions that have been classified experimentally to date. [84]

The term MXenes refers to the 2D layered nanomaterials containing transition metal carbides, nitrides or carbonitrides. [85] Unlike other 2D layered nanostructures, e.g. graphene

[2] The material in this chapter was co-authored by Michael Johnson and Danling Wang. Michael had primary responsibility for developing and carrying out material synthesis methods, as well as collection and analysis of XRD and SEM data. Michael was the primary developer of the conclusions pertaining to MXene material that are advanced here. Michael also drafted and revised all versions of this chapter. Danling served as proofreader and checked the data and conclusions conducted by Michael.

comes from graphite and phosphorene is produced from black phosphorus, MXenes do not have a basic elemental 3D precursor. Instead, MXene layered flakes are produced via etching and exfoliation of the A layer in ceramic MAX materials, such as the removal of the Al layer from Ti_3AlC_2, which is the most common MAX phase studied for this use. After removal of the A layer from the MAX phase, intercalation agents, such as DMSO or Li^+ ions, are typically utilized to delaminate the structure into few-layer or even single-layer nanosheets.

To better understand MXene's structures, the precursor MAX phase origins will need to be discussed. MAX and $M_{n+1}AX_n$ (n = 1, 2, or 3) phases are layered transition metal carbides and nitrides classified into three types that denote the molar amount of each basic element, 211, 312, and 413 dependent on the value of n, all with hexagonal crystal structures. [86-88] M represents an early transition metal, such as Ti, V, Nb, or Ta; A represents elements from group 13 or 14, usually Al or Si; and X refers to C, N, or blends of the two. To further explain, the MAX crystal structure, 211, would have periodic stacking of M-X-M-A along its cross section. So, a Ti_2AlC MAX phase has a periodic stacking of Ti-C-Ti-Al. The Ti bilayers are two layers of closely packed atoms, while the C monolayer consists of C atoms occupying octahedral sites between the two Ti layers, and finally the Al monolayer splits periodic units of the Ti-C-Ti trilayers.

There are three common types of MAX phase classification; 211, 312, and 413, are the number of M layers between each A layer, being 2, 3, and 4 respectively. Moreover, the number of X layers will always be one less than the number of M layers. Currently, over 150 MAX phases have been studied [84], most of which exist as the 211 phase, followed by the 312 phase and finally the 413 phase. Even higher order MAX phases exist but they are few and require special means to synthesize. The discovery of more MAX phases is ongoing, and directly affects the types of MXenes that can be made to date. The 413 phase members as well as binary metal

alloys ($M'_xM''_y$) that replace the single M layer are of particular interest currently. [89, 90] The M layers are comprised of one element from Ti, V, Cr, Zr, Nb, Mo, Hf, and Ta; A layers can consist of an element among Al, Si, P, S, Ga, Ge, As, Cd, In, Sn, Tl, and Pb; and the X layers are comprised of C, N or a combination of both. The wide variety of MAX phases that can be made allows for numerous MXene materials to be crafted and studied. This all leads to exciting new areas of research into this new 2D nanomaterial for its properties and uses.

In the beginning, the methods of producing MXenes were limited, with the only method of synthesis involving the use of hydrofluoric (HF) acid to etch the aforementioned MAX phases. The first MXene isolated, Ti_3C_2, was obtained by soaking Ti_3AlC_2 MAX powders in HF acid. Since their discovery, MXenes became a hot topic in research with varying compositions being synthesized using selective etching. [85, 91-95] The interest in MXenes has begun to rapidly grow [96-106], and researchers in theoretical chemistry predict a large quantity of new MXenes. [89, 90, 107-110]

In most MAX phase materials, the M-X bond is stronger and more stable than the A layers, which are relatively weaker than the M-X bonds. Therefore, selective etching reactions to remove A-layers is the preferred strategy, using HF acid as stated earlier. Early work revealed MAX phases are inert in the presence of other acids (HCl, H_2SO_4, and HNO_3), NaOH solutions, and common salts (NaCl and Na_2SO_4). However, in 2014, an alternative LiF salt precursor method was developed, which was able to bring MXenes to a new era of their research. [111] This new method created a moldable “clay” which allowed for easy use in numerous new applications. At the nanoscale, this method also was able to fully delaminate nanosheets from the regular accordion-like structure without the need for addition of other intercalation methods or

sonication. Due to this method requiring no harsh chemicals or sonication, it was named the MILD method.

MXene nanosheets often contain surface functional groups, denoted as a T_x in the general chemical formula, of O, F, and OH. This functionalization leads to the formation of semiconducting properties displayed by MXenes. That is, the MXene $Ti_3C_2(OH)_2$ will present semiconducting properties while a pristine MXene with no surface functionalization like Ti_3C_2 will have metallic properties.

With all the possible MXene chemical properties discussed so far, there is an immense range of possible MXene materials. Considering all the possible differences that can exist between MXenes, we can surmise that these materials can be highly tunable for many applications. Herein, the most popular MXene studied to date, Ti_3C_2, and its MAX precursor, Ti_3AlC_2, are studied under different synthesis conditions that pertain to making usable 2-D nanomaterials with varying properties.

3.2. Synthesis of Ti_3C_2 MXene

3.2.1. MAX Synthesis

To be able to truly control MXene parameters the MAX phase must be first studied. As the precursor to the final product, it will dictate the order of the synthesized MXene product, *i.e.* 211, 312, 413 discussed earlier. Herein, proper sintering conditions to create Ti_3AlC_2 are found by controlling temperature, time, and molar-ratio of precursor materials.

The synthesis method starts with ball-milling TiC, Al, and Ti powders at a 2:1.2:1 ratio respectively together in toluene for 5 hours. Extra Al is used as loses are found to happen later in the process. [92] These powders are collected via centrifuge then dried in a drying oven at 60 ^oC. Once dried the powder is collected and put into a high-purity alumina crucible for sintering. The

sintering process has been reported to yield the purest Ti_3AlC_2 MAX product at 1350 ^oC in an Ar atmosphere. [83] To produce the best quality MAX phase, the sinter time was studied by synthesizing material at 1350 ^oC for 0.5, 1, 2, 3, and 4 hours under Ar gas flow. The resulting product yielded a dark grey solid which were then studied using XRD for purity; the results are seen in **Figure 32**. The results clearly indicate that as sinter time is increased the crystallinity and purity of the product increase, with peaks for TiC impurity decreasing and Ti_3AlC_2 peaks increasing. Using this information all MAX phase is prepared as described above and sintered for 4 hours for MXene samples made.

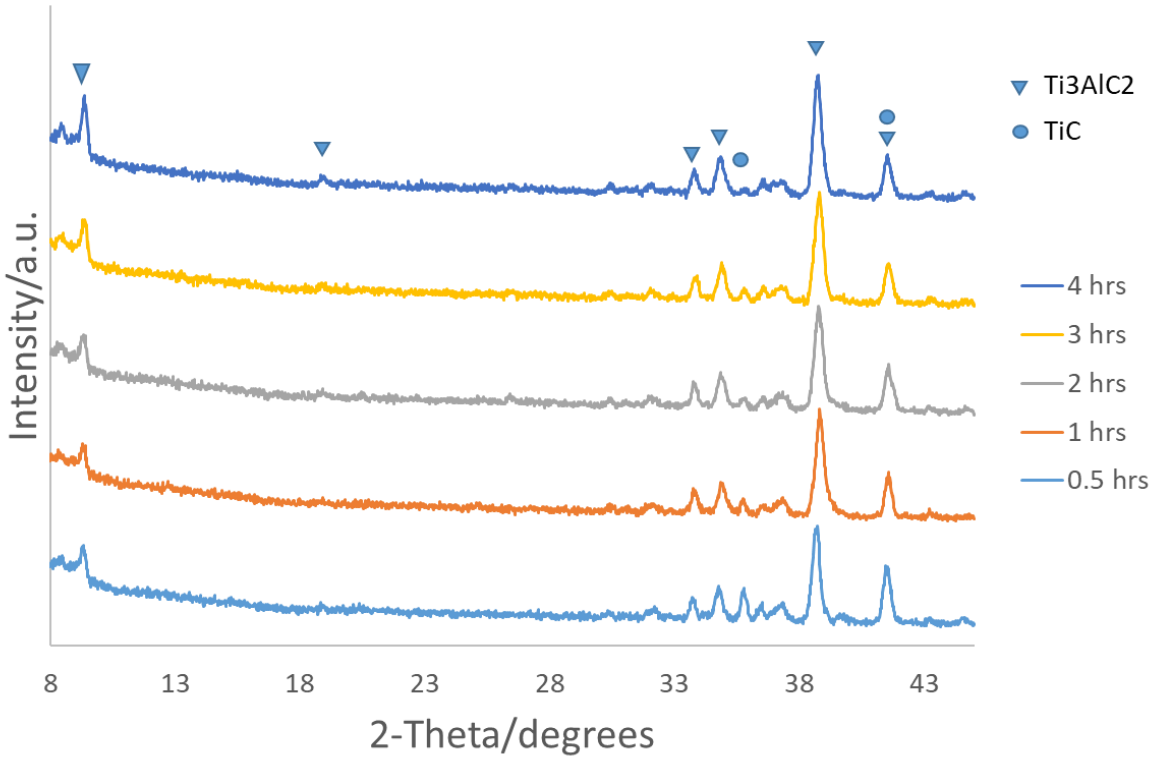

Figure 32. XRD Ti_3AlC_2 MAX phases sintered at 1350 ^oC for 0.5, 1, 2, 3, and 4 hours.

3.2.2. Hydrofluoric Acid

The top-down approach initially created thick multilayer flakes of MXene via selective etching MAX phases. The selective etching of MAX phases would extract the A layer to form

MXenes. Early examples of this method used aqueous concentrated hydrofluoric acid to remove the weakly bound Al layer from the Ti_3AlC_2 phase, see reaction (3.1), at room temperature. [83] After removal of the Al layers, the pristine MXenes would then react with excess HF, and H_2O to make $Ti_3C_2F_2$ and $Ti_3C_2(OH)_2$, Reactions (3.2) and (3.3).

$$Ti_3AlC_2(s) + 3HF(aq) = Ti_3C_2(s) + AlF_3(aq) + 3/2H_2(g) \quad (3.1)$$

$$Ti_3C_2(s) + 2HF(aq) = Ti_3C_2F_2(s) + H_2(g) \quad (3.2)$$

$$Ti_3C_2(s) + 2H_2O(aq) = Ti_3C_2(OH)_2(s) + H_2(g) \quad (3.3)$$

The different surface terminations with hydroxyl and fluorine groups occur due to pristine 2D-layered Ti_3C_2 monosheets having two exposed Ti atoms in a unit cell. These Ti atoms require thermodynamic dangling bond passivation, and because the reaction environment is rich with fluorine anions, and hydroxyl groups they are the most common reported surface ligands.

MXenes prepared in this fashion consist of multilayer flakes in an accordion like structure held together by weak interlayer interactions. Ultra-sonication of this product will exfoliate these sheets leading to nanosheets with a thickness of 11 ± 3 nm, which corresponds to ten layers of $Ti_3C_2(OH)_2$.

XRD and SEM are two very common techniques to study the etching process from MAX to MXene. **Figure 33** shows to XRD of as-synthesized MAX phase and the resulting MXene from a 24-hour etching done at room-temperature with 50% wt. HF solution. It can be seen that the most prominent MAX phase peaks occur at 9.5°, 26.6°, and 38.9° while TiC impurities can be seen with peaks at 36.0° and 41.7°. After etching, the peaks corresponding to the MAX phase have disappeared and left wider peaks at 9.0°, and 18.2°. These wider peaks are characteristic to MXenes and indicate good etching. The larger width of the peak is due to the final product having vacancies where Al atoms once resided now having more variance in distance between

nanosheets, which are now held together by electrostatic forces into stacks. [112] This can be seen in **Figure 34** which shows the resulting "accordion"-like morphology a stack of etched MXenes can present.

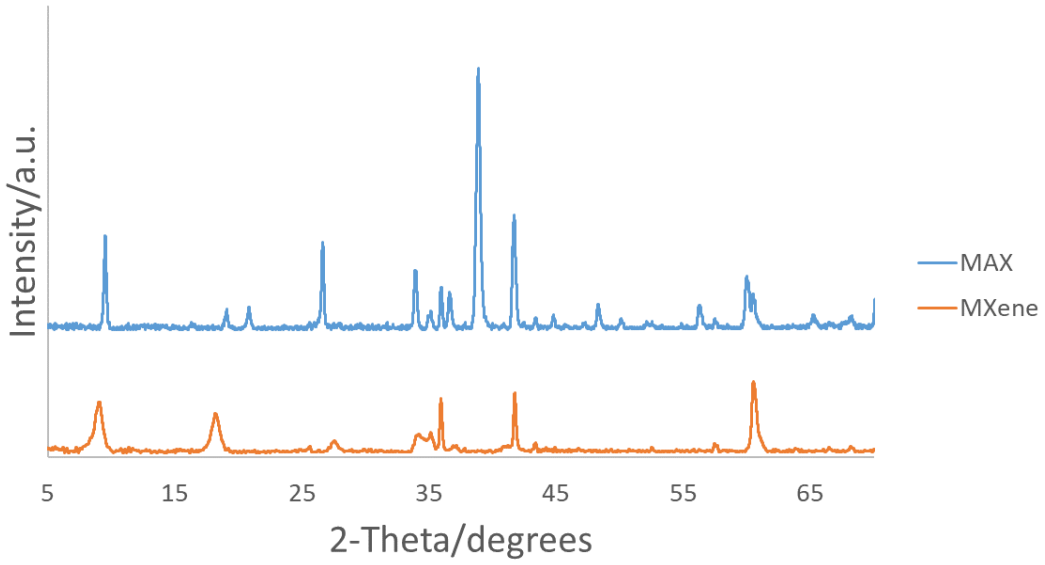

Figure 33. XRD of Ti_3AlC_2 MAX phase and post-etching Ti_3C_2 MXene.

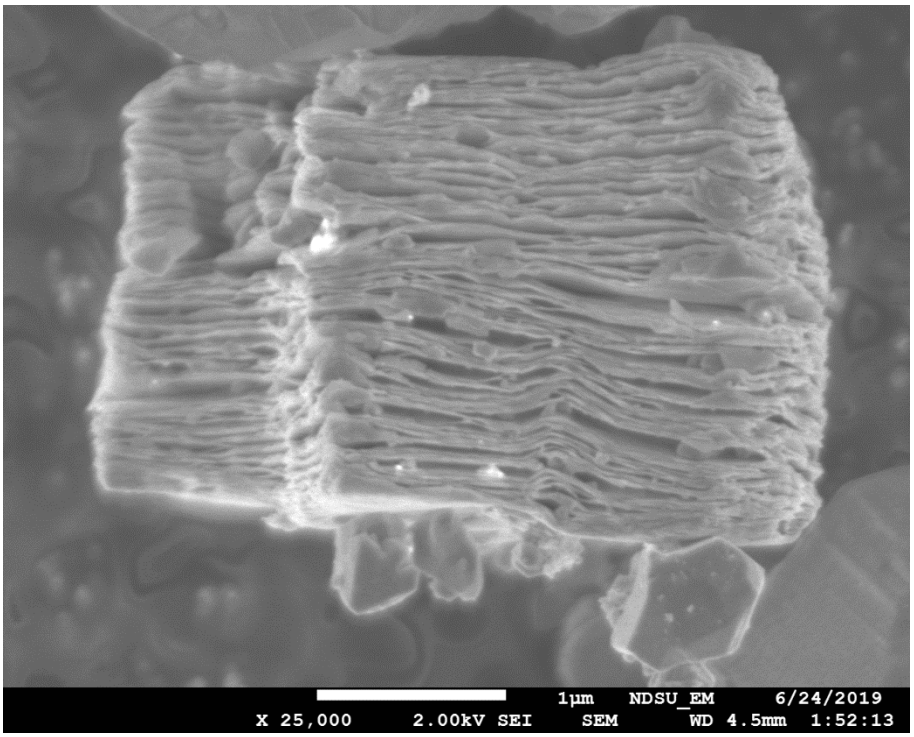

Figure 34. SEM of resulting Ti_3C_2 made by etching Ti_3AlC_2 MAX phase with HF acid.

3.2.3. MILD Method

Mixed solution etchant media has also been developed. By utilizing an aqueous mixture of LiF/HCl, which is milder and less hazardous than hydrofluoric acid, an in-situ production of hydrofluoric acid for selective etching was developed [112-117]. The HF species is produced, as seen in reaction (3.4):

$$LiF(aq) + HCl(aq) = HF(aq) + LiCl(aq) \quad (3.4)$$

Immersing a Ti_3AlC_2 powder MAX phase in this solution has similar effect to immersing the powder in hydrofluoric acid. The concentration using this method of etching is still very controllable which has made this etching method very popular among many research groups. After reaction, samples are rinsed with water to remove side products, such as AlF_3, for a pure final product. The $Ti_3C_2T_x$ MXenes are produced after drying. What is most interesting about this method is the final MXene product has clay-like features which is highly flexible and shapeable. Interestingly, the relative ratio of LiF in the reaction solution and the inclusion or non-inclusion of sonication treatment can influence the lateral sizes of the final MXene. [118] Due to the chemicals being relatively safer to handle and how they are less harsh on the final material, this method of etching has been labeled MILD.

Here, MILD Ti_3C_2 MXene samples are synthesized by adding 0.5 g of Ti_3AlC_2 MAX to a solution prepared by mixing 0.8 g of lithium fluoride (LiF) into 10 mL of 9M hydrochloric acid (HCl).

Again, XRD can be employed to study the etching process from MAX to MXene. **Figure 35** shows the XRD of as-synthesized MAX phase and resulting MXene from utilizing a MILD etching method. In congruence with standard HF etching, MAX peaks can be seen to disappear after etching leaving characteristic MXene peaks at 7.1°, and 14.2°. Compared to the standard HF etching method, it can be seen that the characteristic MXene peaks have shifted downward. This

is due to Li^+ ions intercalating between the nanosheets creating a larger average gap between sheets. This intercalation also helps weaken the electrostatic attractions which hold the accordion-like structure together. This weakening allows for delamination and creation of single-to-few layer MXene nanosheets by simply washing and agitating the product in D.I. water. A single layer sheet created this way can be seen in **Figure 36**.

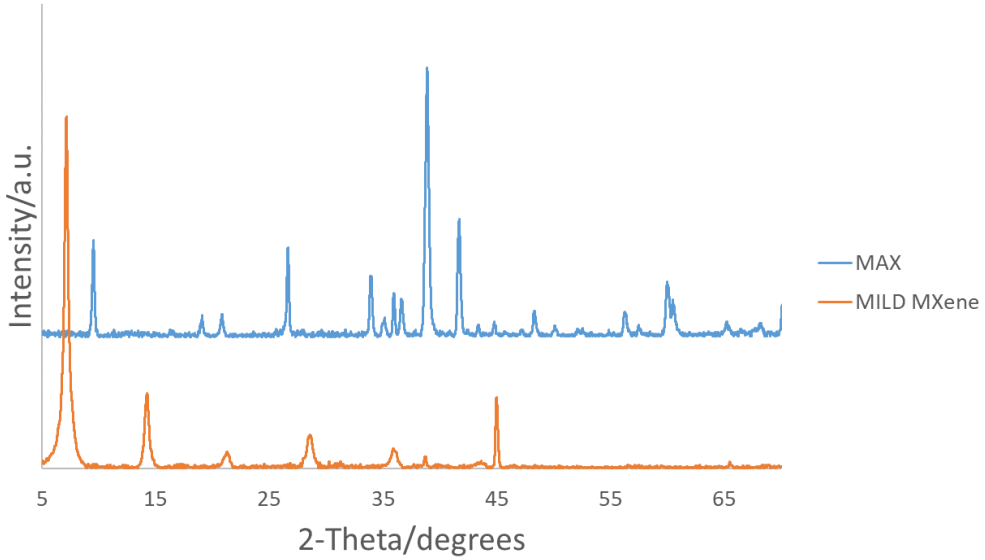

Figure 35. XRD of as-synthesized MAX phase and resulting MXene from utilizing a MILD etching method.

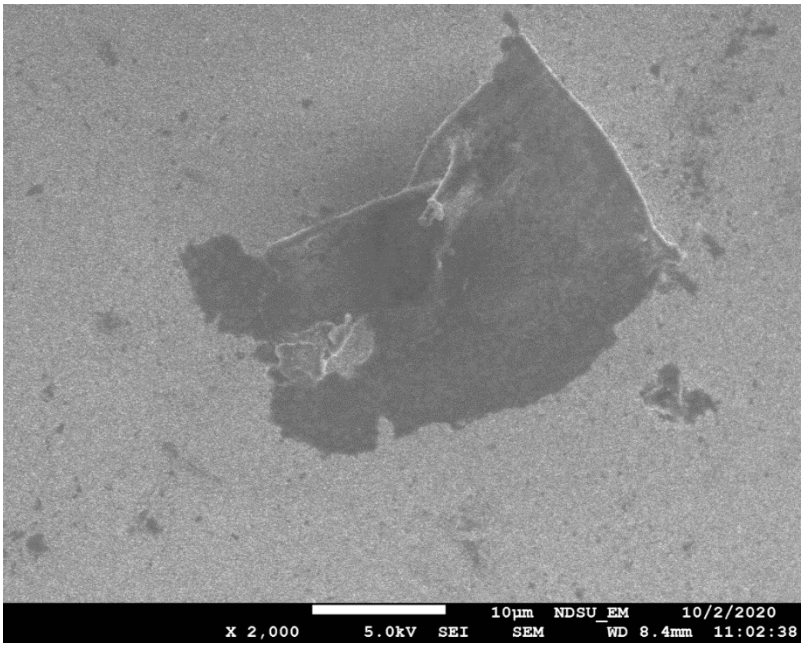

Figure 36. SEM of a single-layer MXene nanosheet on ITO substrate made via the MILD etching method and subsequent washing.

3.2.4. Elevated Temperature Etching

In recent years, many studies have been done to try and optimize the synthesis process of two-dimensional $Ti_3C_2T_x$ nanostructures for semiconductor material applications. It has been predicted that Ti_3C_2 MXenes have direct-bandgap semiconductor properties. [119] However, experimental synthesis of MXenes still pose challenges and further exploring synthesis procedures for chemical and structural diversity will allow for a wider variety of applications.

In this study, $Ti_3C_2T_x$ was prepared by etching with hydrofluoric acid. Many variables can be controlled during the etching step including temperature, time, and HF concentration. To further explore synthesis conditions of $Ti_3C_2T_x$, we synthesized $Ti_3C_2T_x$ at high temperatures, and then studied using field-emission scanning electron microscopy and x-ray diffraction.

MAX phase was created using the standard method described earlier. 0.5 g of MAX phase was etched using HF acid in a 25 ml Teflon lined autoclave at temperatures of 100, 120, and 150 ^{o}C for five hours in a Thermolyne furnace. Varying HF concentrations of 5, 10, and 15

%wt. were studied at all temperatures. Samples were let cool to room-temperature naturally then sonicated for one hour using a sonicating bath and collected via centrifuge. All sample were then dried overnight at 65 ^{o}C in a drying oven.

MILD samples are also being studied under hot-etching conditions. Like the samples etched with HF acid, MILD samples were made by etching 0.5 g MAX at 100, 120, and 150 ^{o}C. Samples were synthesized by adding 0.5 g MAX phase into a solution of 1.6 g LiF and 20 mL of 9M HCl which was sealed in a 25 mL autoclave and then heated at the respective temperatures for 5 hours. Samples were let cool to room-temperature naturally and then collected via a vigorous washing and centrifuge cycle. Initial XRD data was collected and is presented further on.

3.2.4.1. X-ray Diffraction

XRD was used to study the $Ti_3C_2T_x$ MXene's crystal structure and purity. The relative intensities of the characteristic MXene peaks (8.9^{o}) and can be used to find sample purity with a higher peak showing higher crystallinity. [119] All samples present peaks from a TiC impurity (36^{o} and 42^{o}) which originate from the as-synthesized MAX phase.

Figure 37 presents the XRD of all samples etched at 100 ^{o}C, and it can be seen that increasing the HF concentration from 5 to 10 %wt. yields taller characteristic MXene peaks. This indicates a more complete etching process has occurred. However, we see no significant change in purity when increasing the HF concentration from 10 to 15 %wt.

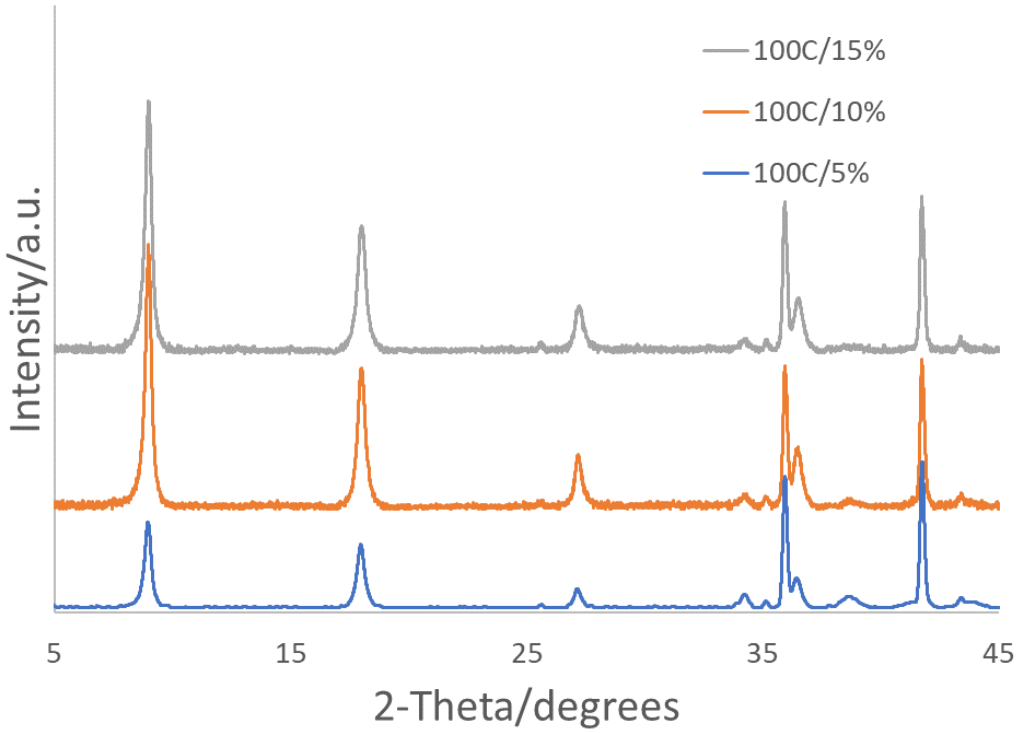

Figure 37. XRD of MXenes etched at 100 ºC for 5 hours at concentrations of 5, 10, and 15 %wt. HF.

Figure 38 shows the XRD data of all samples etched at 120 ºC. The purity of all samples etched at this temperature show little variance with only a small dip in purity when the sample is etched at 15 %wt. indicating the MXene phase may begin to decompose while etching under these conditions which agrees well with the FESEM data. We see the same effect when looking at the XRD of samples etched at 150 ºC in **Figure 39**. The XRD presents the lowest purity when compared to samples etched at lower temperature, and when etched at the highest concentration, 15 %wt., yields no MXene material and only TiC peaks. This indicates that the sample has totally decomposed into TiC under these etching conditions.

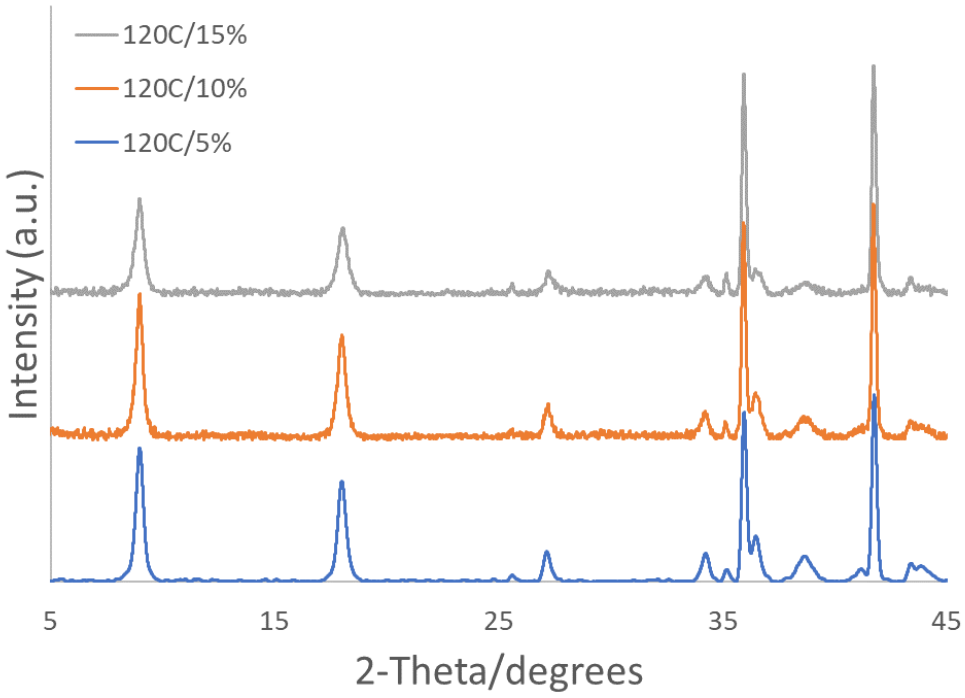

Figure 38. XRD of MXenes etched at 120 ^{o}C for 5 hours at concentrations of 5, 10, and 15 %wt. HF.

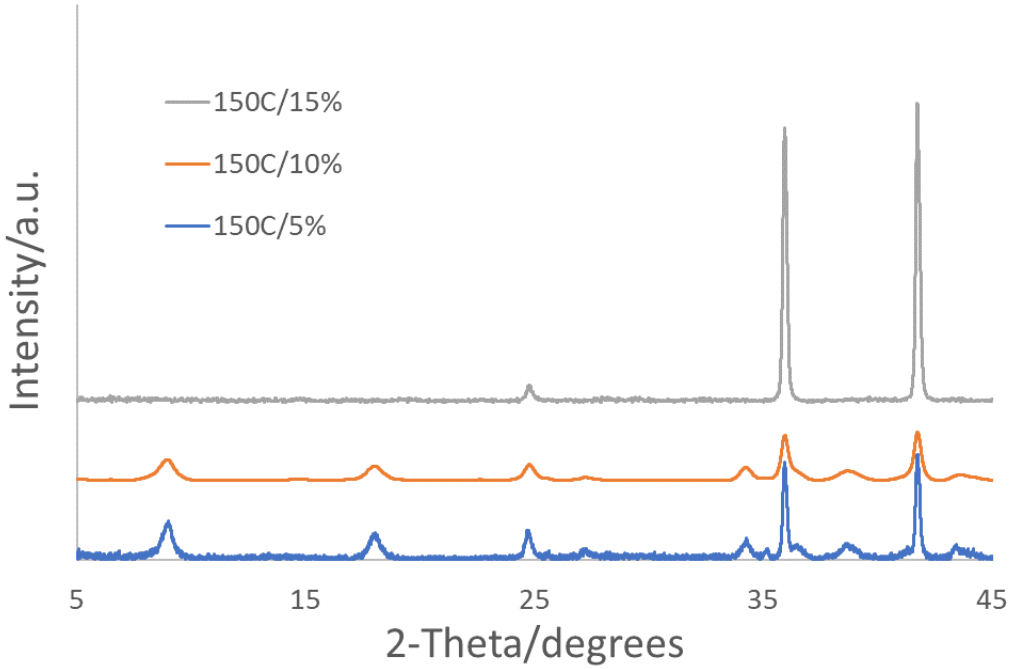

Figure 39. XRD of MXenes etched at 150 ^{o}C for 5 hours at concentrations of 5, 10, and 15 %wt. HF.

MILD Ti_3C_2 synthesized via hot-etching was also studied using XRD. The results can be seen in **Figure 40**. Characteristic MXene peaks are present indicating a successful etching process in all samples. However, it can be seen that the peak at 21.6° begins to become much more prevalent, which corresponds to Li_3AlF_6 (PDF 00-052-1151). Given this, it can be assumed that the higher temperature etching process will start to favor this reaction at higher temperatures and decrease etching achieved. Overall, more study is required to understand the full effect hot-etching has on MXenes made using the MILD method.

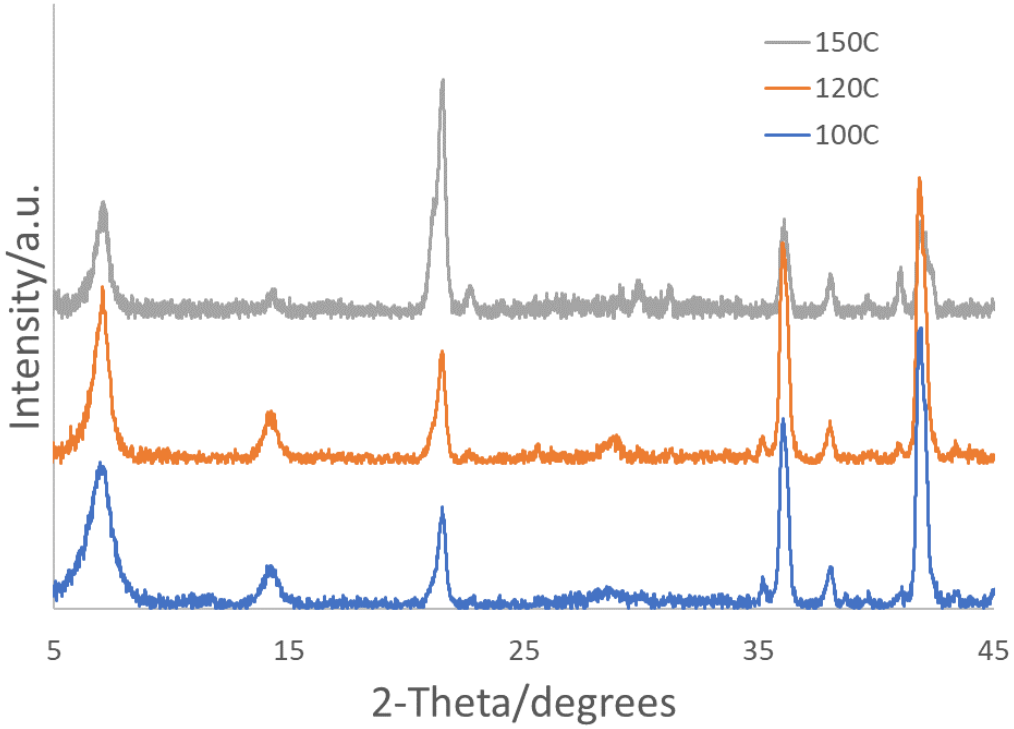

Figure 40. Ti_3C_2 MXenes ethed using the MILD method at 100, 120, and 150 °C.

3.2.4.2. Scanning Electron Microscopy

FESEM was used to study the morphology of all HF etched samples made. **Figure 41** shows the SEM images of multiple Ti_3C_2 samples that were etched using temperatures at 100, 120, and 150 °C and HF concentrations of 5, 10, and 15 %wt. It can be seen that small increases in HF concentration had little effect on the morphological change of samples etched at 100 °C.

Samples etched at 120 ºC were similar in morphology until etched with 15 %wt. HF, where the MXene's edges had a rougher surface, showing that smaller increases of etchant concentration can affect the produced material when etched at higher temperature. Samples etched at 150 ºC were successful at 5 and 10 %wt. HF, while the sample etched at 15 %wt. had no yield of MXene but was rather only TiC as indicated by earlier XRD results.

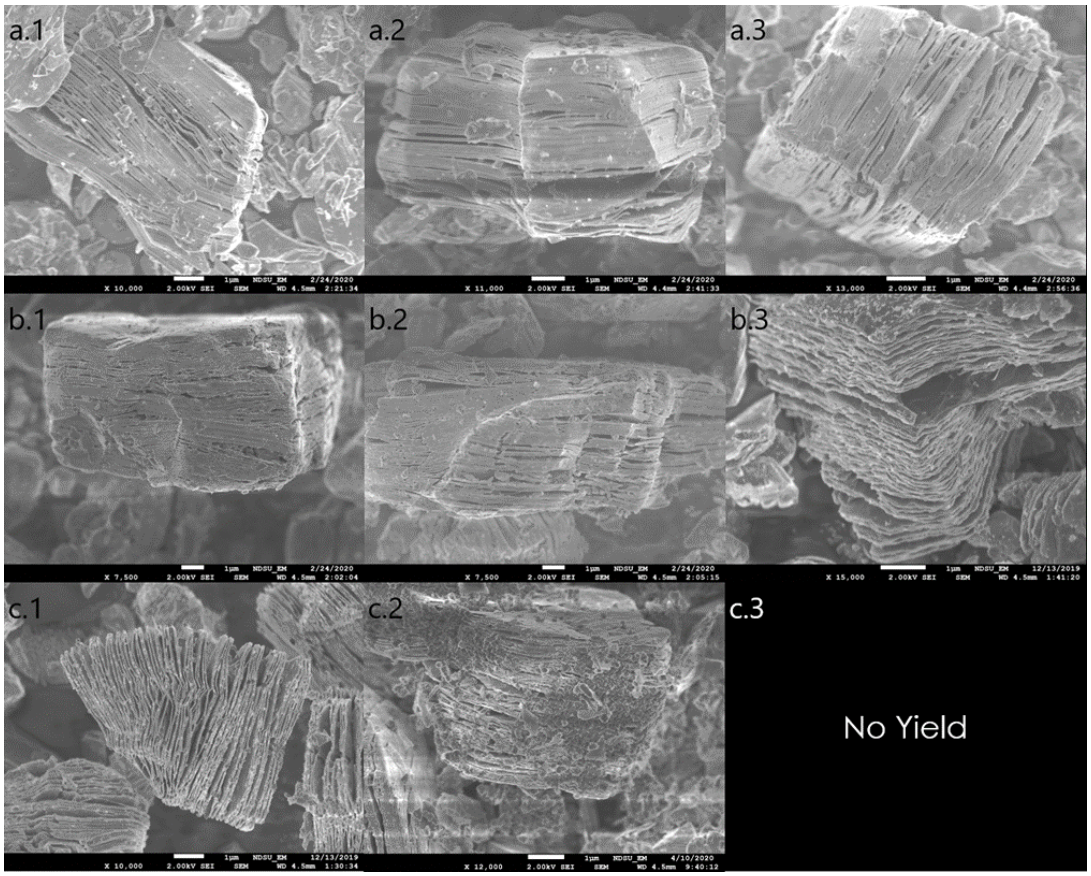

Figure 41. FESEM of Ti_3C_2 samples etched at 100 (a), 120 (b), and 150 (c) ºC and 5 (1), 10 (2), 15 (3) %wt. HF concentration.

The most prominent difference we can see from this figure is the increase in temperature leads to a more exfoliated morphology. While it can be seen the samples etched at 100 and 120 ºC have little difference in morphology with small and uneven layer spacing, while samples etched at 150 ºC show a very pristine accordion like structure with large even layer spacing indicating the highest degree of etching among all samples. On the other hand, it can be seen that

the sample etched at 150 ^{o}C with 10 %wt. HF has many impurities starting to form. We can use this to deduce that increasing the HF concentration actually begins destroying the MXene sample during etching which agrees with other reports of high temperature etching. [120]

Overall, the FESEM data shows that we can successfully etch $Ti_3C_2T_x$ MXenes at high temperature from the Ti_3AlC_2 MAX phase, and that increasing the etching temperature makes changes to the HF concentration much more impactful to the final MXene material's morphology. We can also gather from this data that tuning the temperature and HF concentration conditions could allow for the control over the final material's layer spacing.

Comparing to the XRD data in **Figure 39** it can be seen in **Figure 41 c.2** that the formation of impurities on the surface of the sample begins to accumulate, which corresponds well with this XRD data showing that this impurity is the formation of TiC. It can also be seen looking back at **Figure 41 b.3** that there is a surface roughness to the edges of the MXene sheets. This corresponds well with the XRD data in **Figure 38** that shows this particular sample begins to show less purity than the other two samples etched at this temperature showing signs of decomposition of the MXene material from the etching process.

Based on these experiments, we have shown that high temperature etching at 150 ^{o}C to synthesize Ti_3C_2 MXene material yields a larger layer spacing as compared to lower temperature etching methods. However, it has also been shown that this etching process is very extreme and thus yields lower purity sample due to the MXene material decomposing into TiC. It has also been shown that at these high of etching temperatures a smaller change in HF concentration yields more morphological difference between samples. These high temperature etching methods could be used to create MXenes with different layer spacing allowing for a more varied use in areas such as sensors, energy-storage, and electronics.

3.3. Ti_3C_2MXene-Based Sensor to Guide Lung Cancer Therapy and Management

Lung, breast, pancreas, colon, skin, and stomach cancers are some of the most common forms of cancers that occur. [121] Of them, lung cancer is the second most common cancer in men and women and is the leading cause of cancer related deaths in the United States. There are two major forms of lung cancer, small cell lung cancer (SCLC, ~15%) and non-small cell lung cancer (NSCLC, ~85%), with both having low rates of survival. [122-124] According to the American Cancer Society, lung cancer and asbestos-related lung cancer alone were responsible for 142,670 estimated deaths in 2019. [125] This makes it the deadliest cancer at three times the deaths correlated to breast cancer. [126] The reason most cases become so deadly is patients are typically diagnosed at later stages, typically being stage III or IV when diagnosed. [127] To combat this early detection and effective anti-cancer treatments need to be developed. Recently, a variety of methods including nutritional approaches and therapeutic treatments have been found to better treat lung cancer such as chemotherapy, targeted therapy, cyclooxygenase (COX)-2 inhibition, and omega-3 fatty acid dietary manipulation. [128-132]

Beyond these methods, numerous visualization/detection methods are available for tumor detection to diagnose lung cancer, *e.g.*, positron emission tomography (PET), magnetic resonance imaging (MRI), computerized tomography (CT), ultrasonography, endoscopy, and gas chromatography methods such as gas chromatography coupled with mass spectrometry (GC-MS). [133, 134] However, multiple major issues arise in some if not all of these methods. For example, MRI is very expensive and time-consuming with results that cannot distinguish between malignant and benign cancer. [135] For PET, radioactive material needs to be combined with glucose which is then injected into the patient, and this can be a major issue for those who live with diabetes. [136] CT scans involve high doses of radiation, which makes the patient at

higher risks for cancers. [137] Ultrasound has accuracy issues upon diagnosis. [138] Endoscopy can cause complications such as perforation, infection, bleeding, or pancreatitis. [139] Lastly, the fundamental working concept of (GC-MS) is the samples must volatile, limiting the number of viable tests which can be done. [140] Also, all of these methods require highly trained individuals to collect and interpret results which takes a fair amount of time and makes these tests fairly expensive. Therefore, an effective and accurate means of cancer diagnosis which can aid in treatment is sorely needed.

It has been shown that cyclooxygenase (COX), more specifically COX-2, is overexpressed in lung cancer, which leads to an abundance of the enzymatic product prostaglandin E_2 (PGE_2). PGE_2 is a deleterious metabolite formed from COX-2-catalyzed peroxidation of an upstream omega-6 (ω-6) fatty acid called arachidonic acid (AA), PGE_2 promotes tumor growth and metastasis. [141] Many efforts in lung cancer therapy have been focused on the development of COX-2 inhibitors as they have been shown to suppress PGE_2 formation from COX-2-catalyzed ω-6 arachidonic acid peroxidation. [142] However, most COX-2 inhibitors can severely injure the gastrointestinal tract, increase the risk of cardiovascular disease, and have provided limited clinical responses. [141, 142]

Seeking a safer and more efficient method to treat cancers, a new anti-cancer strategy, as shown in **Figure 42**, has been recently developed, which has a very different approach than classic COX-2 inhibitors. [143-145] This is a strategy that uses dihomo-γ-linolenic acid (DGLA), an ω-6, in the daily diet combined with the commonly high level of COX expressed in most cancers to promote the formation of 8-hydroxyoctanoic acid (8-HOA), a novel anti-cancer free radical by-product. This is accomplished using delta-5-desaturase inhibitor (D5Di). D5D is an enzyme that converts an upstream DGLA in a diet to AA. The high expression of COX-2 will

typically promote the conversion of AA to PGE_2, however, the D5Di will (1) knock down the conversion of DGLA to AA and limit the generation of PGE_2 by reducing its precursor; and (2) promote the COX-2-catalyzed DGLA peroxidation to form 8-HOA. This strategy has proven to be a more effective and safer therapeutic outcome in cancer treatment and has been validated in colon and pancreatic cancers. [146] Therefore, detection of the PGE_2 and 8-HOA, the final products of each metabolic pathway, in lung cancer should be an effective method to evaluate the effectivity of this cancer treatment. Furthermore, the relative ratio of PGE_2 and 8-HOA concentrations may become a useful method to help diagnose cancers at an early stage. However, due to the extremely low concentrations of PGE_2 and 8-HOA in cancer cells, typically in ng/mL or μM concentrations, the detection of these components is quite challenging. Traditional methods of measuring low concentrations of compounds, such as PGE_2 and 8-HOA, are using gas chromatography–mass spectrometry (GC–MS) or liquid chromatography–mass spectrometry (LC–MS). These techniques, as described earlier, are accurate and sensitive but heavy, expensive, time-consuming, and cannot provide in-time feedback.

Utilizing the hot-etched Ti_3C_2 MXene-based nanosensor to effectively detect 8-HOA in cancer cells with and without using a D5D inhibitor is explored. [147] The new sensor based on the two-dimensional nanomaterial, Ti_3C_2 MXene, can facilitate the diagnosis and treatment of lung cancers by using the new D5D inhibitor and 8-HOA therapy. The sensor device works on a simple resistive change mechanism, and the preliminary data indicates that this sensor device can sensitively detect PGE_2 and 8-HOA levels in healthy and cancerous lung cells (BEAS2B and A549 respectively) with similar accuracy to GC–MS but with an in-time manner to guide the cancer treatment through multiple stages.

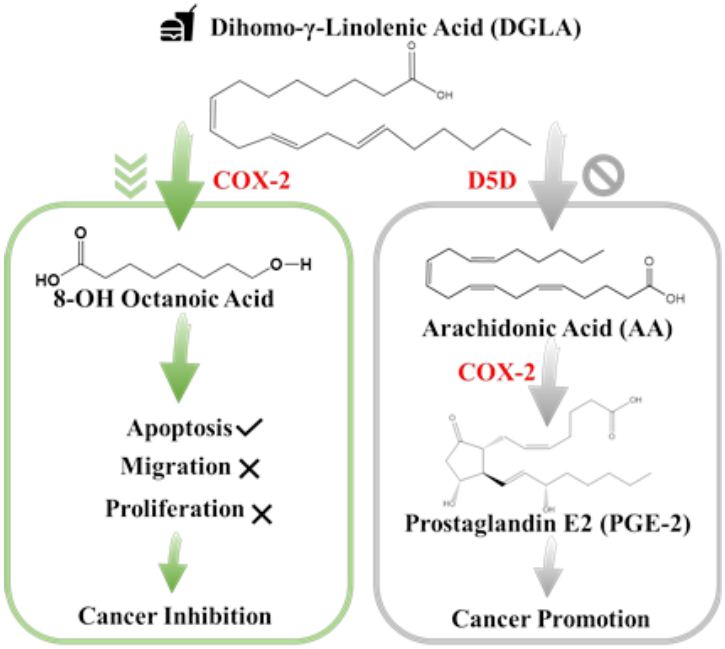

Figure 42. New anti-cancer strategy: target but do not inhibit cyclooxygenase-2 (COX-2) in cancer. [147]

3.3.1. Materials and Methods

The Ti_3C_2 MXene material was made using the new hot-etch method at 150 ^oC in an HF concentration of 5%wt with an etch time of 5 hours at temperature. The sample was let cool naturally then sonicated in a sonication bath for 1 hour. The resulting MXene powder was washed with DI water, collected via centrifugation, and dried overnight at 65 ^oC. A paste was made using the resulting material and ethanol. This paste was then blade coated onto a glass substrate with Au patterned electrodes and let dry.

Cancer cell lines of A549 (ATCC®CCL-185™), NCI-H1299 (ATCC® CRL-5803), and BEAS-2B (ATCC®CRL-9609™) were purchased from American Type Culture Collection (ATCC, VA, USA). Iminodibenzyl (CAS Number: 494-19-9) and 8-hydroxyoctanoic acid (8-HOA) were obtained from Sigma-Aldrich (St. Louis, MO, USA). PGE_2 and DGLA (for in vitro study) and DGLA ethyl ester (for in vivo study) were acquired from Cayman Chemical (Ann Arbor, MI, USA).

About 3×10^5 A549 or BEAS-2B cells were trypsinized and seeded into each well of the 6-well plates. Then, the cells were randomly assigned into different groups for the administration of DGLA (100 μM), iminodibenzyl (10 μM), or their combination accordingly. After 48 h, the cell culture medium was collected. Cells were washed with phosphate buffer solution (PBS) and collected by centrifugation after trypsinization. A 1 mL cell culture medium with collected cells was homogenized and ready for testing. Three different groups of control samples were prepared using the same preparation procedures, including (a) blank group in 1 mL cell homogenate without any treatment; (b) 8-HOA group in 1 mL cell homogenate containing 0.6 ug/mL exogenous 8-HOA; (c) PGE_2 group in 1 mL cell homogenate containing 6 ug/mL exogenous PGE_2.

3.3.2. Ti_3C_2-Based Cancer Sensor Results

3.3.2.1. Non-Cancerous Cells

To test the sensor response of 8-HOA and PGE_2 in normal lung cells, 10^6 BEAS2B non-tumorigenic epithelial cell lines were collected. 8-HOA, PGE_2, and BSA (Bovine Serum Albumin) were applied to the samples right before measuring any resistance change. Once the samples were applied onto the Ti_3C_2 MXene-based sensors, resistances were measured immediately and repeated at regular time intervals. The experiment parameters are listed in **Table A2**. The resistance change of the MXene slides for each of the samples is measured and shown in **Figure 43**, which shows the resistance increases dramatically when BEAS2B is added PGE_2 but BEAS2B alone and BEAS2B with 8-HOA do not show obvious change of resistance.

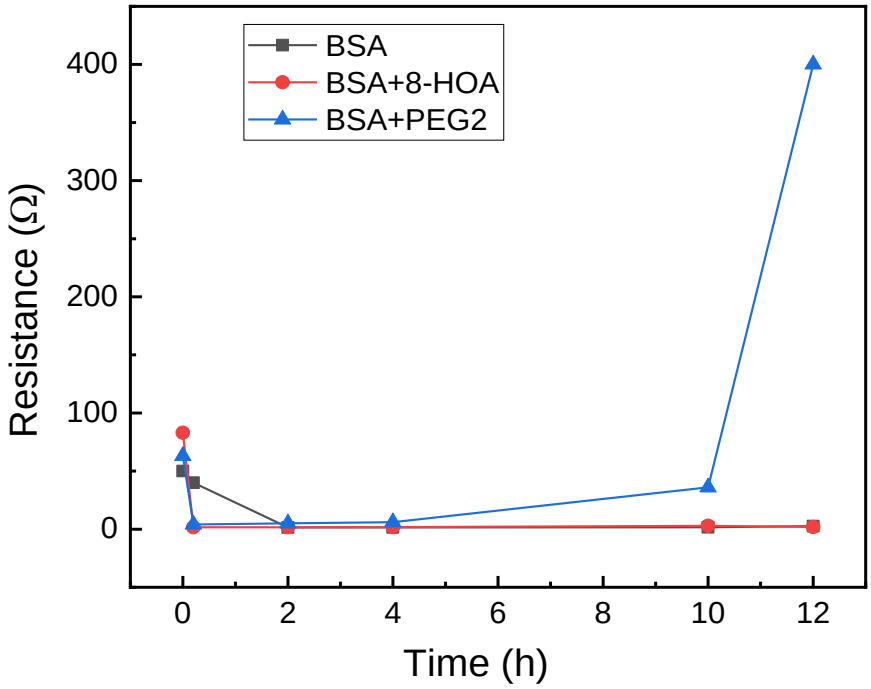

Figure 43. Resistance change measured using Ti_3C_2 MXene-based sensors for BEAS2B cells.

This sensing test is conducted on normal lung cells, BEAS2B, without extra treatment and by treating the cells with extra PGE_2 or 8-HOA. A significant resistance increase is observed in BEAS2B by adding 10 µM PGE_2, while the untreated normal cells and cells treated by 8-HOA do not show any obvious resistance change. This result indicates a unique role of PGE_2 in healthy cells through the change of the electrical property of sensing material. Considering the elevated concentration of PGE_2 can indicate a cancer development, such a sensitive response to PGE_2 in normal cells using Ti_3C_2 MXene-based sensor can be potentially used to diagnose cancer even at a very early stage.

3.3.2.2. Cancerous Cells

In sensing tests, A549 cells were collected after being cultured. The complete design of the experiment to verify the relative concentration of generated 8-HOA and PGE_2 with and without using the new cancer treatment via the detection of Ti_3C_2 Mxene-based sensor are listed

in **Table A3**. Like the BEAS-2B cell lines, 8-HOA and PGE_2 samples were applied to the A549 cell lines just before conducting the experiment. The sensing tests of these samples are shown in **Figure 44**. The resistances of A549 cancer cells, A549 cells treated by DGLA, and PGE_2 are much higher than the cancer cells treated by adding 8-HOA, applying D5Di, or using the new anti-cancer treatment DGLA + D5Di.

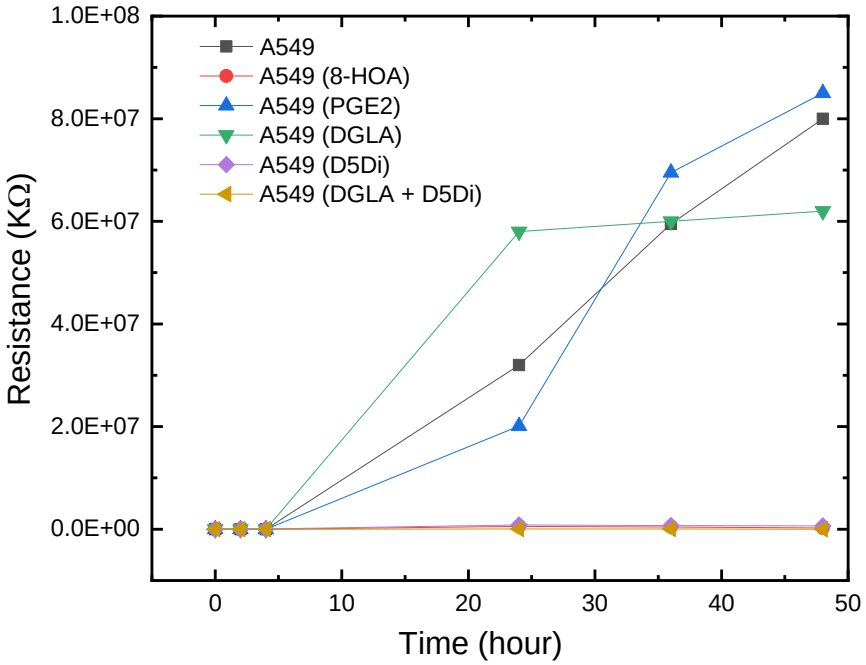

Figure 44. Resistance change measured using Ti_3C_2 MXene-based sensors for A549 cancer cells with and without using the new anti-cancer treatment.

As discussed previously, D5Di is used to prevent the conversion of DGLA to AA and therefore limiting PGE_2 created. The main mechanism of the new anti-cancer strategy uses D5Di along with DGLA to limit the formation of PGE_2, while at the same time promoting the formation of 8-HOA. The sensing tests using the Ti_3C_2 MXene-based sensor exhibits an interesting trend of resistance changes; showing high resistance for A549, A549 with 10 uM PGE_2, and A549 treated by DGLA in the sensing test. These results indicate a higher concentration of PGE_2 generated in A549 cells while the high resistance in the sample only

treated by DGLA confirms that omega-6 (DGLA) are pro-inflammatory and promote the formation of PGE_2, and thus increases material resistance which correlates well to the results found in **Figure 43**. Moreover, the new anti-cancer treatment using DGLA and D5Di to treat A549 cells shows a similar low resistance level to that of A549 cells with 8-HOA. This result indicates promising information: the Ti_3C_2 MXene-based sensor can be used to monitor or validate the anti-cancer effect of this new anti-cancer strategy.

3.3.2.3. Correlation Between Sensing Test Results and GC–MS Results

To verify the Ti_3C_2-based sensor results for PGE_2 and 8-HOA detection, both the sensor and GC–MS have been used to detect very low concentrations of 8-HOA and PGE_2 in A495 lung cancer cells. The Ti_3C_2 Mxene sensors can provide the information of concentration of 8-HOA via the value of resistance change while GC–MS can quantitatively provide the exact concentration of 8-HOA. As shown in **Figure 45**, an obvious correlation is obtained between the GC–MS measurement and resistances that the Ti_3C_2 MXene-based sensor measured. This correlation further confirmed the capability of the Ti_3C_2 MXene-based sensor to detect trace concentrations of 8-HOA. Proving further it can be a convenient, fast, and low-cost tool to help the anti-cancer strategy in lung cancer treatment.

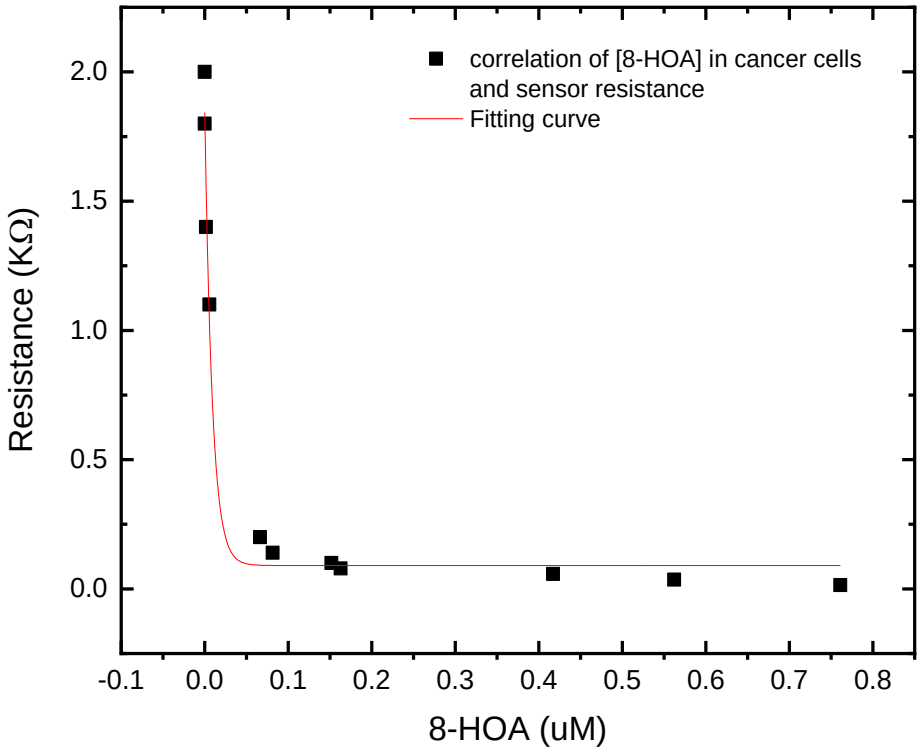

Figure 45. Correlation between different concentration of 8-HOA detected by gas chromatography–mass spectroscopy (GC–MS) and resistance measured by Ti_3C_2 MXene sensor using the same sampling conditions.

3.4. Concluding Remarks and Future Work

MXenes have been shown to be a very versatile material with numerous applications. This is due to the vast number of variables that can be altered to tailor the material for specific use. Here, it is shown that a knowledge of the precursor MAX phase is required to create this material for specific uses, and there are multiple etching methods that give varying results. The synthesis of $Ti_3C_2T_x$ MXenes at high temperature was done using both the standard HF and MILD methods of etching. It was shown that this is a viable route of synthesis for MXenes and it can have the interesting effect, using standard HF method, of controlling the gap between sheets via etching temperature. Additional research should be done to see morphology of MILD

MXenes and developing an experiment to see how hot-etching effects the surface functional group composition could also be done to better find how the material can be tuned.

Additionally, a new sensor based on 2D nanosheets, Ti_3C_2 MXene, has been designed and used for the sensing response to 8-HOA and PGE_2 in lung cancer cells. The preliminary results indicate an important conclusion: this new Ti_3C_2-based sensor can provide a convenient and simple method for anti-cancer treatment guidance. In addition, the high sensitivity of this new sensor opens a potential application for early-stage cancer detection via monitoring variation of PGE_2 and 8-HOA in cells. Future work should include testing the functional groups as a variable for sensitivity of PGE_2 and 8-HOA in cells, as this could help identify a mechanism for sensing and allow for future optimization of the sensing material. Instead of using heavy, expensive, and time-consuming GC–MS to assist the anti-cancer treatment, the Ti_3C_2 MXene-based sensor can provide a fast, simple, low-cost, highly efficient, and much less invasive assistant tool to detect and cure cancer.

4. 1D NANOROD/2D NANOSHEET NANOCOMPOSITE FOR ACETONE SENSING[3]

4.1. Introduction

Sensing materials can be improved either through modification of sensor device configuration/structure or combination with other nanomaterials to form nanocomposites in order to facilitate interaction with gas acetone molecules. For example, ZnO-CuO core-hollow cube nanostructures-based p-n heterojunction chemiresistive sensor exhibits a remarkable response to acetone at 200 °C. The lowest concentration can be detected down to 0.04 ppm with high selectivity and excellent stability for up to 40 days. [148] However, these sensors typically operate at an elevated temperature of at least 200 °C, which will increase the power requirement and overall cost of the final devices. However, as discussed earlier, the newly as-synthesized KWO nanorods has been validated to be able to operate at room temperature with both a sensitive and a selective response to acetone. This is because the KWO-based sensing mechanism is different than traditional MOS-based chemiresistive sensors, due to its unique material and surface properties, which were explored earlier. Briefly, this chapter focuses on the *p*-type semiconductor property, high surface area and porous morphology, and specifically the room-temperature ferroelectric property. All these structural and material properties enable nanostructured KWO to effectively interact with the high dipole-moment compound, acetone, which then causes a detectable change of the resistance even at low concentrations. However, the results indicate that water vapor can cause a strong interference and baseline shift to weaken KWO sensing performance. [61] Herein, a solution which can effectively address the water

[3] The material in this chapter was co-authored by Michael Johnson and Danling Wang. Michael had primary responsibility for developing and carrying out material synthesis methods, as well as collection and analysis of XRD and SEM data. Michael was the primary developer of the conclusions that are advanced here. Michael also drafted and revised all versions of this chapter. Danling served as proofreader and checked the data and conclusions conducted by Michael.

vapor interference and baseline shift in KWO-based sensors is presented by combining KWO with Ti_3C_2 MXene nanosheets.

As presented in chapter 2, a new two-dimensional (2D) nanomaterial, $Ti_3C_2T_x$ (T_x stands for OH, O, and F surface terminal groups), has successfully been synthesized in various ways. Due to the unique multi-layered structure, extremely large surface/interface area, metallic conductivity, and flexible surface functionality $Ti_3C_2T_x$ MXenes attract a lot of attention in the field of biomedical sensing and energy storage due to outstanding signal to noise ratios. [149–152] Motivated by these findings, here, we aim to explore the potential of using a combination of 1D KWO and 2D $Ti_3C_2T_x$ to form a new nanocomposite as the sensing material for acetone detection with a low cost, high sensitivity and selectivity, low noise, low interference from water vapor, while maintaining room-temperature operation.

4.2. Synthesis Methods and Characterization

The standard method of hydrothermal synthesis for KWO was described in chapter 1. Briefly, a precursor solution containing $Na_2WO_4 \cdot 2H_2O$ (95%, Alfa Aesar, Haverhill, MA, USA), oxalic acid dihydrate (>99%, VWR, Radnor, PA, USA), K_2SO_4 (>99%, VWR, Radnor, PA, USA) and HCl (36%–38%, Aqua Solutions Inc. Deer Park, TX, USA) was made. This solution was then put into a 30 ml autoclave for synthesis. KWO samples were grown at 225 °C for 24 hours, then collected via centrifuge.

The synthesis methods for MXenes were described in chapter 2. It can be broken down into two basic methods; standard HF etching, and MILD etching both of which can be done at higher temperatures, up to 150 ^oC. Here, both hot-etched Ti_3C_2 MXene made at 150 ^oC, 5 %wt. HF; and Ti_3C_2 MXene made via the MILD method at room-temperature are explored for their efficacy as part of the 1D/2D nanocomposite for acetone sensing.

4.2.1. Electrostatic Assembly of Accordion-Like MXene Nanosheets and KWO Nanorods

The KWO sensor nanomaterial was synthesized using the hydrothermal method described above. Pure $Ti_3C_2T_x$ MXene was synthesized based on a HF etching method. The hot etching method, which can make high-yield, high purity $Ti_3C_2T_x$ MXene, was used. A total of 0.5 g of MAX phase was etched using HF acid in a 25 ml Teflon lined autoclave at temperature of 150 °C for five hours in a Thermolyne furnace. A concentration of 5 %wt. HF was used to remove Al-layers from the MAX phase. Materials were then sonicated for 1 hour using a sonicating bath and collected via centrifuge. All materials were then dried overnight at 65 °C in a drying oven.

The nanocomposite film made by KWO and $Ti_3C_2T_x$ MXene was formed with variable material ratios of KWO/$Ti_3C_2T_x$–1:1, 1:2, 1:5, 2:1, 4:1, and 9:1 using electrostatic self-assembly technique. In detail, amounts of as-synthesized KWO nanorods were dispersed into distilled water and sonicated for 1h. Then, 10mg of as-synthesized $Ti_3C_2T_x$ nanosheets were added to 10 mL distilled water and sonicated for 1h. Thereafter, the homogeneous KWO solution was poured into the $Ti_3C_2T_x$ solution. After that, the mixture was stirred vigorously for 12 hours. Finally, the obtained KWO/$Ti_3C_2T_x$powder was washed three times with distilled water and dried at 80 °C for 24 h; Finally, eight as-synthesized nanomaterials including $Ti_3C_2T_x$, KWO, and KWO/$Ti_3C_2T_x$ (1:1, 1:2, 1:5, 2:1, 4:1, and 9:1) were made into thin films using blade-coating technique onto the gold-electrode patterned glass substrates. These nanocomposites were then characterized using XRD and SEM. [153]

4.2.1.1. X-Ray Diffraction

The XRD patterns of the as-synthesized samples (KWO, $Ti_3C_2T_x$ MXene, and KWO/$Ti_3C_2T_x$ nanocomposites) are shown in **Figure 46**. The peak at $2\theta = 9.0°$ is corresponding

to the *(002)* facet of $Ti_3C_2T_x$. While the peaks at 2θ = 23°, 28° correspond to *(002)* and *(200)* of KWO. As found in chapter 1, the relative peaks *(002)*/*(200)* of KWO play an important role to realize the selective detection of acetone. The XRD spectrum of KWO/$Ti_3C_2T_x$ (2:1) nanocomposite has shown the strongest relative peak at *(002)*. In addition, nanocomposites show higher crystalline structure while the ratio of KWO/$Ti_3C_2T_x$ is higher. Beside these, the much weaker intensity of MXene observed in XRD indicates that the content of the $Ti_3C_2T_x$ in the composite is very low, as expected. The low content of $Ti_3C_2T_x$ in the nanocomposites means $Ti_3C_2T_x$ will not cause dramatic change of material properties, e.g., *p*-type semiconducting, and ferroelectricity, but KWO has interacted with $Ti_3C_2T_x$ in the nanocomposites and caused the change of the expressed crystal facets.

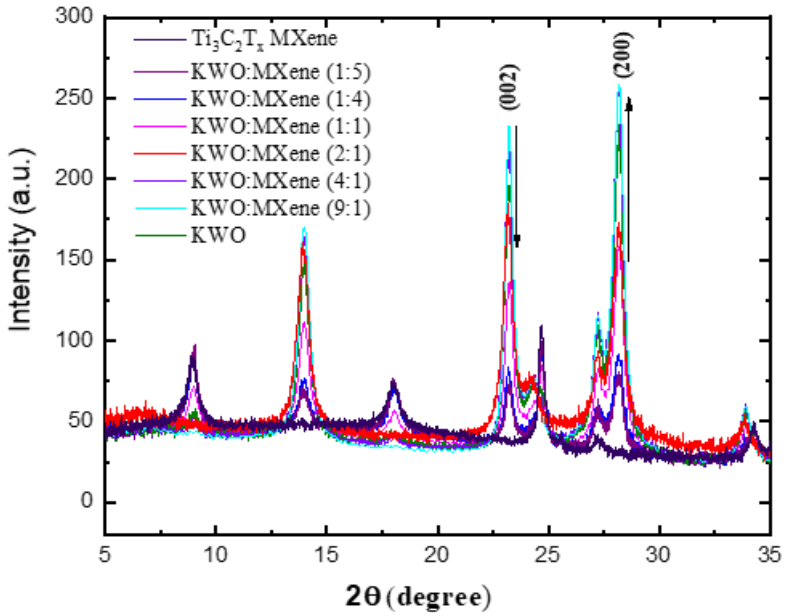

Figure 46. XRD spectra of KWO nanorods, $Ti_3C_2T_x$MXene, and KWO/$Ti_3C_2T_x$ nanocomposites, and $Ti_3C_2T_x$ MXene.

4.2.1.2. Scanning Electron Microscopy

The microstructures and morphologies of the as-synthesized nanomaterials: KWO, $Ti_3C_2T_x$, KWO/$Ti_3C_2T_x$ nanocomposites have been investigated by SEM. As shown in **Figure 47**

a, the SEM image of KWO clearly shows a three-dimensional mesh of randomly orientated and interconnected nanorods with several μm in length and 20–50 nm in diameter. The SEM image of pristine $Ti_3C_2T_x$ MXene (**Figure 47 b**) exhibits multilayered structure and accordion-like morphology. **Figure 47 c–f** show the SEM images of the KWO/$Ti_3C_2T_x$ nanocomposites at the ratio 1:1, 2:1, 4:1, and 9:1, which all indicate a rougher surface due to the decoration of the KWO nanorods on the $Ti_3C_2T_x$ nanosheets and illustrate the successful construction of the 1D/2D KWO/$Ti_3C_2T_x$ hybrids. This could suggest a strongly coupled interaction between KWO and $Ti_3C_2T_x$.

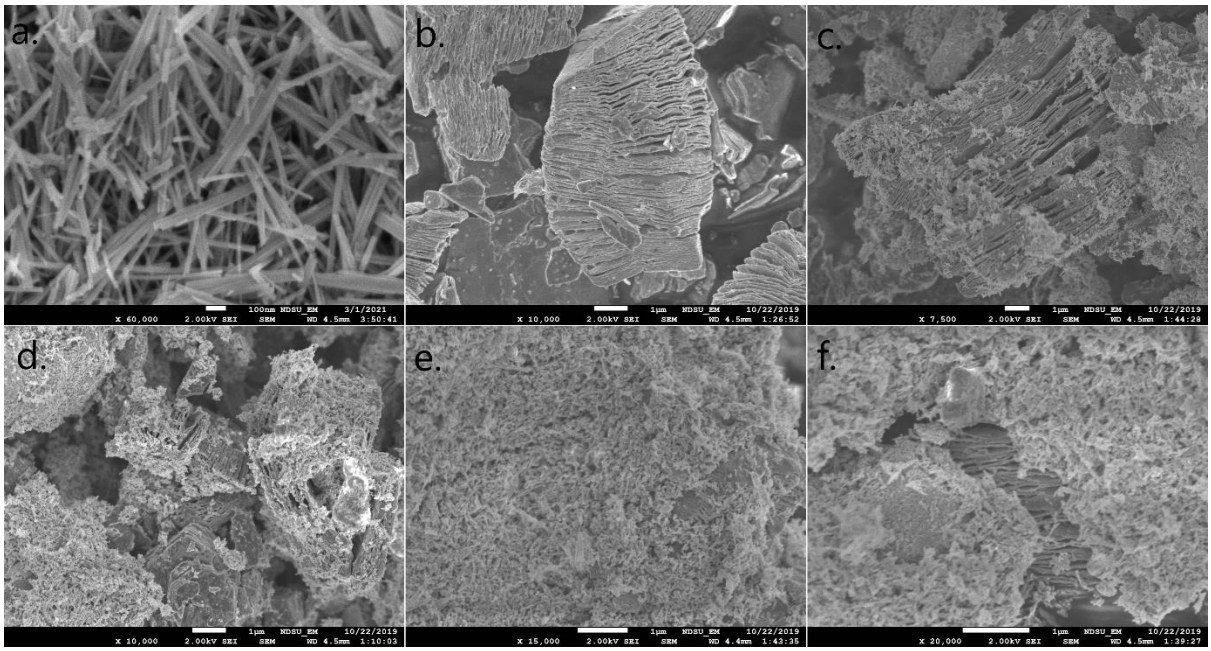

Figure 47. SEM images of (a) KWO nanorods, (b) $Ti_3C_2T_x$, (c) KWO/ $Ti_3C_2T_x$ (1:1), (d) KWO/ $Ti_3C_2T_x$ (2:1), (e) KWO/ $Ti_3C_2T_x$ (4:1), and (f) KWO/ Ti_3C_{2x} (9:1).

4.2.1.3. Acetone Sensing and Humidity Response

The sensing performance of as-fabricated device to detect acetone is still based on a room-temperature chemiresistive response, which was described in chapter 1. Briefly, the detection and sensing response of acetone largely depend on sensing material's chemical, electrical and structural properties. These properties affect charge transfer between sensing

material and analyte gas, and electron/hole diffusion within the nanocomposite. This results in a change in resistance of sensing material. **Figure 48** shows the sensing results of the fabricated nanocomposites, comparing to other nanomaterials, the KWO/$Ti_3C_2T_x$ (2:1) nanocomposite exhibits the highest sensitivity (almost 10 times higher than the response of KWO) to 2.86 ppm acetone at the same sensing condition, RH = 20% and room temperature. This improved sensing performance of KWO/$Ti_3C_2T_x$ (2:1) nanocomposite can be contributed due to 1) the unique surface and electronic properties of $Ti_3C_2T_x$ nanosheets, [106, 152] which can provide better signal to noise ratio and higher sensitivity, 2) the room temperature of ferroelectric property of KWO, and 3) the interaction between KWO and $Ti_3C_2T_x$ creating a more expressed (002) facet. Here, 2D multilayered $Ti_3C_2T_x$ nanosheets not only provide extreme large surface and interface area for the absorption of acetone molecules, but also the surface functional groups, T_x: –O, –OH, and –F. These can act as active sites for the nucleation and growth of the KWO nanorods to enhance the interfacial interactions between KWO and $Ti_3C_2T_x$ and expedite charge transfer/transportation.

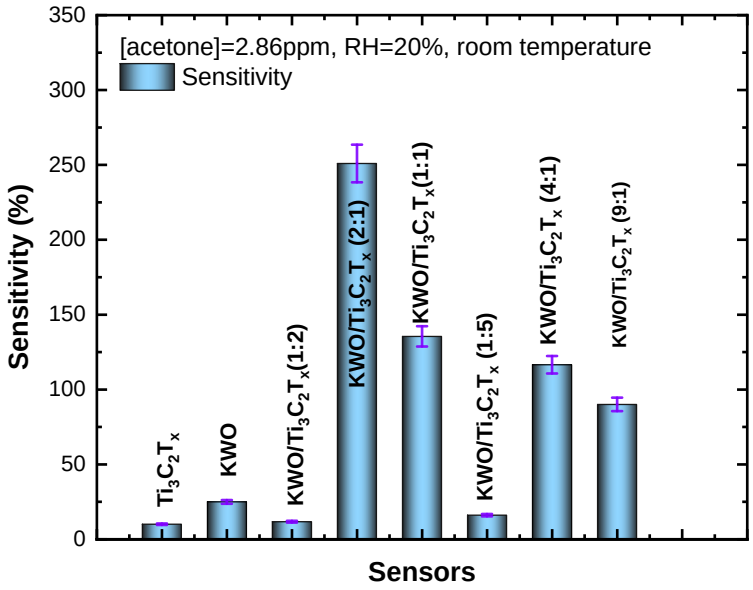

Figure 48. Sensing test on 2.86 ppm acetone at room temperature, RH = 20% using variable sensors based on $Ti_3C_2T_x$ nanosheets, KWO nanorods, KWO/Ti_3C_2Tx (1:2), KWO/$Ti_3C_2T_x$ (2:1), KWO/$Ti_3C_2T_x$ (1:1), KWO/$Ti_3C_2T_x$ (1:5), KWO/$Ti_3C_2T_x$ (4:1), and KWO/$Ti_3C_2T_x$ (9:1).

To evaluate the cross-interference of humidity, the KWO/$Ti_3C_2T_x$ (2:1) nanocomposite-based sensor has been tested under varying levels of relative humidity (RH) at room-temperature. The result is shown in **Figure 49**. The KWO/$Ti_3C_2T_x$ (2:1) nanocomposite shows relative stable baseline resistance (red color) while RH is from 10% up to 86%. Considering the little influence of RH and high sensitivity to acetone, The KWO/$Ti_3C_2T_x$ (2:1) nanocomposite shows the best sensing response to acetone at room temperature.

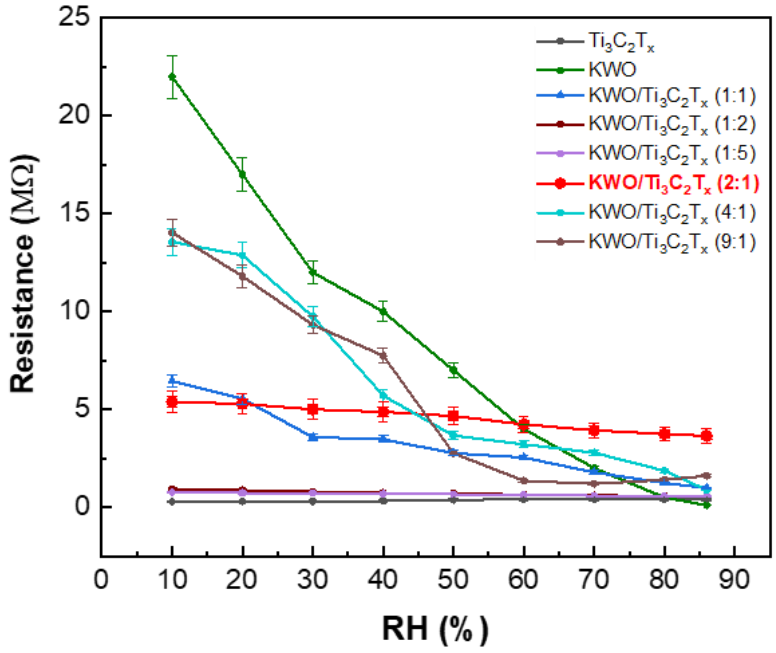

Figure 49. Resistance and RH relationship based on variable nanomaterials: $Ti_3C_2T_x$ nanosheets, KWO nanorods, KWO/$Ti_3C_2T_x$ (1:2), KWO/$Ti_3C_2T_x$ (2:1), KWO/$Ti_3C_2T_x$ (1:1), KWO/$Ti_3C_2T_x$ (1:5), KWO/$Ti_3C_2T_x$ (4:1), and KWO/$Ti_3C_2T_x$ (9:1).

The potential sensing mechanism of the KWO/$Ti_3C_2T_x$ nanocomposite (2:1) to detect acetone, can be explained as: 1) 1D KWO nanorods are a *p*-type semiconductor. Although the nanocomposite has altered the crystal structure of the material, the Hall Effect measurement reveals that KWO/$Ti_3C_2T_x$ nanocomposites still possess *p*-type semiconducting properties. The XRD spectra further shows that the content of $Ti_3C_2T_x$ is much low in comparison to the content of KWO within the nanocomposites. Therefore, the semiconducting properties of the nanocomposites have no change. This means the majority carriers in the nanocomposites are still holes. Once electron rich compounds, such as acetone, absorb onto KWO/$Ti_3C_2T_x$, acetone molecules will donate electrons and then combine with holes to result in the increase of resistance of the sensing materials. 2) The KWO room-temperature ferroelectric property is still the major reason to cause an effective charge transfer between KWO and acetone and realize selective detection of acetone, since pure MXenes show little response to acetone in **Figure 47**.

3) The high electrical conductivity of $Ti_3C_2T_x$ MXene and the interfacial interaction between $Ti_3C_2T_x$ and KWO not only can lower the signal noise, but also can further enhance the charge transfer within the material. In other words, $Ti_3C_2T_x$ MXenes have been used as an efficient charge transfer aid material for biosensors. Herein, it is believed they play a similar role in the KWO/$Ti_3C_2T_x$ material sensing acetone. While they likely do not contribute much to the interaction with acetone, the $Ti_3C_2T_x$ MXenes help to lower the baseline resistance of the sensor film and provide an improved signal to noise ratio. In other words, the $Ti_3C_2T_x$ MXenes work as a type of electron collector which can help KWO more efficiently transfer charge while interacting with acetone. More study into the mechanism at contact between the two materials should be studied to fortify this theory.

The KWO/$Ti_3C_2T_x$ (2:1) nanocomposite is a new functionalized sensing material with great potential for application in the breath acetone sensor device. This device can deliver a low-cost, non-invasive, highly accurate, and portable device with little interference of humidity for early and rapid diabetes detection and long-term health monitoring with extreme high signal-to-noise ratio (SNR).

4.2.2. In-Situ Growth of KWO Nanorods Using Colloidal MILD Solution

To try and achieve a higher interface between KWO and $Ti_3C_2T_x$ MXene, KWO was grown in the presence of colloidal MXene nanosheets made by the MILD etching method. The MILD MXene was made using the standard room-temperature MILD etching procedure discussed in chapter 2. The composite was synthesized by a precursor solution containing $Na_2WO_4 \cdot 2H_2O$ (95%, Alfa Aesar, Haverhill, MA, USA), oxalic acid dihydrate (>99%, VWR, Radnor, PA, USA), K_2SO_4 (>99%, VWR, Radnor, PA, USA) and HCl (36%–38%, Aqua Solutions Inc. Deer Park, TX, USA). This solution was then put into a 30 ml autoclave for

synthesis with varying amounts, 0.1, 0.2, 0.3, 0.4, and 0.5 g, of as-synthesized MILD $Ti_3C_2T_x$ MXene. Samples were then grown at 225 °C for 24 hours, then collected via centrifuge. Samples were then characterized using XRD, SEM, and tested for acetone response.

4.2.2.1. X-Ray Diffraction

Figure 50 shows the results of the XRD taken of KWO/MILD nanocomposite samples grown with 0.1, 0.2, 0.3, 0.4, and 0.5 g of MXene. Immediately, it is easy to see how expressed the *(002)* facet of KWO in samples grown with 0.1, 0.2, and 0.3 g of MXene. This effect becomes more prevalent with increasing MXene up to 0.3 g. On the other hand, little KWO shows on samples grown with 0.4 and 0.5 g of MXene. Also of note, characteristic MXene peaks are not visible within samples grown from 0.1 to 0.3 g. This is likely due to the MXene sheets breaking into smaller pieces as the growth process of KWO happens leading to little observable MXene within the composite but can be seen in the SEM later. Overall, more work should be done to better define the growth of KWO when in the presence of colloidal MXene to better understand the resulting product and the interfacial zone of the two materials.

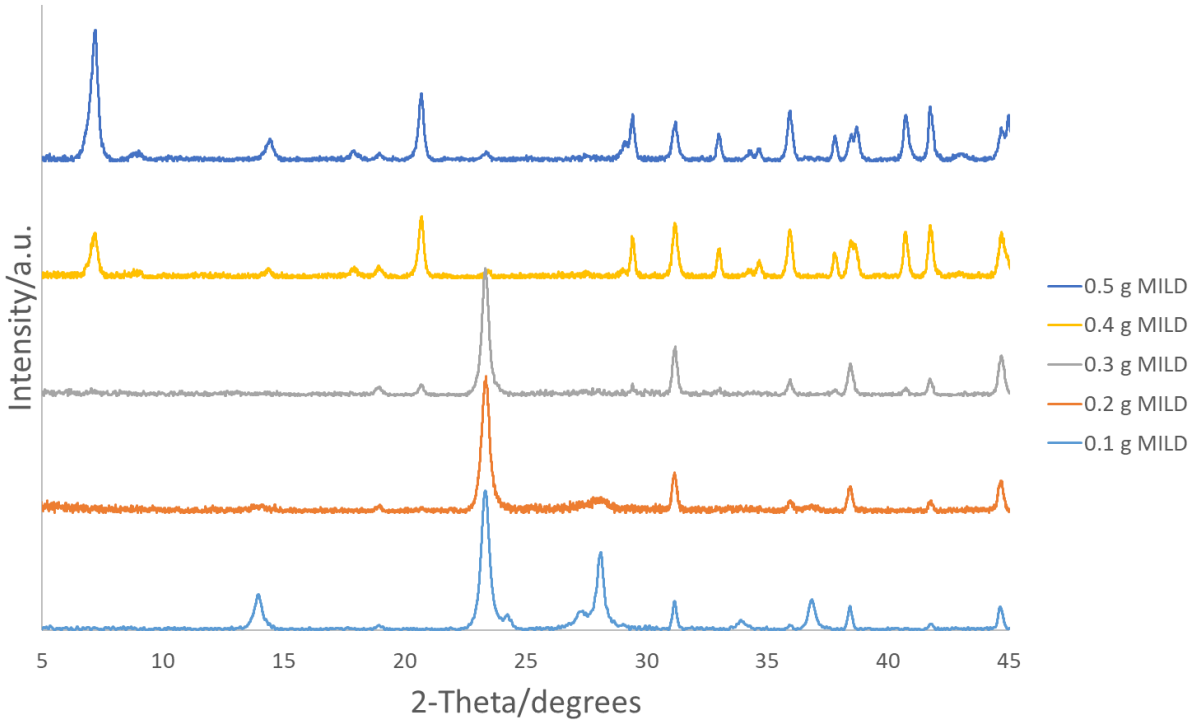

Figure 50. XRD of KWO/$Ti_3C_2T_x$ MILD MXene nanocomposite synthesized hydrothermally with 0.1, 0.2, 0.3, 0.4, and 0.5 g of MILD MXene.

4.2.2.2. Scanning Electron Microscopy

Figure 51 shows the SEM images of KWO/$Ti_3C_2T_x$ MILD MXene nanocomposite synthesized hydrothermally with 0.1, 0.2, 0.3, 0.4, and 0.5 g of MILD MXene. In agreement with the XRD we see little nanorods present in the samples grown with 0.4 and 0.5 g of MXene. The samples grown with 0.1 to 0.3 g of MXene show a change in morphology with longer nanorods as MXene content is increased. The last piece to note is small MXene flakes can be seen in the sample grown with 0.3 g of MXene helping fortify the theory that this material breaks apart into smaller pieces over the course of hydrothermal synthesis.

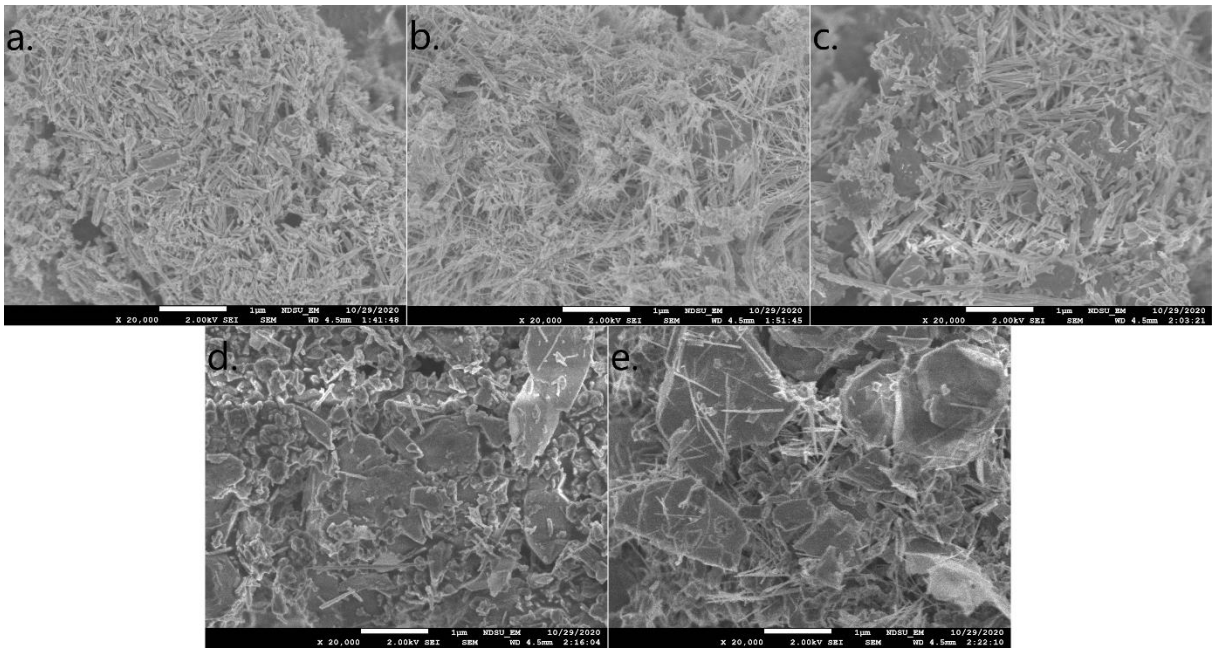

Figure 51. SEM of KWO/$Ti_3C_2T_x$ MILD MXene nanocomposite synthesized hydrothermally with (a) 0.1, (b) 0.2, (c) 0.3, (d) 0.4, and (e) 0.5 g of MILD MXene.

4.3. Concluding Remarks and Future Work

The combination of the two previous materials to improve the acetone sensing performance of tungsten oxide nanorods by greatly increasing sensitivity and mitigating the effect humidity has on these types of sensors. More work to understand the interfacial zone would allow for a clearer picture of the exact mechanism that has these two materials perform well when combined for acetone sensing. This can be done by first studying the content of –OH, -O, and –F surface groups these MXenes present. Synthesis of MILD/KWO nanocomposites has just recently become feasible, and to gain a better understanding of their nature sensing tests should be done to see if they improve upon the already excellent performance standard MXenes have added to acetone sensing. Testing alternate metal-based tungsten oxide nanorods, Li-, Na-, Cu-, and Cr-WO, with MXenes could also prove beneficial for the sensing of acetone.

5. CONCLUSIONS AND FUTURE WORK

In this thesis, two major nanomaterials, KWO for application in diabetes and MXene for cancer management and further improvement of the KWO diabetes sensor, are intensively researched. KWO shows great potential as a breath acetone sensor, which can be utilized to monitor and diagnose diabetes. It also shows the unique ferroelectric property which allows for a room-temperature sensing operation. Synthesis methods and characterization are done to further the understanding of KWO as an acetone sensor and further improve its capability towards becoming the cornerstone of a handheld biomedical sensor which is non-invasive, portable, and easy-to-use. Ti_3C_2 MXenes are studied and characterized under various synthesis conditions to create both accordion-like structures with varying gap widths, and single-to-few layered nanosheets created by the intercalation of Li^+ ions. Additionally, a new sensor based on 2D nanosheets, Ti_3C_2 MXene, has been designed and used for the sensing response to 8-HOA and PGE_2 in lung cancer cells. The preliminary results indicate an important conclusion: this new Ti_3C_2-based sensor can provide a convenient and simple method for anti-cancer treatment guidance. Finally, a nanocomposite is synthesized using both KWO and Ti_3C_2 MXenes to improve the acetone sensor's sensitivity and selectivity by majorly reducing humidity cross-interference.

First, a novel group of chemiresistive nanomaterials, metal doped tungsten oxide (MWO) nanorods, were explored for their ability to work as a sensor for breath-acetone. Tungsten oxide nanorods growth via the hydrothermal method was explained. The basics of the chemiresistive method were studied and applied to the development of multiple samples. First, KWO was studied for proper growth temperature, which was found to be 225 ^oC, to better express its crystallinity and ferroelectric phase, which in-turn improved sensing performance. Then varying

levels of potassium content along with synthesis using surfactant additives was studied to tune the material's crystal facets and increase the ferroelectric property. Continuing, metals beyond K were studied using the same hydrothermal growing method. Initially, other alkali metals Li and Na were studied and compared to the original KWO. It was found that KWO had the best sensitivity, and this was likely due to it also possessing the ferroelectric ε-phase and the *(002)* facet. On the other hand, both LiWO and NaWO samples showed poorer performance than that of KWO. More study into the selectivity and longevity of these materials should also be done to better characterize their sensing properties. Hybrid metals of (K:Li)WO were also synthesized at 1:1 and 3:1 ratios. Both samples presented ε-WO_3 correlating to good ferroelectricity and had very expressed *(002)* peaks in the XRD. They ended up having higher sensitivity than KWO and more study can be done in the future to characterize why.

Next, MXenes have been shown to be a very versatile material with numerous applications. This is due to the vast number of variables that can be altered to tailor the material for specific use. Here, it is shown that a knowledge of the precursor MAX phase is required to create this material for specific uses, and there are multiple etching methods that give varying results. The synthesis of $Ti_3C_2T_x$ MXenes at high temperature was done using both the standard HF and MILD methods of etching. It was shown that this is a viable route of synthesis for MXenes and it can have the interesting effect, using standard HF method, of controlling the gap between sheets via etching temperature. Additional research should be done to see morphology of MILD MXenes and developing an experiment to see how hot-etching effects the surface functional group composition could also be done to better find how the material can be tuned.

Additionally, a new sensor based on 2D nanosheets, Ti_3C_2 MXene, has been designed and used for the sensing response to 8-HOA and PGE_2 in lung cancer cells. The preliminary

results indicate an important conclusion: this new Ti_3C_2-based sensor can provide a convenient and simple method for anti-cancer treatment guidance. In addition, the high sensitivity of this new sensor opens a potential application for early-stage cancer detection via monitoring variation of PGE_2 and 8-HOA in cells. Future work should include testing the functional groups as a variable for sensitivity of PGE_2 and 8-HOA in cells, as this could help identify a mechanism for sensing and allow for future optimization of the sensing material. Instead of using heavy, expensive, and time-consuming GC–MS to assist the anti-cancer treatment, the Ti_3C_2 MXene-based sensor can provide a fast, simple, low-cost, highly efficient, and much less invasive assistant tool to detect and cure cancer.

Finally, the combination of the two previous materials to improve the acetone sensing performance of tungsten oxide nanorods by greatly increasing sensitivity and mitigating the effect humidity has on these types of sensors. More work to understand the interfacial zone would allow for a clearer picture of the exact mechanism that has these two materials perform well when combined for acetone sensing. This can be done by first studying the content of –OH, -O, and –F surface groups these MXenes present. Synthesis of MILD/KWO nanocomposites has just recently become feasible, and to gain a better understanding of their nature sensing tests should be done to see if they improve upon the already excellent performance standard MXenes have added to acetone sensing. Testing alternate metal-based tungsten oxide nanorods, Li-, Na-, Cu-, and Cr-WO, with MXenes as a nanocompsite could also prove beneficial for the sensing of acetone.

REFERENCES

1. Buszewski, B.; Kesy, M.; Ligor, T.; Amann, A., Human exhaled air analytics: Biomarkers of diseases. *Biomedical Chromatography* **2007**, *21* (6), 553-566.

2. Das, S.; Pal, M., Non-Invasive Monitoring of Human Health by Exhaled Breath Analysis: A Comprehensive Review. *Journal of Electrochemical Society* **2020**, *167*, 037562.

3. van de Kant, K.D.; van der Sande, L.J.; Jobsis, Q.; van Schayck, O.C.P.; Dompeling, E., Clinical Use of Exhaled Volatile Organic Compounds in Pulmonary Diseases: A Systematic Review. *Respir Res.* **2012**, *13*, 117.

4. Broza, Y.Y.; Vishinkin, R.; Barash, O.; Nakhleh, M.K.; Haick, H., Synergy Between Nanomaterials and Volatile Organic Compounds for Non-Invasive Medical Evaluation. *Chemical Society Review* **2018**, *47*, 4781–4859.

5. Zhou, X. Y.; Xue, Z. J.; Chen, X. Y.; Huang, C. H.; Bai, W. Q.; Lu, Z. L.; Wang, T., Nanomaterial-based gas sensors used for breath diagnosis. *J. Mater. Chem. B* **2020**, *8*, 3231.

6. de Lacy Costello, B.; Amann, A.; Al-Kateb, H.; Flynn, C.; Filipiak, W.; Khalid, T.; Osborne, D.; Ratcliffe, N. M., A review of the volatiles from the healthy human body. *J. Breath Res.* **2014**, *8*, 014001.

7. Puchalska, P.; Crawford P. A., Multi-dimensional Roles of Ketone Bodies in Fuel Metabolism, Signaling, and Therapeutics. *Cell Metabolism* **2017**, *25* (2), 262-284.

8. Deng, C. H.; Zhang, J.; Yu, X. F.; Zhang, W.; Zhang, X. M., Determination of acetone in human breath by gas chromatography-mass spectrometry and solid-phase microextraction with on-fiber derivatization. *Journal of Chromatography B-Analytical Technologies in the Biomedical and Life Sciences* **2004,** *810* (2), 269-275.

9. Španěl, P.; Smith, D., What is the real utility of breath ammonia concentration measurements in medicine and physiology?. *J. Breath Res.* **2018**, *12* (2), 027102.

10. Obermeier, J.; Trefz, P.; Happ, J.; Schubert, J. K.; Staude, H.; Fischer, D. C.; Miekisch, W., Exhaled volatile substances mirror clinical conditions in pediatric chronic kidney disease. *PLoS ONE* **2017,** *12* (6), e0178745.

11. Limeres, J.; Garcez, J. F.; Marinho, J. S.; Loureiro, A.; Diniz, M.; Diz, P., A breath ammonia analyser for monitoring patients with end-stage renal disease on haemodialysis. *Br. J. Biomed. Sci.* **2017**, *74*, 24–29.

12. Guo, Y.; Hong, C.; Liu, Y.; Chen, H.; Huang, X.; Hong, M., Diagnostic value of fractional exhaled nitric oxide for asthma-chronic obstructive pulmonary disease overlap syndrome. *Medicine* **2018**, *97* (23), e10857.

13. Smith, D.; Španěl, P.; Fryer, A. A.; Hanna, F.; Ferns, G. A., Can volatile compounds in exhaled breath be used to monitor control in diabetes mellitus?. *J. Breath Res.* **2011**, *5* (2), 022001.

14. Davies, S.; Španěl, P.; Smith, D., A new 'online' method to measure increased exhaled isoprene in end-stage renal failure. *Nephrol., Dial., Transplant.* **2001**, *16* (4), 836-839.

15. Bajtarevic, A.; Ager, C.; Pienz, M.; Klieber, M.; Schwarz, K.; Ligor, M.; Ligor, T.; Filipiak, W.; Denz, H.; Fiegl, M.; Hilbe, W.; Weiss, W.; Lukas, P.; Jamnig, H.; Hackl, M.; Haidenberger, A.; Buszewski, B.; Miekisch, W.; Schubert, J.; Amann, A., Noninvasive detection of lung cancer by analysis of exhaled breath. *Bmc Cancer* **2009,** *9*, 16.

16. Alkhouri, N.; Singh, T.; Alsabbagh, E.; Guirguis, J.; Chami, T.; Hanouneh, I.; Grove, D.; Lopez R.; Dweik, R., Isoprene in the Exhaled Breath is a Novel Biomarker for Advanced Fibrosis in Patients with Chronic Liver Disease: A Pilot Study. *Clin. Transl. Gastroenterol.* **2015**, *6* (9), e112.

17. Bures, J.; Cyrany, J.; Kohoutova, D.; Forstl, M.; Rejchrt, S.; Kvetina, J.; Vorisek, V.; Kopacova, M., Small intestinal bacterial overgrowth syndrome. *World J. Gastroenterol.* **2010**, *16* (24), 2978-2990.

18. Kunkel, D.; Basseri, R. J.; Makhani, M. D.; Chong, K.; Chang, C.; Pimentel, M., Methane on Breath Testing Is Associated with Constipation: A Systematic Review and Meta-analysis. *Dig. Dis. Sci.* **2011**, *56*, 1612-1618.

19. Kerlin, P.; Wong, L., Breath hydrogen testing in bacterial overgrowth of the small intestine. *Gastroenterology* **1988**, *95* (4), 982-988.

20. Pimentel, M.; Mayer, A. G.; Park, S.; Chow, E. J.; Hasan, A.; Kong, Y., Methane Production During Lactulose Breath Test Is Associated with Gastrointestinal Disease Presentation. *Dig. Dis. Sci.* **2003**, *48*, 86-92.

21. Choi, K. I.; Kim, H. J.; Kang, Y. C.; Lee, J. H., Ultraselective and ultrasensitive detection of H_2S in highly humid atmosphere using CuO-loaded SnO_2 hollow spheres for real-time diagnosis of halitosis. *Sens. Actuators, B* **2014**, *194*, 371–376.

22. Miekisch, W.; Schubert, J. K.; Noeldge-Schomburg, G. F., Diagnostic potential of breath analysis—focus on volatile organic compounds. *Clin. Chim. Acta* **2004**, *347*, 25–39.

23. Cheng, C. S.; Chen, Y. Q.; Lu, C. J., Organic vapour sensing using localized surface plasmon resonance spectrum of metallic nanoparticles self assemble monolayer. *Talanta* **2007**, *73* (2), 358–365.

24. Tao, W.; Lin, P.; Ai, Y.; Wang, H.; Ke, S.; Zeng, X., Multichannel quartz crystal microbalance array: Fabrication, evaluation, application in biomarker detection. *Anal. Biochem.* **2016**, *495*, 85-92.

25. Chikkadi, K.; Muoth, M.; Roman, C.; Haluska, M.; Hierold, C., Advances in NO_2 sensing with individual single-walled carbon nanotube transistors. *Beilstein J. Nanotechnol.* **2014**, *5*, 2179–2191.

26. Yao, M. S.; Lv, X. J.; Fu, Z. H.; Li, W. H.; Deng, W. H.; Wu, G. D.; Xu, G., Layer-by-Layer Assembled Conductive Metal–Organic Framework Nanofilms for Room-Temperature Chemiresistive Sensing. *Angew. Chem., Int. Ed.* **2017**, *56* (52), 16510–16514.

27. Pei, Y. Y.; Zhang, X. L.; Hui, Z. Y.; Zhou, J. Y.; Huang X.; Sun, G. Z.; Huang W., Ti3C2TX MXene for Sensing Applications: Recent Progress, Design Principles, and Future Perspectives. *ACS Nano* **2021**, *15* (3), 3996-4017.

28. Hibbard, T.; Killard, A. J., Breath Ammonia Analysis: Clinical Application and Measurement. *Critical Reviews in Analytical Chemistry* **2011,** *41* (1), 21-35.

29. Lindinger, W.; Hansel, A., Analysis of trace gases at ppb levels by proton transfer reaction mass spectrometry (PTR-MS). *Plasma Sources Science & Technology* **1997,** *6* (2), 111-117.

30. Phillips, M.; Herrera, J.; Krishnan, S.; Zain, M.; Greenberg, J.; Cataneo, R. N., Variation in volatile organic compounds in the breath of normal humans. *Journal of Chromatography B* **1999,** *729* (1-2), 75-88.

31. Mürtz, M., Breath Diagnostics Using Laser Spectroscopy. *Optics & Photonics News* **2005,** *16*, 30-35.

32. Lindinger, W.; Hansel, A.; Jordan, A., On-line Monitoring of Volatile Organic Compounds at pptv Levels by Means of Proton Transfer Reaction Mass Spectrometry (PTR-MS) Medical Applications, Food Control and Environmental Research. *International Journal of Mass Spectrometry and Ion Processes* **1998,** 191-241.

33. Warneke, C.; Kuczynski, J.; Hansel, A.; Jordan, A.; Vogel, W.; Lindinger, W., Proton transfer reaction mass spectrometry (PTR-MS): Propanol in human breath. *International Journal of Mass Spectrometry* **1996,** *154* (1-2), 61-70.

34. Wang, Z. N.; Wang, C. J., Is breath acetone a biomarker of diabetes? A historical review on breath acetone measurements. *Journal of Breath Research* **2013,** *7* (3), 18.

35. Pleil, J. D.; Lindstrom, A. B., Exhaled human breath measurement method for assessing exposure to halogenated volatile organic compounds. *Clinical Chemistry* **1997,** *43* (5), 723-730.

36. Konvalina, G.; Haick, H., Sensors for Breath Testing: From Nanomaterials to Comprehensive Disease Detection. *Accounts of Chemical Research* **2014,** *47* (1), 66-76.

37. Tricoli, A.; Righettoni, M.; Teleki, A., Semiconductor Gas Sensors: Dry Synthesis and Application. *Angewandte Chemie-International Edition* **2010,** *49* (42), 7632-7659.

38. Korotcenkov, G., Gas response control through structural and chemical modification of metal oxide films: state of the art and approaches. *Sensors and Actuators B-Chemical* **2005,** *107* (1), 209-232.

39. Guan, X. F.; Wang, Y. J.; Luo, P. H.; Yu, Y. L.; Chen, D. G.; Li, X. Y., Incorporating N Atoms into SnO2 Nanostructure as an Approach to Enhance Gas Sensing Property for Acetone. *Nanomaterials* **2019,** *9* (3), 18.

40. Zhang, J.; Qin, Z. Y.; Zeng, D. W.; Xie, C. S., Metal-oxide-semiconductor based gas sensors: screening, preparation, and integration. *Physical Chemistry Chemical Physics* **2017,** *19* (9), 6313-6329.

41. Sakai, G.; Baik, N. S.; Miura, N.; Yamazoe, N., Gas sensing properties of tin oxide thin films fabricated from hydrothermally treated nanoparticles - Dependence of CO and H-2 response on film thickness. *Sensors and Actuators B-Chemical* **2001,** *77* (1-2), 116-121.

42. Wang, D. L.; Zhang, Q.; Hossain, M. R.; Johnson, M., High Sensitive Breath Sensor Based on Nanostructured K2W7O22 for Detection of Type 1 Diabetes. *Ieee Sensors Journal* **2018,** *18* (11), 4399-4404.

43. Hossain, M. R.; Zhang, Q. F.; Johnson, M.; Wang, D. L., Highly Sensitive Room-Temperature Sensor Based on Nanostructured K2W7O22 for Application in the Non-Invasive Diagnosis of Diabetes. *Sensors* **2018,** *18* (11), 9.

44. Hossain, M. R.; Zhang, Q. F.' Johnson, M.; Ama, O.; Wang, D. L., Investigation of Different Materials as Acetone Sensors for Application in Type-1 Diabetes Diagnosis. *Biomedical Journal of Scientific & Technical Research* **2019,** *14* (5), 002619.

45. Ma, L.; Ma, S. Y.; Shen, X. F.; Wang, T. T.; Jiang, X. H.; Chen, Q.; Qiang, Z.; Yang, H. M.; Chen, H., PrFeO3 hollow nanofibers as a highly efficient gas sensor for acetone detection. *Sensors and Actuators B-Chemical* **2018,** *255*, 2546-2554.

46. Wang, X. F.; Ma, W.; Jiang, F.; Cao, E. S.; Sun, K. M.; Cheng, L.; Song, X. Z., Prussian Blue analogue derived porous NiFe2O4 nanocubes for low-concentration acetone sensing at low working temperature. *Chemical Engineering Journal* **2018,** *338*, 504-512.

47. Shin, J.; Choi, S. J.; Lee, I.; Youn, D. Y.; Park, C. O.; Lee, J. H.; Tuller, H. L.; Kim, I. D., Thin-Wall Assembled SnO2 Fibers Functionalized by Catalytic Pt Nanoparticles and their Superior Exhaled-Breath-Sensing Properties for the Diagnosis of Diabetes. *Advanced Functional Materials* **2013,** *23* (19), 2357-2367.

48. Dwivedi, P.; Dhanekar, S.; Das, S., MoO3/nano-Si heterostructure based highly sensitive and acetone selective sensor prototype: a key to non-invasive detection of diabetes. *Nanotechnology* **2018,** *29* (27), 9.

49. Wang, L.; Teleki, A.; Pratsinis, S. E.; Gouma, P. I., Ferroelectric WO3 nanoparticles for acetone selective detection. *Chemistry of Materials* **2008,** *20* (15), 4794-4796.

50. Jia, Q. Q.; Ji, H. M.; Wang, D. H.; Bai, X.; Sun, X. H.; Jin, Z. G., Exposed facets induced enhanced acetone selective sensing property of nanostructured tungsten oxide. *Journal of Materials Chemistry A* **2014,** *2* (33), 13602-13611.

51. Johnson, M.; Zhang, Q.; Wang, D. L., Room-Temperature Ferroelectric K2W7O22 (KWO) Nanorods as a Sensor for Detection of Acetone. *Medical Devices & Sensors* **2019,** *2*, e10044.

52. Righettoni, M.; Tricoli, A.; Pratsinis, S. E., Si:WO3 Sensors for Highly Selective Detection of Acetone for Easy Diagnosis of Diabetes by Breath Analysis. *Analytical Chemistry* **2010,** *82* (9), 3581-3587.

53. Yoshimura, M.; Byrappa, K., Hydrothermal processing of materials: past, present and future. *Journal of Materials Science* **2008,** *43* (7), 2085-2103.

54. Lopes, L. F.; Pontes, F. M.; Garcia, L. O.; Pontes, D. S. L.; Padovani, D.; Chiquito, A. J.; Teixeira, S. R.; Colmenares, Y. N.; Mastelaro, V. R.; Longo, E., Silver-controlled evolution of morphological, structural, and optical properties of three-dimensional hierarchical WO3 structures synthesized from hydrothermal method. *Journal of Alloys and Compounds* **2018,** *736*, 143-151.

55. Tang, B. L.; Jiang, G. H.; Chen, W. X.; Wan, J. M., First-Principles Study on Hexagonal WO3 for HCHO Gas Sensing Application. *Acta Metallurgica Sinica-English Letters* **2015,** *28* (6), 772-780.

56. Supothina, S.; Suwan, M.; Wisitsoraat, A., Hydrothermal synthesis of K2W4O13 nanowire with high H2S gas sensitivity. *Microelectronic Engineering* **2014,** *126*, 88-92.

57. Woodward, P. M.; Sleight, A. W.; Vogt, T., Ferroelectric tungsten trioxide. *Journal of Solid State Chemistry* **1997,** *131* (1), 9-17.

58. Arai, M.; Hayashi, S.; Yamamoto, K.; Kim, S. S., RAMAN STUDIES OF PHASE-TRANSITIONS IN GAS-EVAPORATED WO3 MICROCRYSTALS. *Solid State Communications* **1990,** *75* (7), 613-616.

59. Li, T. T.; Shen, Y. B.; Zhao, S. K.; Chen, X. X.; Li, G. D.; Lu, R.; Zhu, L. J.; Li, H. S.; Wei, D. Z.; Shen, Y. S., Xanthate sensing properties of Pt-functionalized WO3 microspheres synthesized by one-pot hydrothermal method. *Ceramics International* **2018,** *44* (5), 4814-4823.

60. Mu, W. J.; Li, M.; Li, X. L.; Ma, Z. P.; Zhang, R.; Yu, Q. H.; Lv, K.; Xie, X.; He, J. H.; Wei, H. Y.; Jian, Y., Guanidine sulfate-assisted synthesis of hexagonal WO3 nanoparticles with enhanced adsorption properties. *Dalton Transactions* **2015,** *44* (16), 7419-7427.

61. Hossain, M. R.; Zhang, Q. F.; Johnson, M.; Wang, D. L., Investigation of humidity cross-interference effect on acetone breath sensor based on nanostructured $K_2W_7O_{22}$. *EngPress* **2017,** *1* (1), 30-34.

62. Pokhrel, S.; Simion, C. E.; Teodorescu, V. S.; Barsan, N.; Weimar, U., Synthesis, Mechanism, and Gas-Sensing Application of Surfactant Tailored Tungsten Oxide Nanostructures. *Advanced Functional Materials* **2009,** *19* (11), 1767-1774.

63. Hu, L. H.; Peng, Q.; Li, Y. D., Selective Synthesis of Co3O4 Nanocrystal with Different Shape and Crystal Plane Effect on Catalytic Property for Methane Combustion. *Journal of the American Chemical Society* **2008,** *130* (48), 16136

64. Han, X. G.; Li, L.; Wang, C., Synthesis of Tin Dioxide Nanooctahedra with Exposed High-Index {332} Facets and Enhanced Selective Gas Sensing Properties. *Chemistry-an Asian Journal* **2012,** *7* (7), 1572-1575.

65. Boppella, R.; Anjaneyulu, K.; Basak, P.; Manorama, S. V., Facile Synthesis of Face Oriented ZnO Crystals: Tunable Polar Facets and Shape Induced Enhanced Photocatalytic Performance. *Journal of Physical Chemistry C* **2013,** *117* (9), 4597-4605.

66. Zhang, H. B.; Yao, M. S.; Bai, L. Y.; Xiang, W. C.; Jin, H. C.; Li, J. L.; Yuan, F. L., Synthesis of uniform octahedral tungsten trioxide by RF induction thermal plasma and its application in gas sensing. *Crystengcomm* **2013,** *15* (7), 1432-1438.

67. Johnson, M. E.; Zhang, Q. F.; Wang, D. L., KxWO Is a Novel Ferroelectric Nanomaterial for Application as a Room Temperature Acetone Sensor. *Nanomaterials* **2020,** *10* (2), 10.

68. Osiac, M.; Cioatera, N.; Jigau, M., Structural, Morphological, and Optical Properties of Iron Doped WO3 Thin Film Prepared by Pulsed Laser Deposition. *Coatings* **2020,** *10* (4), 13.

69. Maiti, U. N.; Lee, W. J.; Lee, J. M.; Oh, Y.; Kim, J. Y.; Kim, J. E.; Shim, J.; Han, T. H.; Kim, S. O., 25th Anniversary Article: Chemically Modified/Doped Carbon Nanotubes & Graphene for Optimized Nanostructures & Nanodevices. *Advanced Materials* **2014,** *26* (1), 40-67.

70. Kannan, K.; Sadasivuni, K. K.; Abdullah, A. M.; Kumar, B., Current Trends in MXene-Based Nanomaterials for Energy Storage and Conversion System: A Mini Review. *Catalysts* **2020,** *10* (5), 28.

71. Kannan, K.; Sliem, M. H.; Abdullah, A. M.; Sadasivuni, K. K.; Kumar, B., Fabrication of ZnO-Fe-MXene Based Nanocomposites for Efficient CO2 Reduction. *Catalysts* **2020,** *10* (5), 15.

72. Xiong, J.; Di, J.; Li, H. M., Charge steering in ultrathin 2D nanomaterials for photocatalysis. *Journal of Materials Chemistry A* **2020,** *8* (26), 12928-12950.

73. Fang, W. S.; Huang, L.; Zaman, S.; Wang, Z. T.; Han, Y. J.; Xia, B. Y., Recent Progress on Two-dimensional Electrocatalysis. *Chemical Research in Chinese Universities* **2020,** *36* (4), 611-621.

74. Rahimi-Iman, A., Advances in Functional Nanomaterials Science. *Annalen Der Physik* **2020,** *532* (9), 23.

75. Lin, H.; Chen, Y.; Shi, J. L., Insights into 2D MXenes for Versatile Biomedical Applications: Current Advances and Challenges Ahead. *Advanced Science* **2018,** *5* (10), 20.

76. Wang, S. G.; Yang, X. Q.; Zhou, L. L.; Li, J. F.; Chen, H. R., 2D nanostructures beyond graphene: preparation, biocompatibility and biodegradation behaviors. *Journal of Materials Chemistry B* **2020,** *8* (15), 2974-2989.

77. Sundaram, P.; Abrahamse, H., Phototherapy Combined with Carbon Nanomaterials (1D and 2D) and Their Applications in Cancer Therapy. *Materials* **2020,** *13* (21), 20.

78. Bhatia, I. S.; Randhawa, D. K. K., Something more than graphene - futuristic two-dimensional nanomaterials. *Current Science* **2020,** *118* (11), 1656-1671.

79. Huang, X.; Zeng, Z. Y.; Zhang, H., Metal dichalcogenide nanosheets: preparation, properties and applications. *Chemical Society Reviews* **2013,** *42* (5), 1934-1946.

80. Chhowalla, M.; Liu, Z. F.; Zhang, H., Two-dimensional transition metal dichalcogenide (TMD) nanosheets. *Chemical Society Reviews* **2015,** *44* (9), 2584-2586.

81. Chen, Y.; Tan, C. L.; Zhang, H.; Wang, L. Z., Two-dimensional graphene analogues for biomedical applications. *Chemical Society Reviews* **2015,** *44* (9), 2681-2701.

82. Li, D.; Muller, M. B.; Gilje, S.; Kaner, R. B.; Wallace, G. G., Processable aqueous dispersions of graphene nanosheets. *Nature Nanotechnology* **2008,** *3* (2), 101-105.

83. Naguib, M.; Kurtoglu, M.; Presser, V.; Lu, J.; Niu, J. J.; Heon, M.; Hultman, L.; Gogotsi, Y.; Barsoum, M. W., Two-Dimensional Nanocrystals Produced by Exfoliation of Ti3AlC2. *Advanced Materials* **2011,** *23* (37), 4248-4253.

84. Naguib, M.; Mochalin, V. N.; Barsoum, M. W.; Gogotsi, Y., 25th Anniversary Article: MXenes: A New Family of Two-Dimensional Materials. *Advanced Materials* **2014,** *26* (7), 992-1005.

85. Barsoum, M. W.; Radovic, M., Elastic and Mechanical Properties of the MAX Phases. In *Annual Review of Materials Research, Vol 41*, Clarke, D. R.; Fratzl, P., Eds. Annual Reviews: Palo Alto, 2011; Vol. 41, pp 195-227.

86. Sun, Z. M., Progress in research and development on MAX phases: a family of layered ternary compounds. *International Materials Reviews* **2011,** *56* (3), 143-166.

87. Yoshida, M.; Hoshiyama, Y.; Ommyoji, J.; Yamaguchi, A., Reaction mechanism for the synthesis of Ti3AlC2 through an intermediate carbide of Ti3AlC from elemental Ti, Al, and C powder mixture. *Journal of the Ceramic Society of Japan* **2010,** *118* (1373), 37-42.

88. Verger, L.; Natu, V.; Carey, M.; Barsoum, M. W., MXenes: An Introduction of Their Synthesis, Select Properties, and Applications. *Trends in Chemistry* **2019,** *1* (7), 656-669.

89. Anasori, B.; Xie, Y.; Beidaghi, M.; Lu, J.; Hosler, B. C.; Hultman, L.; Kent, P. R. C.; Gogotsi, Y.; Barsoum, M. W., Two-Dimensional, Ordered, Double Transition Metals Carbides (MXenes). *Acs Nano* **2015,** *9* (10), 9507-9516.

90. Tan, T. L.; Jin, H. M.; Sullivan, M. B.; Anasori, B.; Gogotsi, Y., High-Throughput Survey of Ordering Configurations in MXene Alloys Across Compositions and Temperatures. *Acs Nano* **2017,** *11* (5), 4407-4418.

91. Naguib, M.; Gogotsi, Y., Synthesis of Two-Dimensional Materials by Selective Extraction. *Accounts of Chemical Research* **2015,** *48* (1), 128-135.

92. Naguib, M.; Mashtalir, O.; Carle, J.; Presser, V.; Lu, J.; Hultman, L.; Gogotsi, Y.; Barsoum, M. W., Two-Dimensional Transition Metal Carbides. *Acs Nano* **2012,** *6* (2), 1322-1331.

93. Ghidiu, M.; Naguib, M.; Shi, C.; Mashtalir, O.; Pan, L. M.; Zhang, B.; Yang, J.; Gogotsi, Y.; Billinge, S. J. L.; Barsoum, M. W., Synthesis and characterization of two-dimensional Nb4C3 (MXene). *Chemical Communications* **2014,** *50* (67), 9517-9520.

94. Naguib, M.; Halim, J.; Lu, J.; Cook, K. M.; Hultman, L.; Gogotsi, Y.; Barsoum, M. W., New Two-Dimensional Niobium and Vanadium Carbides as Promising Materials for Li-Ion Batteries. *Journal of the American Chemical Society* **2013,** *135* (43), 15966-15969.

95. Kurtoglu, M.; Naguib, M.; Gogotsi, Y.; Barsoum, M. W., First principles study of two-dimensional early transition metal carbides. *Mrs Communications* **2012,** *2* (4), 133-137.

96. Liang, X.; Garsuch, A.; Nazar, L. F., Sulfur Cathodes Based on Conductive MXene Nanosheets for High-Performance Lithium-Sulfur Batteries. *Angewandte Chemie-International Edition* **2015,** *54* (13), 3907-3911.

97. Chen, J.; Chen, K.; Tong, D. Y.; Huang, Y. J.; Zhang, J. W.; Xue, J. M.; Huang, Q.; Chen, T., CO2 and temperature dual responsive "Smart" MXene phases. *Chemical Communications* **2015,** *51* (2), 314-317.

98. Lei, J. C.; Zhang, X.; Zhou, Z., Recent advances in MXene: Preparation, properties, and applications. *Frontiers of Physics* **2015,** *10* (3), 276-286.

99. Rakhi, R. B.; Ahmed, B.; Hedhili, M. N.; Anjum, D. H.; Alshareef, H. N., Effect of Postetch Annealing Gas Composition on the Structural and Electrochemical Properties of Ti2CTx MXene Electrodes for Supercapacitor Applications. *Chemistry of Materials* **2015,** *27* (15), 5314-5323.

100. Pang, J. B.; Mendes, R. G.; Bachmatiuk, A.; Zhao, L.; Ta, H. Q.; Gemming, T.; Liu, H.; Liu, Z. F.; Rummeli, M. H., Applications of 2D MXenes in energy conversion and storage systems. *Chemical Society Reviews* **2019,** *48* (1), 72-133.

101. Hu, Q. K.; Sun, D. D.; Wu, Q. H.; Wang, H. Y.; Wang, L. B.; Liu, B. Z.; Zhou, A. G.; He, J. L., MXene: A New Family of Promising Hydrogen Storage Medium. *Journal of Physical Chemistry A* **2013,** *117* (51), 14253-14260.

102. Khazaei, M.; Arai, M.; Sasaki, T.; Estili, M.; Sakka, Y., Two-dimensional molybdenum carbides: potential thermoelectric materials of the MXene family. *Physical Chemistry Chemical Physics* **2014,** *16* (17), 7841-7849.

103. Wang, X.; Kajiyama, S.; Iinuma, H.; Hosono, E.; Oro, S.; Moriguchi, I.; Okubo, M.; Yamada, A., Pseudocapacitance of MXene nanosheets for high-power sodium-ion hybrid capacitors. *Nature Communications* **2015,** *6*, 6.

104. Li, Z. Y.; Wang, L. B.; Sun, D. D.; Zhang, Y. D.; Liu, B. Z.; Hu, Q. K.; Zhou, A. G., Synthesis and thermal stability of two-dimensional carbide MXene Ti3C2. *Materials Science and Engineering B-Advanced Functional Solid-State Materials* **2015,** *191*, 33-40.

105. Ma, Z. N.; Hu, Z. P.; Zhao, X. D.; Tang, Q.; Wu, D. H.; Zhou, Z.; Zhang, L. X., Tunable Band Structures of Heterostructured Bilayers with Transition-Metal Dichalcogenide and MXene Mono layer. *Journal of Physical Chemistry C* **2014,** *118* (10), 5593-5599.

106. Johnson, M.; Zhang, Q. F.; Wang, D. L., Titanium carbide MXene: Synthesis, electrical and optical properties and their applications in sensors and energy storage devices. *Nanomaterials and Nanotechnology* **2019,** *9*, 9.

107. Zhang, X.; Zhao, X. D.; Wu, D. H.; Jing, Y.; Zhou, Z., High and anisotropic carrier mobility in experimentally possible Ti2CO2 (MXene) monolayers and nanoribbons. *Nanoscale* **2015,** *7* (38), 16020-16025.

108. Berdiyorov, G. R., Effect of surface functionalization on the electronic transport properties of Ti3C2 MXene. *Epl* **2015,** *111* (6), 5.

109. Xie, Y.; Dall'Agnese, Y.; Naguib, M.; Gogotsi, Y.; Barsoum, M. W.; Zhuang, H. L. L.; Kent, P. R. C., Prediction and Characterization of MXene Nanosheet Anodes for Non-Lithium-Ion Batteries. *Acs Nano* **2014,** *8* (9), 9606-9615.

110. Khazaei, M.; Arai, M.; Sasaki, T.; Ranjbar, A.; Liang, Y. Y.; Yunoki, S., OH-terminated two-dimensional transition metal carbides and nitrides as ultralow work function materials. *Physical Review B* **2015,** *92* (7), 10.

111. Ghidiu, M.; Lukatskaya, M. R.; Zhao, M. Q.; Gogotsi, Y.; Barsoum, M. W., Conductive two-dimensional titanium carbide 'clay' with high volumetric capacitance. *Nature* **2014,** *516* (7529), 78-U171.

112. Alhabeb, M.; Maleski, K.; Anasori, B.; Lelyukh, P.; Clark, L.; Sin, S.; Gogotsi, Y., Guidelines for Synthesis and Processing of Two-Dimensional Titanium Carbide (Ti3C2TX MXene). *Chemistry of Materials* **2017,** *29* (18), 7633-7644.

113. Wang, K.; Zhou, Y. F.; Xu, W. T.; Huang, D. C.; Wang, Z. G.; Hong, M. C., Fabrication and thermal stability of two-dimensional carbide Ti3C2 nanosheets. *Ceramics International* **2016,** *42* (7), 8419-8424.

114. Ng, V. M. H.; Huang, H.; Zhou, K.; Lee, P. S.; Que, W. X.; Xu, J. Z.; Kong, L. B., Recent progress in layered transition metal carbides and/or nitrides (MXenes) and their composites: synthesis and applications. *Journal of Materials Chemistry A* **2017,** *5* (7), 3039-3068.

115. Gao, Q.; Come, J.; Naguib, M.; Jesse, S.; Gogotsi, Y.; Balke, N., Synergetic effects of K+ and Mg2+ ion intercalation on the electrochemical and actuation properties of the two-dimensional Ti3C2 MXene. *Faraday Discussions* **2017,** *199*, 393-403.

116. Maleski, K.; Mochalin, V. N.; Gogotsi, Y., Dispersions of Two-Dimensional Titanium Carbide MXene in Organic Solvents. *Chemistry of Materials* **2017,** *29* (4), 1632-1640.

117. Wang, L.; Tao, W. Q.; Yuan, L. Y.; Liu, Z. R.; Huang, Q.; Chai, Z. F.; Gibson, J. K.; Shi, W. Q., Rational control of the interlayer space inside two-dimensional titanium carbides for highly efficient uranium removal and imprisonment. *Chemical Communications* **2017,** *53* (89), 12084-12087.

118. Lipatov, A.; Alhabeb, M.; Lukatskaya, M.R.; Boson, A.; Gogotsi, Y.; Sinitskii, A., Effect of Synthesis on Quality, Electronic Properties and Environmental Stability of Individual Monolayer Ti_3C_2 MXene Flakes. *Advanced Electronic Materials* **2016,** *2* (12), 9.

119. Liu, P.; Yue, M.; Xue, T.; Bi, M. H.; Yao, P., Preparation conditions and electrical properties of Ti3C2Tx nanosheets. *Materials Science in Semiconductor Processing* **2019,** *104*, 6.

120. Sun, N.; Yang, B. Y.; Zheng, J. C.; He, Z. J.; Tong, H.; Tang, L. B.; An, C. S.; Xiao, B., Effect of synthesis temperature on the phase structure, morphology and electrochemical performance of Ti3C2 as an anode material for Li-ion batteries. *Ceramics International* **2018,** *44* (14), 16214-16218.

121. Cancer. Available online: https://www.who.int/news-room/fact-sheets/detail/cancer (accessed on 10 July 2021).

122. Small Cell Lung Cancer—Cancer Therapy Advisor. Available online: https://www.cancertherapyadvisor.com/home/decision-support-in-medicine/imaging/small-cell-lung-cancer/ (accessed on 10 July 2021)

123. Molina, J.R.; Yang, P.; Cassivi, S.D.; Schild, S.E.; Adjei, A.A. Non-Small Cell Lung Cancer: Epidemiology, Risk Factors, Treatment, and Survivorship. In *Mayo Clinic Proceedings*; Elsevier Ltd.: Amsterdam, The Netherlands, 2008; Volume 83, pp. 584–594.

124. Torre, L.A.; Siegel, R.L.; Jemal, A. Lung Cancer Statistics. *Adv. Exp. Med. Biol.* **2016**, *893*, 1–19.

125. Asbestos Lung Cancer: Causes, Diagnosis & Treatment. Available online: https://www.asbestos.com/cancer/lung-cancer/ (accessed on 10 July 2021)

126. Deadliest Cancers Receive the Least Attention. Available online: https://www.asbestos.com/featured-stories/cancers-that-kill-us/ (accessed on 10 July 2021)

127. Dela Cruz, C.S.; Tanoue, L.T.; Matthay, R.A. Lung Cancer: Epidemiology, Etiology, and Prevention. *CME* **2011**, *32*, 605–644.

128. Lee, S.H. Chemotherapy for Lung Cancer in the Era of Personalized Medicine. *Tuberc. Respir. Dis. (Seoul)* **2019**, *82*, 179–189.

129. Cheng, M.; Jolly, S.; Quarshie, W.O.; Kapadia, N.; Vigneau, F.D.; Kong, F.M. Modern Radiation Further Improves Survival in Non-Small Cell Lung Cancer: An Analysis of 288,670 Patients. *J. Cancer* **2019**, *10*, 168–177.

130. Sandler, A.B.; Dubinett, S.M. COX-2 Inhibition and Lung Cancer. *Semin. Oncol.* **2004**, *31* (Suppl. 7), 45–52.

131. Vega, O.M.; Abkenari, S.; Tong, Z.; Tedman, A.; Huerta-Yepez, S. Omega-3 Polyunsaturated Fatty Acids and Lung Cancer: Nutrition or Pharmacology? *Nutr. Cancer* **2020**, 1–21.

132. Yin, Y.; Sui, C.; Meng, F.; Ma, P.; Jiang, Y. The Omega-3 Polyunsaturated Fatty Acid Docosahexaenoic Acid Inhibits Proliferation and Progression of Non-Small Cell Lung Cancer Cells through the Reactive Oxygen Species-Mediated Inactivation of the PI3K /Akt Pathway. In *Lipids in Health and Disease*; BioMed Central Ltd.: London, UK, 2017.

133. Kouremenos, K.A.; Johansson, M.; Marriott, P.J. Advances in Gas Chromatographic Methods for the Identification of Biomarkers in Cancer. *J. Cancer* **2012**, *3*, 404–420.

134. Cancer—Diagnosis and treatment—Mayo Clinic. Available online: https://www.mayoclinic.org/diseases-conditions/cancer/diagnosis-treatment/drc-20370594 (accessed on 10 July 2021).

135. Problems with MRI for Cancer Diagnosis. Available online: https://www.ctoam.com/precision-oncology/why-we-exist/standard-treatment/diagnostics/mri/ (accessed on 10 July 2021).

136. The Pros and Cons of PET/CT Scans|Independent Imaging. Available online: https://www.independentimaging.com/the-pros-and-cons-of-pet-ct-scans/ (accessed on 10 July 2021).

137. Fred, H.L. Drawbacks and Limitations of Computed Tomography: Views from a Medical Educator. *Tex. Heart Inst. J.* **2004**, *31*, 345–348.

138. Bitencourt, A.G.V.; Graziano, L.; Guatelli, C.S.; Albuquerque, M.L.L.; Marques, E.F. Ultrasound-Guided Biopsy of Breast Calcifications Using a New Image Processing Technique: Initial Experience. *Radiol. Bras.* **2018**, *51*, 106–108.

139. Endoscopy: Purpose, Procedure, Risks. Available online: https://www.webmd.com/digestive-disorders/digestive-diseases-endoscopy#1 (accessed on 10 July 2021).

140. Gas Chromatography. Available online: http://www.chemforlife.org/teacher/topics/gas_chromatography.htm (accessed on 10 July 2021).

141. Borer, J.S.; Simon, L.S. Cardiovascular and Gastrointestinal Effects of COX-2 Inhibitors and NSAIDs: Achieving a Balance. *Arthritis Res. Ther*. **2005**, *7* (Suppl. 4), S14–S22.

142. Yang, P.; Chan, D.; Felix, E.; Cartwright, C.; Menter, D.G.; Madden, T.; Klein, R.D.; Fischer, S.M.; Newman, R.A. Formation and Antiproliferative Effect of Prostaglandin E3 from Eicosapentaenoic Acid in Human Lung Cancer Cells. *J. Lipid Res.* **2004**, *45*, 1030–1039.

143. Xu, Y.; Qi, J.; Yang, X.; Wu, E.; Qian, S.Y. Free Radical Derivatives Formed from Cyclooxygenase-Catalyzed Dihomo-γ-Linolenic Acid Peroxidation Can Attenuate Colon Cancer Cell Growth and Enhance 5-Fluorouracil's Cytotoxicity. *Redox Biol.* **2014**, *2*, 610–618.

144. Xu, Y.; Yang, X.; Wang, T.; Yang, L.; He, Y.Y.; Miskimins, K.; Qian, S.Y. Knockdown Delta-5-Desaturase in Breast Cancer Cells That Overexpress COX-2 Results in Inhibition of Growth, Migration and Invasion via a Dihomo-γ-Linolenic Acid Peroxidation Dependent Mechanism. *BMC Cancer* **2018**, *18*, 1–15.

145. Pang, L.; Shah, H.; Wang, H.; Shu, D.; Qian, S.Y.; Sathish, V. EpCAM-Targeted 3WJ RNA Nanoparticle Harboring Delta-5-Desaturase SiRNA Inhibited Lung Tumor Formation via DGLA Peroxidation. *Mol. Ther. Nucleic Acids* **2020**, *22*, 222–235.

146. Yang, X.; Xu, Y.; Wang, T.; Shu, D.; Guo, P.; Miskimins, K.; Qian, S.Y. Inhibition of Cancer Migration and Invasion by Knocking down Delta-5-Desaturase in COX-2 Overexpressed Cancer Cells. *Redox Biol.* **2017**, *11*, 653–662.

147. Sadiq, M.; Pang, L.; Johnson, M.; Sathish, V.; Wang, D. 2D Nanomaterial, Ti_3C_2 MXene-Based Sensor to Guide Lung Cancer Therapy and Management. *Proceedings* **2020**, *60*, 29.

148. Lee, J. E.; Lim, C. K.; Park, H. J.; Song, H.; Choi, S. Y.; Lee, D. S., ZnO-CuO Core-Hollow Cube Nanostructures for Highly Sensitive Acetone Gas Sensors at the ppb Level. *Acs Applied Materials & Interfaces* **2020,** *12* (31), 35688-35697.

149. Lukatskaya, M. R.; Mashtalir, O.; Ren, C. E.; Dall'Agnese, Y.; Rozier, P.; Taberna, P. L.; Naguib, M.; Simon, P.; Barsoum, M. W.; Gogotsi, Y., Cation Intercalation and High

Volumetric Capacitance of Two-Dimensional Titanium Carbide. *Science* **2013,** *341* (6153), 1502-1505.

150. Huang, K.; Li, Z. J.; Lin, J.; Han, G.; Huang, P., Two-dimensional transition metal carbides and nitrides (MXenes) for biomedical applications. *Chemical Society Reviews* **2018,** *47* (14), 5109-5124.

151. Yuan, W. J.; Yang, K.; Peng, H. F.; Li, F.; Yin, F. X., A flexible VOCs sensor based on a 3D Mxene framework with a high sensing performance. *Journal of Materials Chemistry A* **2018,** *6* (37), 18116-18124.

152. Kim, S. J.; Koh, H. J.; Ren, C. E.; Kwon, O.; Maleski, K.; Cho, S. Y.; Anasori, B.; Kim, C. K.; Choi, Y. K.; Kim, J.; Gogotsi, Y.; Jung, H. T., Metallic Ti3C2TX MXene Gas Sensors with Ultrahigh Signal-to-Noise Ratio. *Acs Nano* **2018,** *12* (2), 986-993.

153. Ama, O.; Sadiq, M.; Johnson, M.; Zhang, Q.; Wang, D. Novel 1D/2D KWO/$Ti_3C_2T_x$ Nanocomposite-Based Acetone Sensor for Diabetes Prevention and Monitoring. *Chemosensors* **2020**, *8*, 102.

APPENDIX

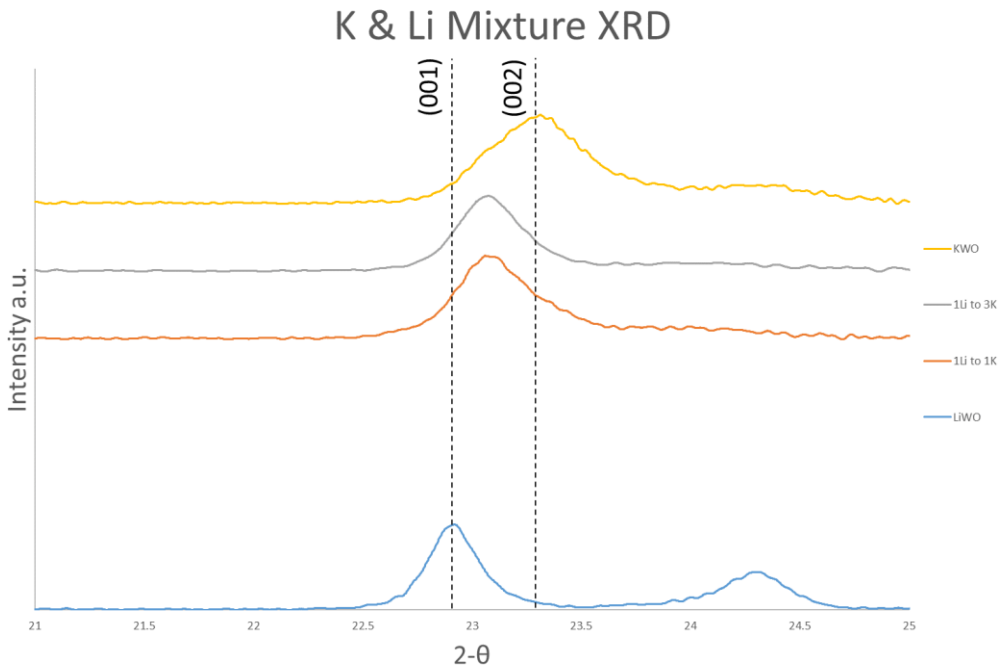

Figure A1. XRD pattern of tungsten oxide samples grown with a Li, K, and mixed sources highlighting the peak shift from the *(001)* to *(002)* facets.

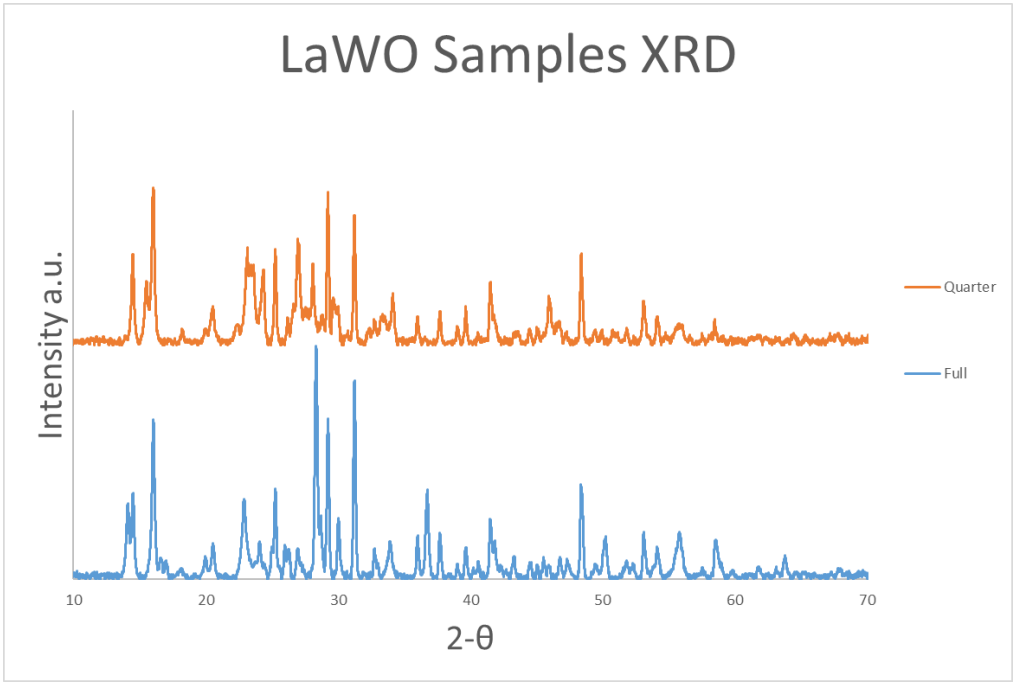

Figure A2. XRD of collected LaWO samples synthesized at full and quarter molar equivalences.

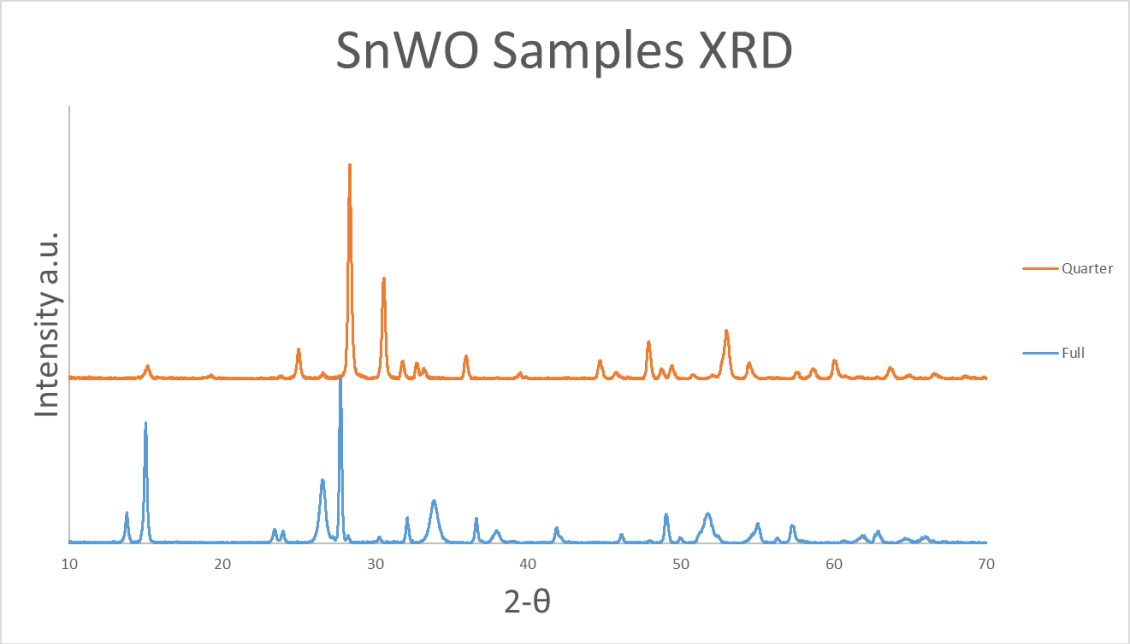

Figure A3. XRD of collected SnWO samples synthesized at full and quarter molar equivalences.

Table A1. Initial sensing data for eighth-molar equivalence CuWO and CrWO done at RH of 30%.

Sample	Test #	Initial Resistance (MΩ)	Dry Air Resistance (MΩ)	Final Resitance (MΩ)	Sensitivity (%)
CuWO	1	1.59	3.5	5.15	103.7
	2	2.17	3.43	4.18	34.5
	3	2.24	3.42	3.92	22.3
CrWO	1	0.229	0.8	7.45	2903.9
	2	0.56	1.48	11.32	1757.1
	3	1.0	2.13	14.89	1276.0

Table A2. Table showing the composition of each sample for BEAS2B used in Ti_3C_2 based cancer sensing.

Sample	Cell	8-HOA	PGE2	BSA
1	$\mathbf{10^6}$BEAS2B	none	none	None
2	$\mathbf{10^6}$BEAS2B	0.6 ug/mL	none	None
3	$\mathbf{10^6}$BEAS2B	none	6 ug/mL	None
4	None	none	none	1 mg/mL

Table A3. The composition of each sample for A549 cells treated by 8-hydroxyoctanoic acid (8-HOA), Prostaglandin E2 (PGE2), dihomo-γ-linolenic acid (DGLA), delta-5-desaturase inhibitor (D5Di), and DGLA + D5Di.

Sample	Cell	DGLA	D5Di	8-HOA	PGE2	Estimated 8-HOA/PGE2 level
1	10^6 A549	none	none	none	none	Low 8-HOA; low PGE2
2	10^6 A549	none	none	0.6 ug/mL	none	High 8-HOA; low PGE2
3	10^6 A549	none	none	none	6 ug/mL	Low 8-HOA; high PGE2
4	10^6 A549	100 uM	none	none	none	Low 8-HOA; high PGE2
5	10^6 A549	none	10 uM	none	none	Low 8-HOA; low PGE2
6	10^6 A549	100 uM	10 uM	none	none	High 8-HOA; low PGE2